

Democratic Republic of Algeria

Ministry of Higher Education and Scientific Research



University of Blida 01

Institute of Aeronautics and Space Studies



End of Studies Thesis Master's in Aeronautics

Option: **Propulsion**

THEME :

The effect of turbulence models on the performance prediction of a centrifugal compressor

Made by :

RAHMANI Abderrahmane

BENKOURGLOU Ilies Abdenour

Supervised by :

Mr. LAAZAB Sebaa

Mr. BEKHTI Ahmed

2023/2024

ABSTRACT

Computational fluid dynamics (CFD) simulations have become an indispensable tool in the design process of centrifugal compressors, enabling the prediction of global performance parameters such as pressure ratio and efficiency with reasonable accuracy.

However, the accurate prediction of detailed compressor flow fields remains a significant challenge, often associated with the selection of an appropriate turbulence model. In the iterative design optimization process, there is a pressing need for robust, numerically stable turbulence models that can provide accurate results within a short time.

This study aims to assess the accuracy of various turbulence simulation models in predicting the flow fields of a centrifugal compressor. An exemplar open test case, the "Radiver" centrifugal compressor, was used to compare the performance of three eddy-viscosity models (Spalart-Allmaras (S-A), $k-\epsilon$, and $k-\omega$) and two Reynolds stress models (Shear Stress Transport (SST) and a modified SST with curvature correction (SST-CC)) of a steady state of a compressible ideal gas (Air) using the CFD code ANSYS CFX.

Key words : centrifugal compressor ; prediction ; turbulence ; simulation ; steady state ; compressible .

RESUME

Les simulations numériques de la dynamique des fluides (CFD) sont devenues un outil indispensable dans le processus de conception des compresseurs centrifuges, permettant de prédire avec une précision raisonnable les paramètres de performance globaux tels que le rapport de pression et l'efficacité.

Cependant, la prédiction précise des champs d'écoulement détaillés des compresseurs reste un défi important, souvent associé à la sélection d'un modèle de turbulence approprié. Dans le processus itératif d'optimisation de la conception, il existe un besoin pressant de modèles de turbulence robustes et numériquement stables, capables de fournir des résultats précis en peu de temps.

Cette étude vise à évaluer la précision de divers modèles de simulation de turbulence pour prédire les champs d'écoulement d'un compresseur centrifuge. Un cas d'essai ouvert exemplaire, le compresseur centrifuge "*Radiver*", a été utilisé pour comparer les performances de trois modèles de turbulence-viscosité (Spalart-Allmaras (**S-A**), **k- ϵ** et **k- ω**) et de deux modèles de contrainte de Reynolds (Shear Stress Transport (**SST**) et un SST modifié avec correction de courbure (**SST-CC**)) d'un état stable d'un gaz idéal compressible (Air) à l'aide du code de CFD ANSYS CFX.

Mots clés : compresseur centrifuge ; prédiction ; turbulence ; simulation ; régime stationnaire ; compressible.

المخلص

أصبحت عمليات محاكاة ديناميكيات الموائع الحسابية (CFD) أداة لا غنى عنها في عملية تصميم ضواغط الطرد المركزي، مما يتيح التنبؤ بمعلمات الأداء العالمي مثل نسبة الضغط والكفاءة بدقة معقولة.

ومع ذلك، لا يزال التنبؤ الدقيق لحقول التدفق التفصيلية للضاغط يمثل تحديًا كبيرًا، وغالبًا ما يرتبط باختيار نموذج الاضطراب المناسب. في عملية تحسين التصميم التكراري، هناك حاجة ملحة لنماذج اضطراب قوية ومستقرة عدديًا يمكنها تقديم نتائج دقيقة في غضون وقت قصير.

تهدف هذه الدراسة إلى تقييم دقة العديد من نماذج الاضطراب في التنبؤ بحقول التدفق لضاغط طارد مركزي. تم استخدام حالة اختبار نموذجية مفتوحة، وهي الضاغط الطارد المركزي "Radiver"، لمقارنة أداء ثلاثة نماذج للزوجية الدوامية (S-A) Spalart-Allmaras ، $k-\epsilon$ ، $k-\omega$ ونموذجين لإجهاد رينولدز (نقل الإجهاد القصي (SST) ونموذج معدل SST مع تصحيح الانحناء (SST-CC)) لحالة مستقرة لغاز مثالي قابل للانضغاط (الهواء) باستخدام كود

.ANSYS CFX : CFD

الكلمات المفتاحية : ضاغط مركزي ; تنبؤ ; الاضطراب ; محاكاة ; حالة ثابتة ; قابل للضغط.

ACKNOWLEDGEMENTS

In the name of Allah, the Most Beneficent and Most Merciful. We thank Allah for all His blessing and strength that He gives us in completing this humble work.

We would like to extend my heartfelt gratitude to the following individuals and organizations for their invaluable support and contributions to this:

- **Mr. LAAZAB Sebaa** and **Mr. BEKHTI Ahmed**, for their guidance and expertise, their insights and suggestions have been invaluable in helping us to refine our research.
- We would also like to thank the contributions of **Mr. REZZOUG T.** for facilitating the work in the computing center.

Finally, we would like to thank all those who have contributed in any way to the feasibility of this work.

DEDICATION

I would like to dedicate this thesis to:

All my family BENKOURGLOU ,My dad , My mum , my brother , my uncles.

,to my cousins.

My friends in Mostaganem (team nice).

All my friends in the graduating propulsion class.

My Friends of university city.

All professors who taught me .

BENKOURGLOU ILIES ABDENOUR

•

I dedicate this modest work and all my efforts over the past five years:

To my very dear parents, my reason for living, symbol of courage and sacrifice, may

God keep them.

To my very dear sisters.

To my uncles, aunts and cousins.

To all my family.

To all the friends that I shared this journey with.

RAHMANI ABDERRAHMANE

TABLE OF CONTENTS

ABSTRACT	1
RESUME	2
المخلص	3
ACKNOWLEDGEMENTS	4
DEDICATION	5
TABLE OF CONTENTS	6
LIST OF FIGURES	9
LIST OF TABLES	12
LIST OF SYMBOLS	13
INTRODUCTION	14
LITERATURE REVIEW	16
CHAPTER I : THEORY	19
I.1. INTRODUCTION	20
I.2. CENTRIFUGAL COMPRESSOR COMPONENTS	22
I.2.1. The impeller.....	22
I.2.2. The diffuser.....	23
I.2.3. Scroll or Manifold	24
I.3. VELOCITY TRIANGLES OF CENTRIFUGAL COMPRESSORS.....	25
I.3.1. Inlet Velocity Triangle.....	25
I.3.2. Impeller Velocity Triangles.....	25
I.3.3. Outlet Velocity Triangle.....	26
I.4. AERODYNAMICS OF CENTRIFUGAL COMPRESSORS.....	26
I.4.1. Main flow (Analysis of the forces).....	26
I.4.2. Secondary flow	28
I.5. THE REFERENCE PLANES IN A CENTRIFUGAL COMPRESSOR	29
I.6. CENTRIFUGAL COMPRESSOR CHARACTERISTICS.....	29
I.6.1. STALL.....	30
I.6.2. SURGING	31
I.6.3. CHOKING.....	32
I.6.4. THE OPERATING RANGE.....	33
I.7. LOSSES	33
I.7.1. Rotor Losses	33

I.7.2. Stator Losses.....	33
I.8. PERFORMANCE PREDICTION	34
CHAPTER II : MATHEMATICAL MODEL	35
II.1. INTRODUCTION.....	36
II.2. COMPRESSOR THERMODYNAMICS	36
II.2.1. Stage Total-to-Total Efficiency	36
II.2.2. Total-to-Static Efficiency	37
II.2.3. Corrected Compressor Mass Flow	38
II.2.4. Corrected Pressure.....	38
II.2.5. Corrected Temperature	39
II.3. GOVERNING EQUATIONS	39
II.4. ROTATIONAL MODEL.....	40
II.5. TURBULENCE MODELING	41
II.5.1. Direct Numerical Simulation (DNS).....	43
II.5.2. Large Eddy Simulation (LES).....	43
II.5.3. RANS.....	44
II.6. ALGEBRAIC (OR ZERO-EQUATION) MODELS	45
II.7. ONE-EQUATION MODELS	46
II.7.1. Spalart-Allmaras	46
II.8. TWO-EQUATION MODELS	46
II.8.1. Standard Model k- ϵ	47
II.8.2. K- ω standard model.....	49
II.8.3. Model k - ω SST (Shear Stress Transport)	50
II.8.4. Rotation and Curvature Correction.....	51
II.9. FLOW MODELLING AT THE WALL	52
II.9.1. Wall treatment.....	53
II.9.2. Automatic wall treatment.....	54
II.10. BOUNDARY CONDITION	56
II.10.1. Wall condition.....	56
II.10.2.Periodicity condition.....	56
CHAPTER III : SIMULATION.....	58
III.1. INTRODUCTION.....	59
III.2. INITIAL DATA	62

III.3. CONSTRUCTION OF A COMPUTATIONAL MODEL (Impeller)	62
III.4. CONSTRUCTION OF A COMPUTATIONAL MODEL (Diffuser)	77
III.5. TECHNOLOGY OF COMPUTATIONAL STUDY.....	85
CHAPTER IV : RESULTS	98
IV.1. INTRODUCTION	99
IV.2. GRID CONVERGENCE STUDY.....	100
IV.3. PROCESSING OF CALCULATION RESULTS AND COMPARISON	102
IV.3.1. The influence of the turbulence model.....	102
IV.3.2. Simulation analysis in the centrifugal compressor.....	105
VI.3.2.a. The impeller.....	105
VI.3.2.b. The diffuser	115
VI.3.2.c. The compressor stage	121
CONCLUSION	131
REFERENCES	132

LIST OF FIGURES

FIGURE I.1.1.	A VERSION OF THE CENTRIFUGAL COMPRESSOR USED BY SIR FRANK WHITTLE.	20
FIGURE I.1.2.	PRESSURE AND VELOCITY THROUGH A CENTRIFUGAL COMPRESSOR.	21
FIGURE I.1.3.	FLOW ENTERING A VANED DIFFUSER.	21
FIGURE I.2.1.	MAIN COMPONENTS OF A CENTRIFUGAL COMPRESSOR IN ISOMETRIC VIEW.	22
FIGURE I.2.2.	IMPELLER SHAPE.	23
FIGURE I.2.3.	DIFFERENT TYPES OF DIFFUSER.	23
FIGURE I.2.4.	DIFFERENT SHAPES OF VOLUTE.	24
FIGURE I.3.1.	VELOCITY TRIANGLES OF CENTRIFUGAL COMPRESSORS	25
FIGURE I.4.1.	FORCES AND FLOW CHARACTERISTICS IN A CENTRIFUGAL COMPRESSOR.	28
FIGURE I.5.1.	REFERENCE SURFACES IN THE CENTRIFUGAL COMPRESSOR IMPELLER.	29
FIGURE I.6.1.	THE THEORETICAL CENTRIFUGAL COMPRESSOR CHARACTERISTIC.	30
FIGURE I.6.2.	MECHANISM OF STALL PROPAGATION.	31
FIGURE I.6.3.	CENTRIFUGAL COMPRESSOR CHARACTERISTICS.	32
FIGURE II.2.1.	THE IMPELLER FLOW PROCESS ON A TOTAL-TO-TOTAL AND TOTAL-RELATIVE-TO-TOTAL-RELATIVE.	36
FIGURE II.2.2.	PRESWIRL GUIDE VANES ELIMINATE THE NEED TO TWIST THE IMPELLER INLET SEGMENT.	38
FIGURE II.5.1.	HIERARCHY OF TURBULENCE MODELS.	42
FIGURE II.5.2.	REYNOLDS AVERAGING—ILLUSTRATION OF TURBULENT VELOCITY FLUCTUATIONS v' AND STATISTICAL MEAN.	43
FIGURE II.10.1.	COMPUTATIONAL DOMAIN OF THE RADIVER CENTRIFUGAL COMPRESSOR.	57
FIGURE III.1.1.	ACCURATE NUMERICAL DISCRETIZATION HELPS LINEARIZE THE PARTIAL DIFFERENTIAL EQUATIONS AND CAPTURE THE SENSITIVE VARIABLE GRADIENTS.	61
FIGURE III.3.1.	ANSYS WORKBENCH PROGRAM WINDOW.	63
FIGURE III.3.2.	MNEMONIC DIAGRAM IN ANSYS WORKBENCH.	64
FIGURE III.3.3.	BLADEGEN PROGRAM WINDOW.	65
FIGURE III.3.4.	GEOMETRY OF THE IMPELLER OBTAINED IN THE FIRST APPROXIMATION.	66
FIGURE III.3.5.	ANGLES OF INCLINATION OF THE WALLS OF THE MERIDIONAL BYPASS.	68
FIGURE III.3.6.	CONNECTED BLOCKS OF BLADEGEN AND GEOMETRY PROGRAMS.	68
FIGURE III.3.7.	GEOMETRY OF THE IMPELLER IN DESIGNMODELER.	69
FIGURE III.3.8.	3D MODEL OF THE IMPELLER BLADES OBTAINED IN DESIGNMODELER.	69
FIGURE III.3.9.	TURBOGRID PROGRAM WINDOW WITH THE LOADED GEOMETRY OF THE IMPELLER.	70
FIGURE III.3.10.	SPECIFYING THE RADIAL GAP.	71
FIGURE III.3.11.	ENABLE AUTOMATIC GRID UPDATES.	72
FIGURE III.3.12.	SETTING THE DENSITY OF THE FINITE ELEMENT MESH.	73
FIGURE III.3.13.	3D MODEL OF THE IMPELLER MESH.	74
FIGURE III.3.14.	VIEWING INFORMATION ABOUT THE SECT OF FINITE ELEMENTS.	75
FIGURE III.3.15.	THE VALUE OF THE SELECTED QUALITY PARAMETER.	76

FIGURE III.4.1. BLADE DIFFUSER GEOMETRY OBTAINED AUTOMATICALLY IN THE FIRST APPROXIMATION.....	78
FIGURE III.4.2. CHANGING THE TYPE OF THE BLADE'S TRAILING EDGE	79
FIGURE III.4.3. 3D MODEL OF THE BLADE DIFFUSER OBTAINED IN TURBOGRID..	80
FIGURE III.4.4. TURBOGRID PROGRAM WINDOW WITH THE LOADED GEOMETRY OF THE DIFFUSER.	80
FIGURE III.4.5. DESCRIPTION OF THE MESH TOPOLOGY IN AUTOMATIC MODE.	82
FIGURE III.4.6. SETTING THE DENSITY OF THE FINITE ELEMENT MESH OF THE DIFFUSER.	83
FIGURE III.4.7. A PREVIEW OF THE OBTAINED MESH.	84
FIGURE III.4.8. VIEWING INFORMATION ABOUT THE FINITE ELEMENT MESH.	85
FIGURE III.5.1. VIEW OF THE AREA FOR BUILDING STRUCTURAL DIAGRAMS AFTER ADDING THE ANSYS CFX MODULE.	86
FIGURE III.5.2. ANSYS CFX PRE PROGRAM WINDOW WITH THE LOADED IMPELLER AND DIFFUSER MODEL.	87
FIGURE III.5.3. ROTATING THE OUTLET SYSTEM MODEL AROUND THE OZ AXIS.....	88
FIGURE III.5.4. RESULT OF MATCHING THE COMPRESSOR ELEMENTS.	88
FIGURE III.5.5. FILLING IN THE FIRST DIALOG BOX OF THE TURBO TEMPLATE.	89
FIGURE III.5.6. SETTING THE PARAMETERS OF THE IMPELLER DOMAIN.	90
FIGURE III.5.7. SETTING THE PROPERTIES OF THE OUTLET SYSTEM.	91
FIGURE III.5.8. SETTING THE VALUES OF FLOW PARAMETERS AT THE BOUNDARIES.	92
FIGURE III.5.9. INTERFACE CONTROL PAGE.....	93
FIGURE III.5.10. BOUNDARY CONDITION CONTROL PAGE.....	93
FIGURE III.5.11. VIEW OF THE MODEL IN ANSYS CFX – PRE PROGRAM AFTER COMPLETING THE WORK OF THE TURBO TEMPLATE.....	94
FIGURE III.5.12. SETTING THE SOLVER PARAMETERS.	95
FIGURE III.5.13. STARTING THE TASK-SOLVING PROCESS.....	96
FIGURE III.5.14. VIEW OF THE ANSYS CFX SOLVER PROGRAM WINDOW DURING THE SOLUTION PROCESS.	96
FIGURE IV.1. COMPUTATIONAL DOMAIN AND BOUNDARY CONDITIONS.	99
FIGURE IV.2.1 TOTAL TO-TOTAL PRESSURE RATIO OF DIFFERENT GRIDS AT VARIOUS OPERATING POINTS.	100
FIGURE IV.2.2 VELOCITY PROFILES OF DIFFERENT GRIDS AT VARIOUS STREAMWISE LOCATIONS AT THE OPERATING POINT P.	101
FIGURE IV.3.A.1. TOTAL TO-TOTAL PRESSURE RATIO OF DIFFERENT MODELS AT VARIOUS OPERATING POINTS.	102
FIGURE IV.3.A.2. CIRCUMFERENTIAL VELOCITY CONTOURS FOR DIFFERENT TURBULENCE MODELS AT THE IMPELLER EXIT (PLANE 2M') AND THE OPERATING POINT P.	104
FIGURE IV.3.A.3. ENTROPY FIELD IN THE DIFFUSER OF DIFFERENT MODELS AT THE OPERATING POINT P.....	104
FIGURE IV.3.B.1. THE CONTOURS OF STATIC PRESSURE ON A MERIDIAN PLANE OF THE WHEEL.	105
FIGURE IV.3.B.2. THE STATIC PRESSURE FIELD ON A BLADE-TO-BLADE PLANE.	106
FIGURE IV.3.B.3. THE STATIC PRESSURE FIELD ON ORTHOGONAL PLANES.	107

FIGURE IV.3.B.4. THE EFFECT OF THE VARIATION OF AIR FLOW ON THE DISTRIBUTION OF STATIC PRESSURE FOR THE BLADES.....	108
FIGURE IV.3.B.5. THE VARIATION OF STATIC AND TOTAL PRESSURE IN THE WHEEL.	109
FIGURE IV.3.B.6. VARIATION OF STATIC AND TOTAL TEMPERATURE IN THE WHEEL.	110
FIGURE IV.3.B.7. VARIATION OF THE RELATIVE MACH NUMBER IN THE MERIDIAN PLANE....	111
FIGURE IV.3.B.8. VARIATION OF THE RELATIVE MACH NUMBER IN THE BLADE-TO-BLADE PLANE.	112
FIGURE IV.3.B.9. VARIATION OF TURBULENCE ENERGY.....	112
FIGURE IV.3.B.10. THE VARIATION OF ENTROPY IN THE BLADE-TO-BLADE PLANE RELATIVE TO THE 20% SPAN PLANE.	113
FIGURE IV.3.B.11. THE VARIATION OF ENTROPY IN THE BLADE-TO-BLADE PLANE RELATIVE TO THE 50% SPAN PLANE.	114
FIGURE IV.3.B.12. THE VARIATION OF ENTROPY IN THE BLADE-TO-BLADE PLANE RELATIVE TO THE 80% SPAN PLANE.	114
FIGURE IV.3.B.13. THE VARIATION OF ENTROPY IN THE ORTHOGONAL PLANE AT THE WHEEL OUTLET.....	115
FIGURE IV.3.B.14. STATIC (SP) AND TOTAL (TP) PRESSURE FIELDS.....	116
FIGURE IV.3.B.15. TOTAL PRESSURE FIELD IN THE BLADE-TO-BLADE PLANE RELATIVE TO THE SPAN HEIGHT AT 50%.	117
FIGURE IV.3.B.16. STATIC PRESSURE FIELD RELATIVE TO THE SPAN HEIGHT AT 50%.	117
FIGURE IV.3.B.17. TOTAL PRESSURE FIELDS AT THE DIFFUSER.	118
FIGURE IV.3.B.18. DISTRIBUTION OF STATIC PRESSURE.	119
FIGURE IV.3.B.19. VARIATION OF TOTAL AND STATIC PRESSURE IN THE DIFFUSER.	120
FIGURE IV.3.B.20. ENTROPY FIELD IN THE BLADE-TO-BLADE PLANE AT 50% RELATIVE TO THE SPAN HEIGHT.	121
FIGURE IV.3.B.21. VARIATION OF THE TOTAL PRESSURE FIELD P_t IN THE COMPRESSOR STAGE.	121
FIGURE IV.3.B.22. VARIATION OF THE TOTAL PRESSURE P_t IN THE COMPRESSOR STAGE.....	122
FIGURE IV.3.B.23. VARIATION OF THE STATIC PRESSURE FIELD P_s IN THE COMPRESSOR STAGE.	123
FIGURE IV.3.B.24. VARIATION OF THE STATIC PRESSURE P_s IN THE COMPRESSOR STAGE.....	124
FIGURE IV.3.B.25. VARIATION OF THE RELATIVE MACH NUMBER FIELD IN THE COMPRESSOR STAGE.....	125
FIGURE IV.3.B.26. VARIATION OF THE RELATIVE MACH NUMBER IN THE COMPRESSOR STAGE.	126
FIGURE IV.3.B.27. RELATIVE MACH NUMBER FIELD IN THE CENTRIFUGAL COMPRESSOR STAGE AT THE INTERFACE AND RELATIVE TO THE SPAN HEIGHT AT 50%.	127
FIGURE IV.3.B.28. TURBULENCE ENERGY FIELD IN THE COMPRESSOR STAGE.	128
FIGURE IV.3.B.29. THE VARIATION OF TURBULENCE ENERGY IN THE COMPRESSOR STAGE. ..	129
FIGURE IV.3.B.30. DIAGRAM OF TEMPERATURE AS A FUNCTION OF ENTROPY (T.S) OF THE CENTRIFUGAL COMPRESSOR STAGE.	130

LIST OF TABLES

TABLE II.1. CONSTANTS OF THE STANDARD K- ϵ MODEL.	48
TABLE II.2. CONSTANTS OF THE K- Ω STANDARD MODEL.	50
TABLE II.3. TABLEAU THE CONSTANTS FOR THE SST RC TURBULENCE MODEL	52
TABLE III.5. COMPRESSOR DETAILS FOR $R4/R2 = 1.14$ AT 80% SPEED.	97
TABLE IV.1. GRID REFINEMENTS AT THE OPERATING POINT P.	101

LIST OF SYMBOLS

- y^+ : A dimensionless parameter used in computational fluid dynamics
- γ : Ratio of specific heats
- μ : Dynamic viscosity
- k : Turbulent kinetic energy
- ε : Turbulent dissipation rate
- Δ : Delta
- N : Rotational speed
- M : Mach number
- ρ : Density
- τ : Wall shear stress
- y : Distance from the wall
- Δy : Distance between the first and second mesh
- C : Constant
- u : Velocity
- ω : Angular velocity
- V : velocity scale
- L : length scale
- K : kinetic energy per unit mass
- μ_t : turbulent viscosity
- μ : molecular kinematic viscosity
- G : production of the turbulent viscosity
- ε : rate of turbulent energy dissipation
- α : inverse of the Prandtl number for turbulent flow
- r_2 : Impeller tip radius
- r_4/r_2 : Ratio of impeller outlet radius to impeller tip radius
- α_{4SS} : Diffuser vane setting angle
- C_p : Specific heat capacity at constant pressure
- Γ : Ratio of specific heats
- P : Operating point near surge
- M : Operating point at mid Speedline
- S : Operating point near choke
- $\dot{m}_{exit\ Corr}$: Exit corrected mass flow rate
- $8M$: Outlet plane
- $\Pi_{1,8M}$: Total to-total pressure ratio
- $\tau_{1,8M}$: Total to-total temperature ratio
- $\eta_{1,8M}$: Total to-total efficiency
- PS : Pressure side
- SS : Suction side

INTRODUCTION

Centrifugal compressors are vital components in a wide array of industrial applications, ranging from aerospace propulsion systems to oil and gas processing facilities. Understanding the complex flow dynamics within these compressors is crucial for optimizing their performance and efficiency. Computational Fluid Dynamics (CFD) has become an indispensable tool for simulating and analyzing the flow behavior within centrifugal compressors. However, accurate prediction of turbulent flow phenomena poses a significant challenge, necessitating a thorough assessment of turbulence models.

Turbulence models play a pivotal role in CFD simulations by approximating the effects of turbulent fluctuations on fluid flow. These models are based on various assumptions and equations, each tailored to capture specific aspects of turbulence. However, selecting the most appropriate turbulence model for centrifugal compressor simulations remains a critical task, as the flow within these machines is inherently three-dimensional, unsteady, and highly turbulent.

In this context, this study focuses on evaluating the performance of turbulence models in predicting the flow characteristics within a centrifugal compressor. The assessment encompasses a comprehensive analysis of turbulence model accuracy, encompassing comparisons with experimental data, examination of flow field features, and exploration of model sensitivity to operating conditions and geometric configurations.

By systematically assessing turbulence model predictions, this study aims to enhance the understanding of centrifugal compressor aerodynamics and provide valuable insights into model selection and calibration. Ultimately, improving the accuracy of turbulence modeling in centrifugal compressor simulations will facilitate the design of more efficient and reliable compression systems, with implications for a diverse range of industrial sectors.

The analysis of the flow in this stage of the compressor is generally three-dimensional, compressible, viscous, and turbulent. Therefore, to deal with this problem, which is analytically difficult to solve but numerically possible, we use the *ANSYS CFX 23R2* software.

This work is divided into four chapters:

This bibliographic analysis allows an understanding of the studied phenomenon by citing some study results.

The first chapter: presents generalities on turbomachines and general definitions concerning centrifugal compressors, their classification followed by a description of the different characteristics and internal flows. After having exposed the aerodynamic forces and the general equations governing these flows, and also having exposed the interactions of the flow between rotor-stator.

The second chapter: presents the so-called method of calculating aerothermodynamic parameters in a stage of a centrifugal compressor following the method of one-dimensional analysis with the assumptions of the calculations, it also calculates the different aerodynamic coefficients and losses in this compressor.

The third chapter: in this chapter deals with numerical modeling and the presentation of the software using ANSYS CFX 23R2. We have described in detail the modeling of the geometries of the stage of the centrifugal compressor and we have created the mesh according to conditions. In presenting the turbulence models plus, we use in this study (**k- ϵ** ; **k- ω** ; **SST** ; **SST-CC** and **S-A**). And the finite volume method with numerical discretization, the equations of this problem following a scheme in CFD and the schemes available in this software.

The fourth chapter: the results are present for the wheel of the centrifugal compressor at nominal point; and the validation of the results with the comparison of the experimental results. And also, validation by qualitative comparison with other sources.

Finally, a conclusion with perspectives proposed for future research.

LITERATURE REVIEW

Many researchers have already studied and analyzed the flow in a centrifugal compressor:

LEE GIBSON, LEE GALLOWAY, SUNG IN KIM, STEPHEN SPENCE [1]

Steady-state computational fluid dynamics (CFD) simulations are crucial for designing centrifugal compressors, but predicting detailed compressor flow fields is a challenge due to incorrect turbulence model selection. This study compared three eddy-viscosity and two Reynolds stress models on the centrifugal compressor "Radiver" and found good agreement with experiments. However, local flow field differences were observed, with the SA model showing poor prediction of local flow structures. The SST model showed stable, robust, and time-efficient capability to predict global performance and local flow features.

SHADY ALI, KEVIN J. ELLIOTT, ERIC SAVORY, CHAO ZHANG, ROBERT J. MARTINUZZI, WILLIAM E. LIN [2]

This study evaluates the performance of three turbulence models in a centrifugal compressor stage for an aero-engine. The main focus is the effectiveness of curvature correction terms in two-equation turbulence models, such as the curvature-corrected shear stress transport (SST-CC) model. The results show that the SST-CC model better predicts the choke region and stall region, while the SST model better predicts the choke region. The production multiplier's effects are weaker than the curvature effects near the impeller trailing edge.

SABRI DENIZ, ARMANDO DEL RIO AND ERNESTO CASARTELLI [3]

This paper investigates a low specific speed pump-turbine model, focusing on flow instabilities. The model is experimentally determined and numerically simulated using CFD codes ANSYS-CFX and an inhouse code. The study compares numerical results with experimental data at two guide vane openings (20° and 6°) and different operating points. The results show good agreement between the CFD predictions and experimental data for the 20° guide vane opening, but only the k- ϵ and BSL EARSM models show reasonable agreement for the 6° guide vane opening.

G. DUFOURI, J.-B. CAZALBOU, X. CARBONNEAU, P. CHASSAING [4]

This paper examines two corrections to eddy-viscosity models that account for rotation and curvature effects on turbulence in turbomachines. The first correction is called the Spalart and Shur correction and it is applied to the Spalart and Allmaras model. The second correction is made to the k- model and is developed by Cazalbou et al. The impact of these corrections is assessed using a centrifugal-compressor test case and the Radiver open test case. The results show that both corrections significantly affect the turbulent field and improve the prediction of local flow properties. The predictions of global performances are more sensitive to grid refinement than to the RC turbulence modeling.

WILLIAM J. GOODING, MATTHEW A. MEIER, AND NICOLE L. KEY [5]

Computational tools have become important in design and research recently due to improved computational resources. While historically simplifying model geometry and flow-physics was necessary, modern tools can include realistic features like fillets, surface roughness, and heat transfer. This study simulates a centrifugal compressor stage for an aero-engine application, comparing numerical results to experimental data. The inclusion of fillets and roughness significantly affects flow development, particularly with the SST turbulence model. The study concludes that the BSLEARS model is best for predicting diffuser flow profiles and overall performance, and unsteady effects improve predictive capability.

O DUMITRESCU, V DRĂGAN, I PORUMBEL AND B GHERMAN [6]

The influence of mesh size, discretization schemes, and turbulence models on radial impeller performance in a 14:1 pressure ratio design for the TIDE pulse detonation engine was studied. Numerical studies were conducted using multiple steady-state analyses and one unsteady, single passage analysis. A grid sensitivity study was performed on four grid resolutions, while investigating six different turbulence models. Results revealed that global parameters remained consistent with 1.5 mil cells/passage, but became unstable and resulted in poor convergence above 5 mil cells/passage. The most conservative model was found to be the SST model.

ZI-LIANG LI, XIN-GEN LU, YUN-FENG WU ,GE HAN [7]

The accuracy of predicting performance and flow field in centrifugal compressors through Computational Fluid Dynamics (CFD) is hindered by the complex flow characteristics. Different turbulence models in the Reynolds-Averaged Navier-Stokes Equations (RANS) produce varying simulation results. This study examines the impact of common turbulence models on performance prediction in a high-pressure-ratio centrifugal compressor. By introducing a method to calculate local entropy generation rate, the study proposes an improved method of identifying different types of loss in the compressor. The results highlight the significant influence of secondary flow loss on prediction performance. These findings can assist designers in selecting an appropriate turbulence model for future compressor design.

REINHARD NIEHUIS, HEINZ E. GALLUS, KAI U. ZIEGLER [8]

This two-part paper investigates the impact of impeller-diffuser interaction on flow field configuration in centrifugal compressors. The study uses a flat wedge vaned diffuser, adjusting the diffuser vane angle and radial gap. Results show that smaller radial gaps lead to a more homogeneous flow field and higher diffuser pressure recovery, resulting in higher compressor efficiency. Impeller efficiency is not affected by the radial gap. The experimental results are published as an open CFD test case under the name "Radiver."

KAI U. ZIEGLER, HEINZ E. GALLUS, REINHARD NIEHUIS [9]

The interaction between impeller and diffuser affects flow in centrifugal compressors. A two-part paper investigates the effect of impeller-diffuser interaction on unsteady and time averaged flow configuration. Smaller radial gaps improve diffuser pressure recovery and impeller efficiency. The experimental results are intended to be published as an open CFD testcase under the name "Radiver."

CHAPTER I: THEORY

I.1. INTRODUCTION

Centrifugal compressors are used in small gas turbines and are the driven units in most gas turbine compressor trains. They are an integral part of the petrochemical industry, finding extensive use because of their smooth operation, large tolerance of process fluctuations, and their higher reliability compared to other types of compressors. The proper selection of a compressor is a complex and important decision. The successful operation of many plants depends on smooth and efficient compressor operations. To ensure the best selection and proper maintenance of a centrifugal compressor, the engineer must have a knowledge of many engineering disciplines. [12]

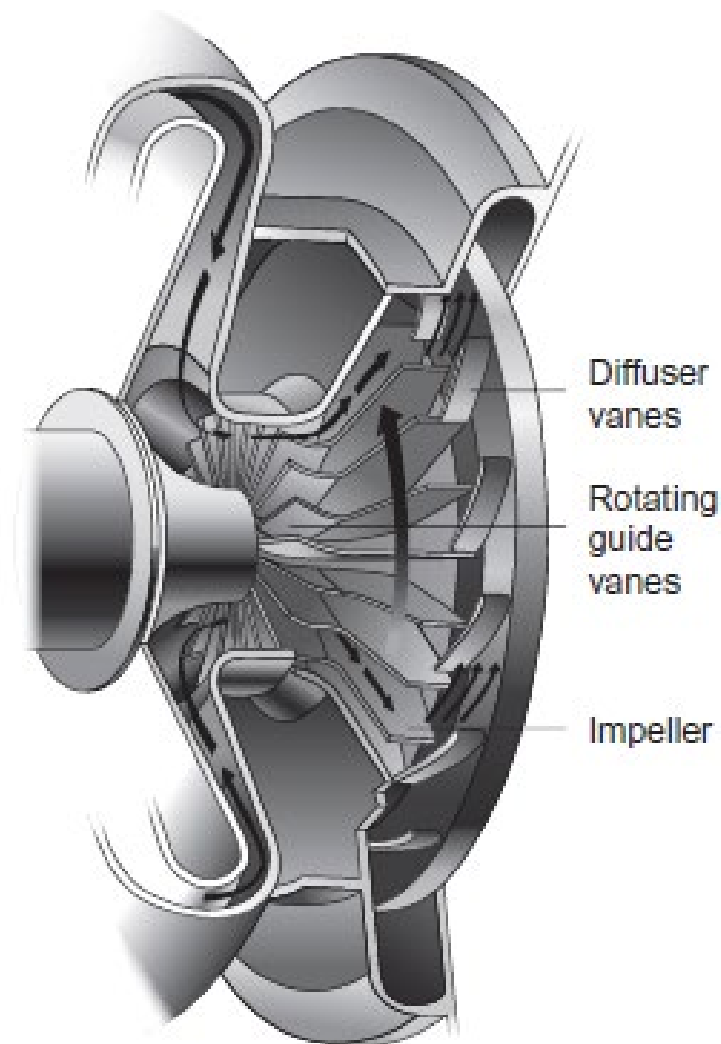


Figure I.1.1. A version of the centrifugal compressor used by Sir Frank Whittle.

In a typical centrifugal compressor, the fluid is forced through the impeller by rapidly rotating impeller blades.

The velocity of the fluid is converted to pressure, partially in the impeller and partially in the stationary diffusers. Most of the velocity leaving the impeller is converted into pressure energy in the diffuser as shown in **Figure I.1.2**. It is normal practice to design the compressor so that half the pressure rise takes place in the impeller and the other half in the diffuser. The diffuser consists essentially of vanes, which are tangential to the impeller. [13]

These vane passages diverge to convert the velocity head into pressure energy. The inner edges of the vanes are in line with the direction of the resultant airflow from the impeller as shown in **Figure I.1.3**.

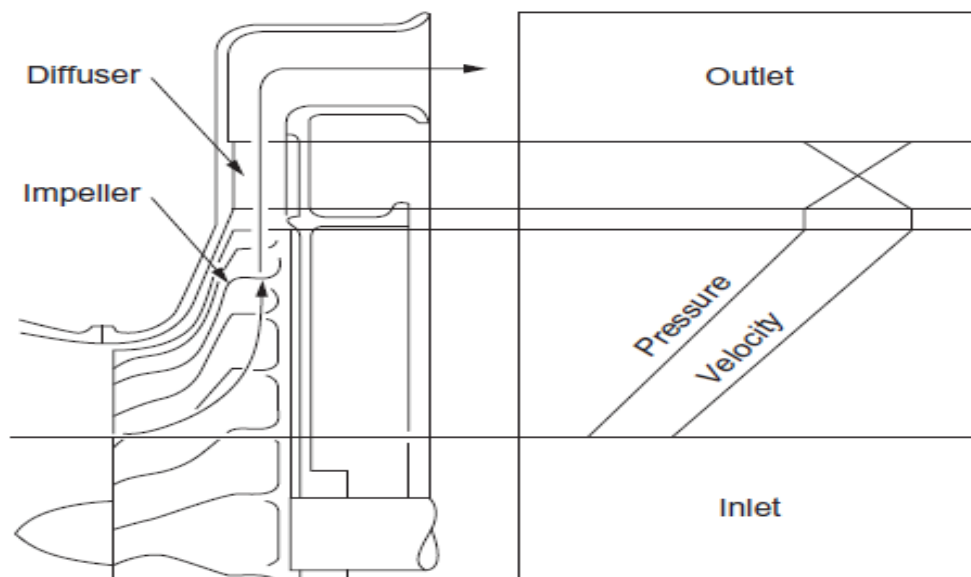


Figure I.1.2. Pressure and velocity through a centrifugal compressor.

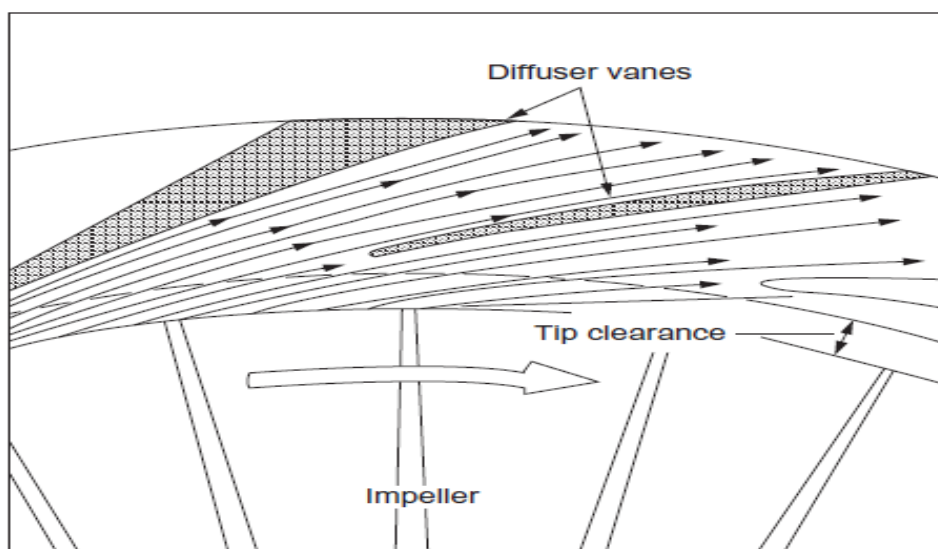


Figure I.1.3. Flow entering a vaned diffuser.

I.2. CENTRIFUGAL COMPRESSOR COMPONENTS

Centrifugal compressors are dynamic machines that achieve a pressure rise by adding kinetic energy to a continuous flow of fluid through the impellers. The components of a centrifugal compressor include the inlet, impeller, outlet, diffuser, and volute. Each component plays a crucial role in the functioning of the compressor, ensuring efficient and reliable operation.

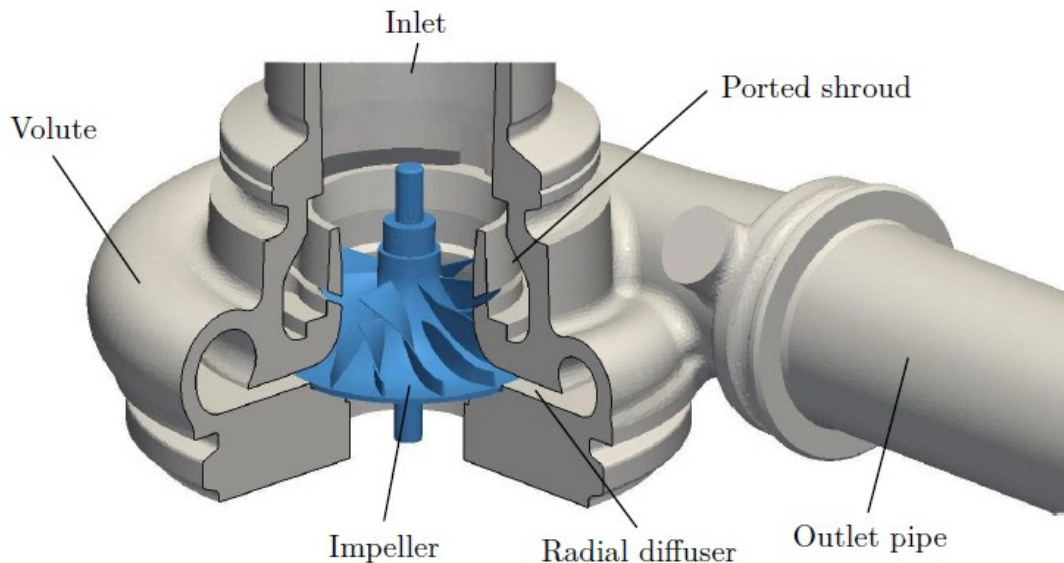


Figure I.2.1. Main components of a centrifugal compressor in isometric view.

I.2.1 The impeller

Impeller scoops in the working fluid (air/gas). Air is drawn at the center or eye of the impeller, then accelerated through the fast-spinning speed of the impeller and finally thrown out at the tip. The forces exerted on the air are centripetal. At the eye (inlet), the vanes are curved to induce the flow: this axial portion is called the inducer or rotating guide vane and may be integral with or separated from the main impeller.

The divergence (increasing cross-sectional area) of these passages diffuses (slows) the flow to a lower relative velocity and higher static pressure. The impeller is a complicated diffuser compared with the conventional straight conical diffuser as the passage is doubly curved first in the axial plane and then in the radial plane **Figure I.2.2**. The impeller vanes are aligned radially, but may be curved near the tip, having forward or backward configurations.

The impeller may have double sides (sometimes denoted double entry), to pass the maximum flow rate relative to its diameter and to balance the stresses of single-sided impeller.

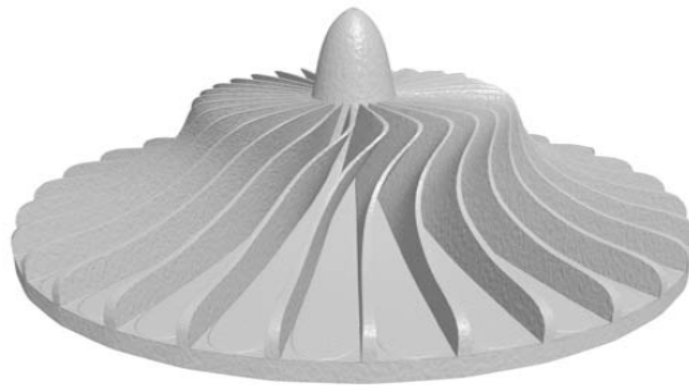


Figure I.2.2. Impeller shape.

The vanes are cast, forged, or machined integrally with the impeller hub. The hub is the curved surface of revolution extending from the eye root to the outlet. The number of vanes is usually a prime number to avoid vibration problems .

The outer curve of the vanes is sealed by the shroud, which may be part of the stationary structure or may rotate with the rotor. Typical impeller proportions are that the eye root diameter is about half the eye tip diameter, and the tip (outlet) diameter is nearly twice the eye tip diameter. [30]

I.2.2 The diffuser

The impeller blades sling the air radially outward where it is once again collected (at higher pressure) before it enters the diffuser. The diffuser represents a part of the fixed structure of the compressor.

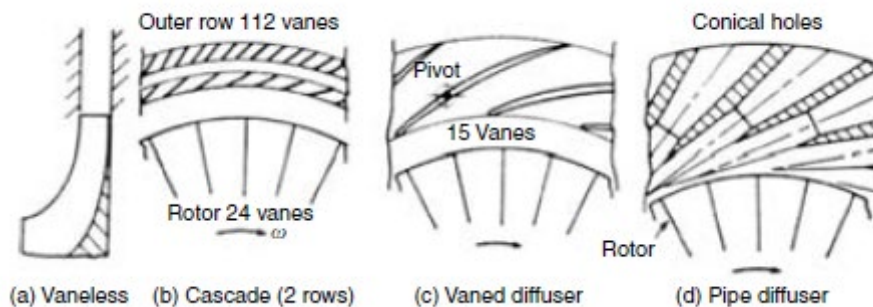


Figure I.2.3. Different types of diffuser.

It discharges air from the compressor impeller with a high absolute velocity and the role of diffusion is to reduce the kinetic energy, thereby increasing the static pressure. The diffuser is either a vaneless passage or a vaneless passage followed by a vaned section. The vaned diffuser represents a large group including the vanes together with the cascade, channel, and pipe types **Figure I.2.3**.

I.2.3 Scroll or Manifold

The final element of centrifugal compressors is either a manifold or a scroll. Centrifugal compressors with manifolds are used when the compressor is a part of a gas generator—in either a gas turbine or an aero engine—and thus the compressor is followed by a combustion chamber. In this case, the diffuser is bolted to the manifold, and often the entire assembly is referred to as the diffuser.

In case of industrial applications such as oil and gas industry (up-, mid-, and downstream), chemical industries and petrochemicals, iron and steel mining, and paper industry, the working fluid is collected in a scroll or volute. The working fluid leaving the stators is collected in a spiral casing surrounding the diffuser called a *volute* or *scroll*. The area of the cross section of the volute increases along the flow path in such a way that the velocity remains constant. Finally, the total fluid leaving all the stator passages is ejected from a pipe/duct normal to the inlet duct. The possible shapes of volute are shown in **Figure I.2.4**. [14]

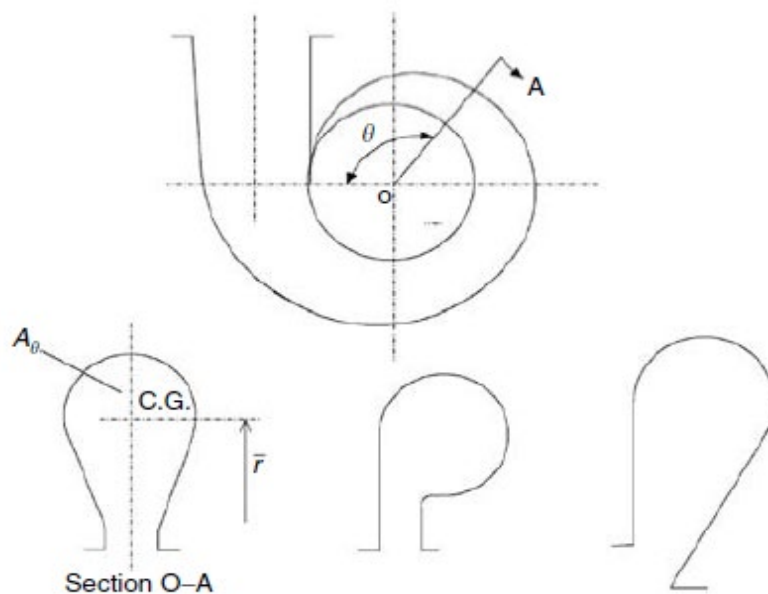


Figure I.2.4. Different shapes of volute. (From H.I.H. Saravanamuttoo, GFC Rogers and H Cohen, Gas Turbine Theory, 5th edn., Prentice Hall, 2001, p. 167.)

I.3. VELOCITY TRIANGLES OF CENTRIFUGAL COMPRESSORS

Velocity triangles are an important tool for analyzing the performance of centrifugal compressors. They provide a graphical representation of the velocities at the inlet and outlet of the impeller, allowing for the calculation of various parameters such as work input, pressure rise, and efficiency.

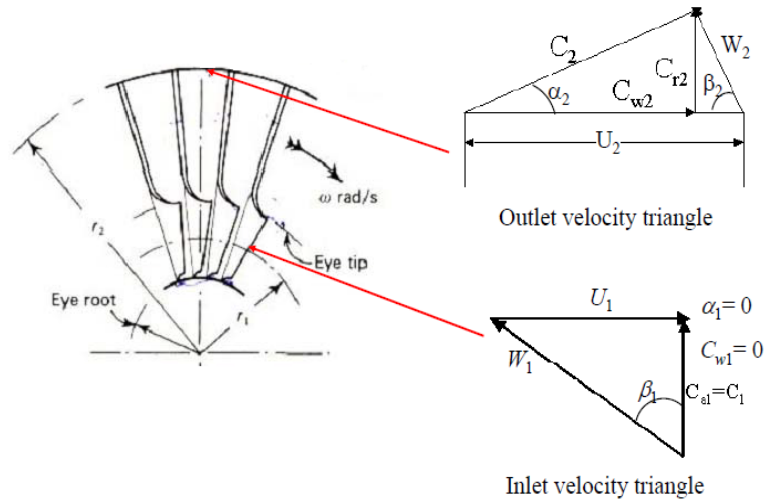


Figure I.3.1. Velocity Triangles of Centrifugal Compressors

I.3.1 Inlet Velocity Triangle

At the impeller inlet, the air enters axially with an absolute velocity c_{a1} . The impeller rotates with a tangential velocity u_1 , creating a whirl velocity c_{w1} . The relative velocity w_1 is the vector sum of c_{a1} and u_1 . The inlet velocity triangle is plotted in the axial plane containing the shaft axis.

I.3.2 Impeller Velocity Triangles

As the air flows through the impeller, its velocity and direction change. The relative velocity w increases due to the centrifugal force, while the absolute velocity c increases in both magnitude and angle. The impeller can have three types of blade configurations:

1. Straight radial blades ($\beta_2 = 90^\circ$)
2. Forward-leaning blades ($\beta_2 < 90^\circ$)
3. Backward-leaning blades ($\beta_2 > 90^\circ$)

Forward-leaning blades are not commonly used due to inherent dynamic instability. Straight and backward-leaning blades are more commonly employed in modern centrifugal compressor

I.3.3 Outlet Velocity Triangle

At the impeller outlet, the air has an absolute velocity c_2 and a whirl velocity c_{w2} . The relative velocity w_2 is the vector difference between c_2 and u_2 . The outlet velocity triangle is plotted in the radial plane.

I.4. AERODYNAMICS OF CENTRIFUGAL COMPRESSORS

The blades, hub and casing of a centrifugal compressor impeller define channels that are supposed to guide the flow.

However, certain phenomena occur that prevent the fluid from being perfectly channeled. The term main flow refers to the fraction of the flow that follows the geometry, as opposed to secondary flow, which refers to the components of the flow in planes orthogonal to the main direction.

Analysis of the forces created by the main flow helps us to understand the pressure gradients established in a centrifugal compressor.

They also help to explain the formation of secondary flows, a major source of losses in turbomachinery. [15]

I.4.1 Main flow (Analysis of the forces)

Writing Euler's equations in the moving (or relative) reference frame linked to the impeller reveals the forces acting on the fluid particles. Since the reference frame is non-Galilean, the centrifugal and Coriolis accelerations appear as external forces.

Apart from the pressure gradient, four forces must be taken into account, expressed here in the reference frame linked to the particle (*Frenet trihedron*):

- the force of inertia linked to the variation in speed of the particle on its trajectory (expressed here per unit volume):

$$F_{inertia} = -\rho W \frac{\partial W}{\partial s} u_s \quad (1.4.1)$$

The direction of this force is given by the trajectory, u_s representing the unit vector tangent to the trajectory at the point under consideration. In a compressor, the particles are generally slowed down over most of their path, and so $\partial W/\partial s$ is often negative;

- the centrifugal force induced by the rotation of the impeller (see Figure 2.11 for a meridian view), which is written as :

$$F_{centrifugal-rotation} = -\rho\Omega \times (\Omega \times r) \quad (1.4.2)$$

where $\Omega = \Omega u_z$ is the rotation vector of the frame. Noting r , the distance to the axis of rotation (in orthogonal projection), and u_r the radial direction vector, the centrifugal force

is expressed as :

$$F_{centrifugal-rotation} = \rho\Omega^2 r u_r \quad (1.4.3)$$

The direction of this force, u , is therefore strictly linked to the fixed reference given by the axis of rotation:

- the Coriolis force due to the rotation of the wheel :

$$F_{coriolis} = -2\rho\Omega W \quad (1.4.4)$$

Since the Coriolis force is given by a vector product involving relative speed, its direction depends directly on the particle's trajectory in the wheel's frame of reference (see **Figure I.4.1** for a representation in a blade-to-blade plane);

- finally, as the trajectory in the relative reference frame is itself curved, we introduce the centrifugal force due to the curvatures. Its expression is roughly analogous to the centrifugal force due to rotation:

$$F_{centrifugal-curvature} = -\rho\Omega_c \times (\Omega_c \times r) \quad (1.4.5)$$

where Ω_c denotes the 'instantaneous rotation vector', which allows the curvature effect to be treated as a rotation effect :

$$\Omega_c = -\frac{W}{R_c}u_b \quad (1.4.6)$$

with bi-normal vector, defined to form a direct trihedron with u_s and u_n , and R_c the (local) radius of curvature of the particle's trajectory. Finally, we can write :

$$F_{\text{centrifugal-curvature}} = \rho \frac{W^2}{R_c} u_n \quad (1.4.7)$$

Neglecting viscous effects, the projection of these forces onto the reference surfaces gives an initial assessment of the pressure gradients in the wheel.

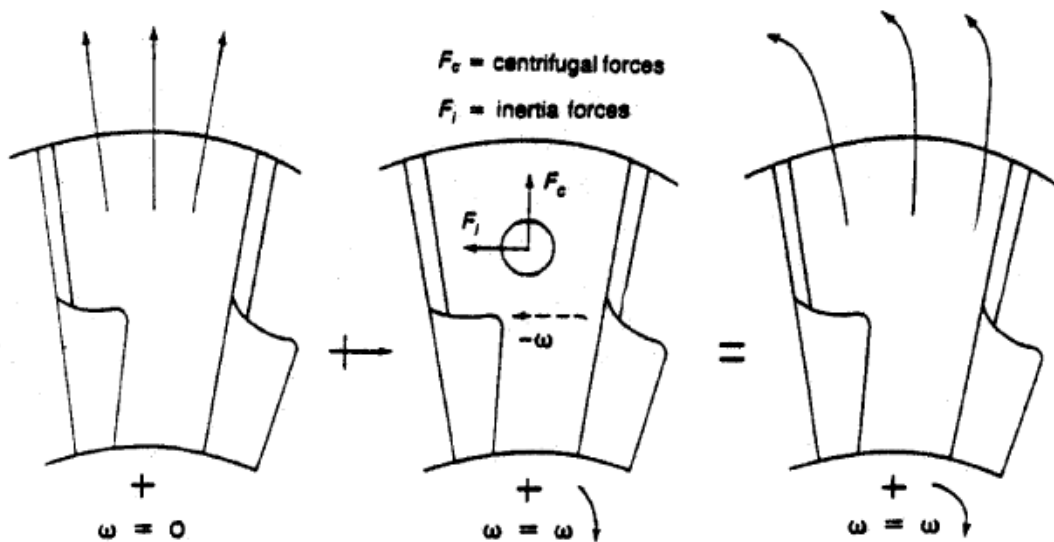


Figure I.4.1. Forces and flow characteristics in a centrifugal compressor.

I.4.2 Secondary flow

Secondary flow is defined as the components of the relative velocities in the plane orthogonal to the direction of the main flow.

According to Brads how , vortex flows known as secondary flows form due to viscous effects on the casing and hub walls, which deflect the main flow.

The characteristics of the secondary flow are :

- a highly three-dimensional and non-stationary character.
- the presence of longitudinal whorls.
- strong interaction with the main flow.

I.5. THE REFERENCE PLANES IN A CENTRIFUGAL COMPRESSOR

Flow in a centrifugal compressor is three-dimensional, viscous, turbulent and generally compressible. To simplify the study and analysis of internal flow, two types of reference surfaces are shown in **Figure I.5.1**.

This decomposition gives rise to two types of flow:

Meridian flow.

blade-to-blade flow.

For each type of surface there are in fact an infinite number of meridian and blade-to-blade planes, so we generally limit ourselves to studying a single mean meridian plane projected onto the (z, r) plane and the blade-to-blade surfaces are presented by conformal transformation in the $R(z, r)$ plane following the law $d\theta = dmr \cdot \tan(\beta)$ and orthogonal sections that can be considered as quasi-plane see **Figure I.5.1**.

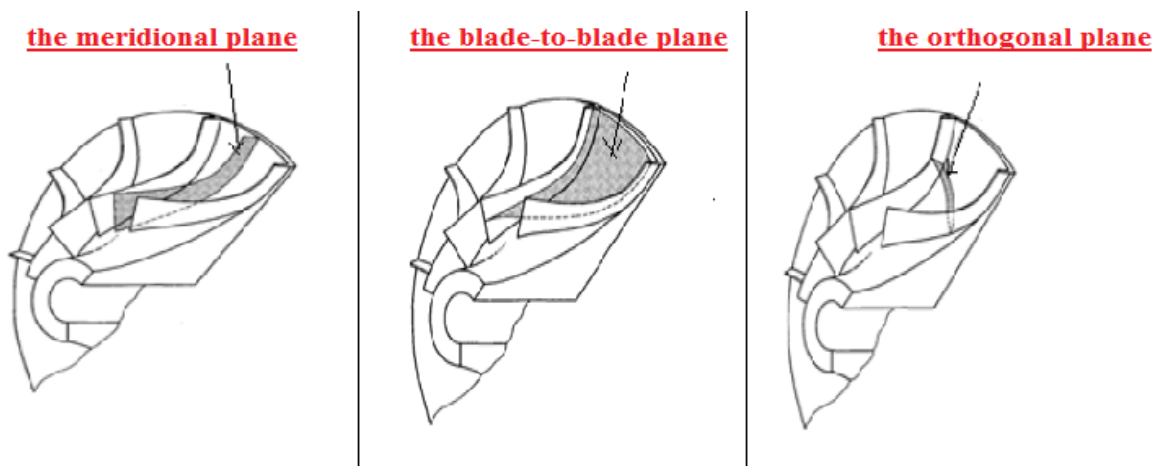


Figure I.5.1. Reference surfaces in the centrifugal compressor impeller.

I.6. CENTRIFUGAL COMPRESSOR CHARACTERISTICS

The performance of compressible flow machines is usually described in terms of the groups of variables derived in dimensional analysis. These characteristics are dependent on other variables such as the conditions of pressure and temperature at the compressor inlet and physical properties of the working fluid. To study the performance of a compressor completely,

it is necessary to plot P_{03}/P_{01} against the mass flow parameter $m \frac{\sqrt{T_{01}}}{P_{01}}$ for fixed speed intervals of $\frac{N}{\sqrt{T_{01}}}$, **Figure I.6.1** shows an idealized fixed speed characteristic.

Consider a valve placed in the delivery line of a compressor running at constant speed. First, suppose that the valve is fully closed. Then the pressure ratio will have some value as indicated by Point A. This pressure ratio is available from vanes moving the air about in the impeller

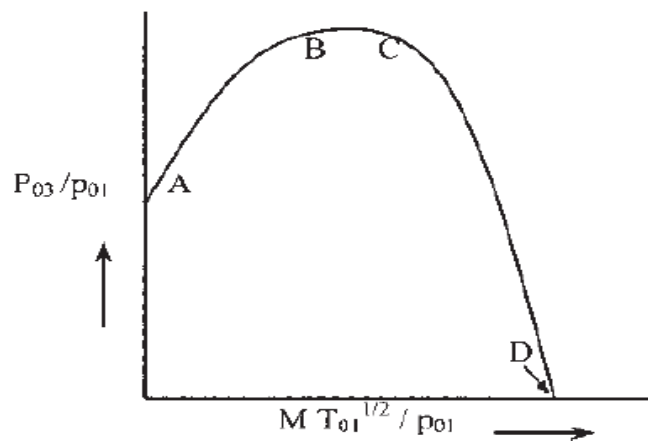


Figure I.6.1. The theoretical centrifugal compressor characteristic.

Now, suppose that the valve is opened and airflow begins. The diffuser contributes to the pressure rise, the pressure ratio increases, and at Point B, the maximum pressure occurs. But the compressor efficiency at this pressure ratio will be below the maximum efficiency. Point C indicates the further increase in mass flow, but the pressure has dropped slightly from the maximum possible value. This is the design mass flow rate pressure ratio.

Further increases in mass flow will increase the slope of the curve until point D. Point D indicates that the pressure rise is zero. However, the above-described curve is not possible to obtain.

I.6.1 STALL

Stalling of a stage will be defined as the aerodynamic stall, or the breakaway of the flow from the suction side of the blade airfoil. A multistage compressor may operate stably in the unsurged region with one or more of the stages stalled, and the rest of the stages unstalled. Stall, in general, is characterized by reverse flow near the blade tip, which disrupts the velocity

distribution and hence adversely affects the performance of the succeeding stages.

Referring to the cascade of **Figure I.6.2**, it is supposed that some nonuniformity in the approaching flow or in a blade profile causes blade B to stall. The air now flows onto blade A at an increased angle of incidence due to blockage of channel AB. The blade A then stalls, but the flow on blade C is now at a lower incidence, and blade C may unstall.

Therefore, the stall may pass along the cascade in the direction of lift on the blades. Rotating stall may lead to vibrations resulting in fatigue failure in other parts of the gas turbine.

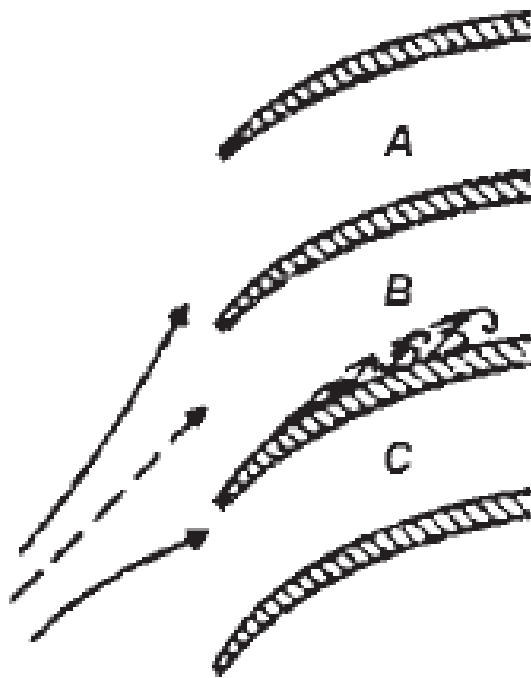


Figure I.6.2. Mechanism of stall propagation.

I.6.2 SURGING

Surging is marked by a complete breakdown of the continuous steady flow throughout the whole compressor, resulting in large fluctuations of flow with time and also in subsequent mechanical damage to the compressor. The phenomenon of surging should not be confused with the stalling of a compressor stage.

Figure I.6.3 shows typical overall pressure ratios and efficiencies h_c of a centrifugal compressor stage. The pressure ratio for a given speed, unlike the temperature ratio, is strongly dependent on mass flow rate, since the machine is usually at its peak value for a narrow range of mass flows. When the compressor is running at a particular speed and the discharge is

gradually reduced, the pressure ratio will first increase, peaks at a maximum value, and then decreased.

The pressure ratio is maximized when the isentropic efficiency has the maximum value. When the discharge is further reduced, the pressure ratio drops due to fall in the isentropic efficiency. If the downstream pressure does not drop quickly there will be backflow accompanied by further decrease in mass flow. In the meantime, if the downstream pressure drops below the compressor outlet pressure, there will be increase in mass flow. This phenomenon of sudden drop in delivery pressure accompanied by pulsating flow is called surging. The point on the curve where surging starts is called the surge point. When the discharge pipe of the compressor is completely choked (mass flow is zero) the pressure ratio will have some value due to the centrifugal head produced by the impeller. [16]

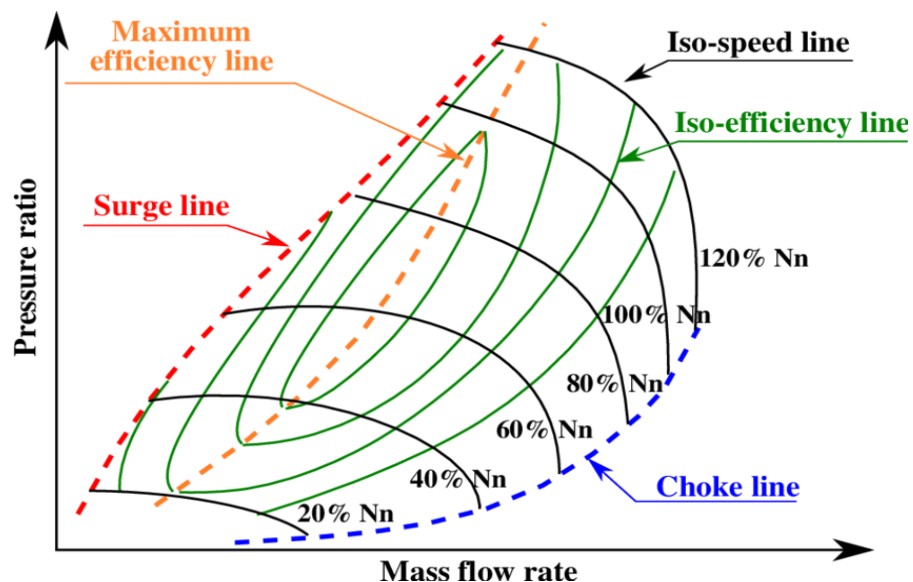


Figure I.6.3. Centrifugal compressor characteristics.

Between the zero-mass flow and the surge point mass flow, the operation of the compressor will be unstable. The line joining the surge points at different speeds gives the surge line.

I.6.3 CHOKING

When the velocity of fluid in a passage reaches the speed of sound at any cross-section, the flow becomes choked (air ceases to flow). In the case of inlet flow passages, mass flow is constant. The choking behavior of rotating passages differs from that of the stationary passages, and therefore it is necessary to make separate analysis for impeller and diffuser, assuming one dimensional, adiabatic flow, and that the fluid is a perfect gas.

I.6.4 THE OPERATING RANGE

The operating range of a compressor is important, and can be defined by the following relationship:

$$range = \frac{\dot{m}_{choke} - \dot{m}_{surge}}{\dot{m}_{no\ min\ al}} \quad (1.6.1)$$

I.7. LOSSES

The accurate calculation and proper evaluation of losses within a centrifugal compressor is as important as the calculation of the blade-loading parameters. If the proper parameters are not controlled, efficiency decreases. The evaluation of various losses is a combination of experimental results and theory. The losses are divided into two groups: losses encountered in the rotor, and losses encountered in the stator.

A loss is usually expressed as a loss of heat or enthalpy. A convenient way to express them is in a non-dimensional manner with reference to the exit blade speed.

I.7.1 Rotor Losses

Rotor losses are divided into the following categories:

Shock in Rotor Losses : This loss is due to shock occurring at the rotor inlet.

Incidence Loss : At off-design conditions, flow enters the inducer at an incidence angle that is either positive or negative.

Disc Friction Loss : This loss results from frictional torque on the back surface of the rotor.

Diffusion-Blading Loss : This loss develops because of negative velocity gradients in the boundary layer.

Clearance Loss : When a fluid particle has a translatory motion relative to a non-inertial rotating coordinate system, it experiences the Coriolis force.

Skin Friction Loss : Skin friction loss is the loss from the shear forces on the impeller wall caused by turbulent friction.

I.7.2 Stator Losses

stator losses are divided into the following categories:

Recirculating Loss : This loss occurs because of backflow into the impeller exit of a compressor and is a direct function of the air exit angle.

Wake-Mixing Loss : This loss is from the impeller blades, and it causes a wake in the vaneless space behind the rotor.

Vaneless Diffuser Loss : This loss is experienced in the vaneless diffuser and results from friction and the absolute flow angle.

Vaned Diffuser Loss : Vaned diffuser losses are based on conical diffuser test results. They are a function of the impeller blade loading and the vaneless space radius ratio.

Exit Loss : *The exit loss assumes that one-half of the kinetic energy leaving the vaned diffuser is lost.*

I.8. PERFORMANCE PREDICTION

Performance prediction is a critical aspect of centrifugal compressor design and operation. It involves calculating various performance parameters such as pressure ratio, flow rate, and efficiency, which can help optimize the compressor's performance and energy efficiency. Inaccurate prediction of these parameters can lead to suboptimal performance, resulting in increased energy consumption and a decreased lifespan of the compressor. Being able to predict a compressors' performance reliably and relatively accurately therefore introduces great benefits for both the design and operation of centrifugal compressors. To design and optimize the performance of centrifugal compressors, a wide variety of methods has been developed and applied over the years. [17]

CHAPTER II:
MATHEMATICAL MODEL

II.1. INTRODUCTION

The mathematical model is formulated from the physical behavior mentioned in the problem statement. Fluid flow equations are basically created from differential equations demonstrating the relationship linking flow variables and respective flow coordinates in space and time.

II.2. COMPRESSOR THERMODYNAMICS

II.2.1 Total-to-Total Efficiency

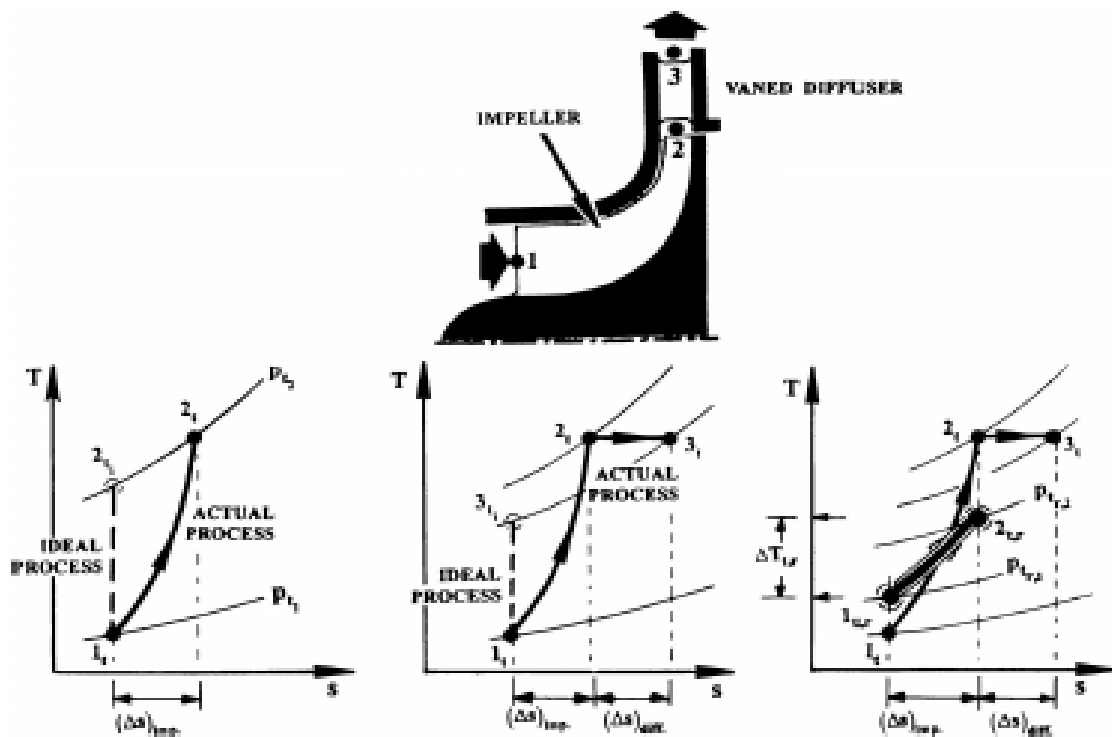


Figure II.2.1. The impeller flow process on a total-to-total and total-relative-to-total-relative.

Being a power-absorbing turbomachine, the total-to-total efficiency (η_{t-t}) is defined as the ideal-to-actual shaft-work ratio. In this statement, the former (ideal) shaft work is the minimum magnitude that would lead to the same total-to-total pressure ratio the actual process does. Assuming an adiabatic flow and a fixed specific-heat ratio (γ), the total-to-total efficiency can be expressed, in light of **Figure II.2.1**, as :

$$\eta_{t-t} = \frac{\left(\frac{p_{t3}}{p_{t1}}\right)^{\frac{\gamma-1}{\gamma}} - 1}{\left(\frac{T_{t3}}{T_{t1}}\right) - 1} \quad (2.2.1)$$

where stations 1 and 3 are the impeller inlet and diffuser exit stations, respectively **Figure II.2.2**. By focusing on these two stations, we are implicitly assuming that the volute is nonexistent or its effect negligible, which is not necessarily the case.

II.2.2 Total-to-Static Efficiency

Maximizing the static pressure recovery, across the compressor diffuser and volute, is one of the most important tasks. This holds true regardless of whether the outlet stream feeds into the combustor or a discharge vessel.

In this sense, it is the total to- static efficiency that is naturally the focus of attention, more so than the total-to total efficiency.

Following a logic that is similar to the derivation of the same in the turbine/exhaust diffuser case, the total-to-static efficiency here can be expressed, by reference to **Figure II.2.1**, as follows

$$\eta_{t-s} = \frac{\left(\frac{p_3}{p_{t1}}\right)^{\frac{\gamma-1}{\gamma}} - 1}{\left(\frac{T_{t3}}{T_{t1}}\right) - 1} \quad (2.2.2)$$

Comparing the contents of **(2.2.2)** to those of the total-to-total efficiency, it is clear that

$$\eta_{t-s} < \eta_{t-t} \quad (2.2.3)$$

This is identical to the conclusion reached in the turbine/exhaust-diffuser counterpart. The efficiency difference in expression **(2.2.3)** is indicative of the designer's skill and carefulness.

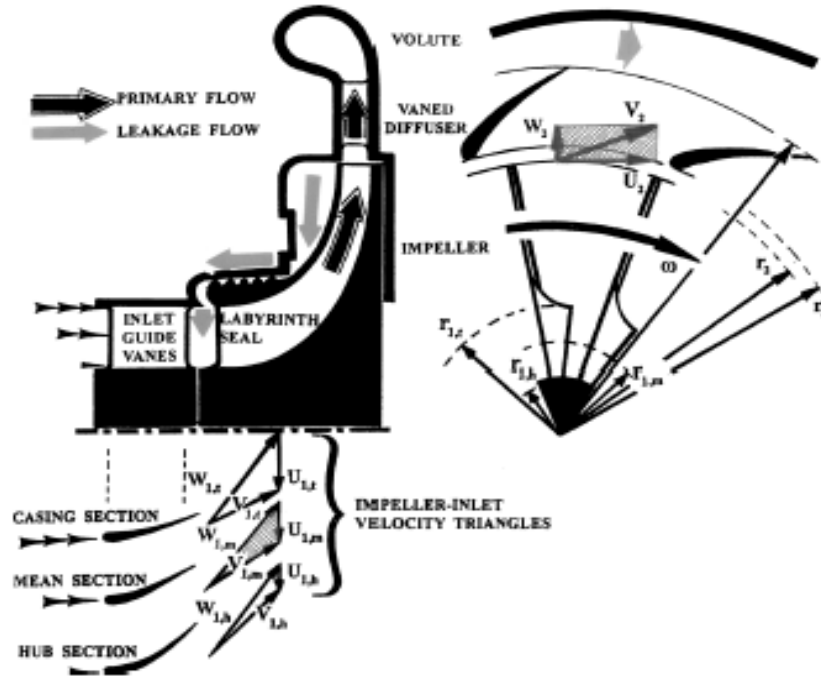


Figure II.2.2. Preswirl guide vanes eliminate the need to twist the impeller inlet segment.

II.2.3 Corrected Compressor Mass Flow

$$M_{corr} = \frac{M_{act} \sqrt{\frac{T_1}{T_{ref}}}}{\frac{P_1}{P_{ref}}} \frac{1}{\sqrt{\frac{MW_{act}}{MW_{ref}}}} \quad (2.2.4)$$

where M_{corr} and M_{act} is the corrected and actual mass flow, and P_{ref} , T_{ref} , MW_{ref} are the Pressure, Temperature, and Molecular Weight at reference conditions, such as design inlet conditions.

II.2.4 Corrected Pressure

$$P_{corr} = \frac{P_{act}}{\frac{P_1}{P_{ref}}} \quad (2.2.5)$$

where P_{corr} and P_{act} are the compressor's corrected and actual Total Pressure.

II.2.5 Corrected Temperature

$$T_{corr} = \frac{T_{act}}{\sqrt{\frac{T_1}{T_{ref}}}} \frac{MW}{MW_{ref}} \quad (2.2.6)$$

where T_{corr} and T_{act} are the compressor's corrected and actual Total Temperature.

The Compressor Performance map is a typical performance map of a centrifugal compressor. The map shows a variation of the total pressure ratio or Head as a function of the corrected compressor mass flow at various aerodynamic speeds. The mass flow is corrected for pressure and temperature, and the mechanical speed is corrected for temperature. In this manner, the map can be used to check the performance of a compressor at variable inlet conditions for a given gas. These maps sometimes can be further modified to also account for changes in molecular weight.

II.3. GOVERNING EQUATIONS

3D CFD simulations made for this thesis dissertation were solved using ANSYS CFX commercial CFD solver. The set of equations solved by ANSYS CFX are the unsteady Navier-Stokes equations in conservative form. The basic instantaneous compressible equations of mass, momentum and energy conservation in stationary frame are respectively:

$$\frac{\partial \rho}{\partial t} + \frac{\partial(\rho W_i)}{\partial x_i} = 0 \quad (2.3.1)$$

$$\frac{\partial(\rho W_i)}{\partial t} + \frac{\partial(\rho W_i W_j)}{\partial x_j} + \frac{\partial p}{\partial x_i} = \frac{\partial \tau_{ij}}{\partial x_j} + S_M \quad (2.3.2)$$

$$\frac{\partial(\rho h_0)}{\partial t} - \frac{\partial q}{\partial t} + \frac{\partial(\rho W_i h_0)}{\partial x_i} + \frac{\partial(W_i p)}{\partial x_i} = \frac{\partial}{\partial x_i} \left(\lambda \frac{\partial T}{\partial x_j} \right) + \frac{\partial(W_j \tau_{ij})}{\partial x_i} + W_i S_M + S_E \quad (2.3.3)$$

The stress tensor τ_{ij} is defined as:

$$\tau_{ij} = \frac{2}{3} \mu \delta_{ij} \frac{\partial W_k}{\partial x_k} + \mu \left(\frac{\partial W_j}{\partial x_i} + \frac{\partial W_i}{\partial x_j} \right) \quad (2.3.4)$$

Please note that dissimilarity to the previous chapters, the velocity terms used in this section are Reynolds averaged values unless otherwise specified. The energy equation is based on the total enthalpy h_0 .

$$h_0 = h + \frac{C^2}{2} \quad (2.3.5)$$

S_M and S_E are respectively the momentum and energy source terms, and λ is the thermal conductivity constant of the wall material. q is the heat flow per unit volume.

ANSYS CFX calculates the pressure and static enthalpy and obtains solution for density and/ or temperature since the equations of state expressing the density as a function of both pressure and temperature.

$$\rho = \frac{w(p + p_{ref})}{RT} \quad (2.3.6)$$

The specific heat may also be described as a function of both pressure and temperature.

$$c_p = c_p(p, T) \quad (2.3.7)$$

With ANSYS CFX, the compressible flow modelling is activated by selection of the energy equation based on total enthalpy h_0 in conjunction with the ideal gas equation of state.

II.4. ROTATIONAL MODEL

For models of rotational components that create Coriolis force and centrifugal force in the fluid, it is necessary to model the appropriate momentum source SM in the momentum and energy equations. The Coriolis force and centrifugal force are given as

$$S_{cor} = -2\rho\omega \times U \quad (2.4.1)$$

$$S_{cfs} = -\rho\omega \times (\omega \times r) \quad (2.4.2)$$

Hence the steady state momentum equation becomes

$$\frac{\partial(\rho C_i C_j)}{\partial x_j} + \frac{\partial p}{\partial x_i} = \frac{\partial \tau_{ij}}{\partial x_j} - 2\rho\omega \times U - \rho\omega \times (\omega \times r) \quad (2.4.3)$$

As the computation of rotational model is made in a rotational frame of reference, it will modify the advection term to include the absolute frame velocity. The momentum equation then becomes

$$\frac{\partial(\rho W_i W_{j,abs})}{\partial x_j} + \frac{\partial p}{\partial x_i} = \frac{\partial \tau_{ij}}{\partial x_j} - 2\rho\omega \times U - \rho\omega \times (\omega \times r) \quad (2.4.4)$$

II.5. TURBULENCE MODELING

The outstanding feature of a turbulent flow, in the opposite to a laminar flow, is that the molecules move in a chaotic fashion along complex irregular path. The strong chaotic motion causes the various layers of the fluid to mix together intensely.

Because of the increased momentum and energy exchange between the molecules and solid walls, turbulent flow leads at the same conditions to higher skin friction and heat transfer as compared to laminar flow.

Although the chaotic fluctuations of the flow variables are of deterministic nature, the simulation of turbulent flows still continues to present a significant problem. Despite the performance of modern supercomputers, a direct simulation of turbulence by the time-dependent Navier-Stokes equations (5.1) .

$$\frac{\partial}{\partial t} \int_{\Omega} \vec{W} d\Omega + \oint_{\partial\Omega} (\vec{F}_c - \vec{F}_v) dS = \int_{\Omega} \vec{Q} d\Omega \quad (2.5.1)$$

—known as the *direct numerical simulation* (DNS) is applicable only to relatively simple flow problems at low Reynolds numbers (Re) in the order of 104-105. A more widespread utilization of the DNS is prevented by the fact that the number of grid points needed for sufficient spatial resolution scales as $Re^{9/4}$ and the CPU-time as Re^3 .

Therefore, we are forced to account for the effects of turbulence in an approximate manner.

For this purpose, a large variety of *turbulence models* was developed and the research still goes on. There are five principal classes of turbulence models:

- *algebraic*,
- *one-equation*,

- *multiple-equation*,
- *second-order* closures (Reynolds-stress models),
- *large-eddy simulation* (LES).

The first three models belong to the so-called *first-order* closures. They are based mostly on the *eddy-viscosity* hypothesis of Boussinesq, but for certain applications also on *non-linear eddy-viscosity* formulations.

An overview of the classes of turbulence models, which are sorted according to their decreasing level of complexity, is displayed in **Figure II.5.1**.

One should be aware of the fact that there is no single turbulence model, which can predict reliably all kinds of turbulent flows. Each of the models has its strengths and weaknesses. For example, if a particular model works perfectly in the case of attached boundary layers, it may fail completely for separated flows.

Thus, it is important always to ask whether the model includes all the significant features of the flow being investigated. Another point which should be taken into consideration is the computational effort versus the accuracy required by the particular application.

We mean by this that in many cases a numerically inexpensive turbulence model can predict some global measures with the same accuracy as a more complex model. [18]

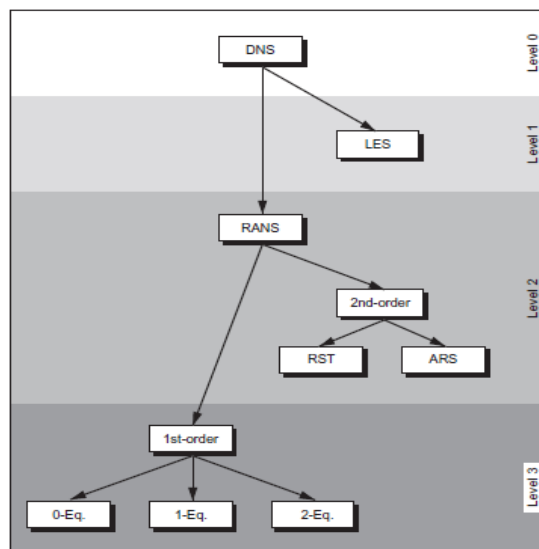


Figure II.5.1. Hierarchy of turbulence models.

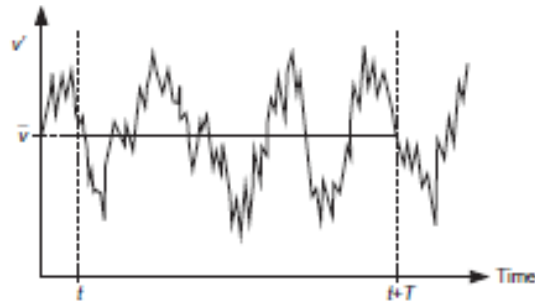


Figure II.5.2. Reynolds averaging—illustration of turbulent velocity fluctuations v' and statistical mean.

II.5.1 Direct Numerical Simulation (DNS)

In DNS, the Navier–Stokes equations are solved directly with refined meshes capable of resolving all turbulent length scales. These simulations calculate the mean flow along with all turbulent velocity fluctuations. DNS has potential for simulation of complex turbulent flows, and algorithms for solving 3D continuity and Navier–Stokes equations are well established. These calculations come with high costs in terms of computational resources, so this approach is not commonly applied for industrial flow computations.

DNS is expected to play a progressively important part in turbulence research in the immediate future. DNS methods need extremely fine, fully 3D meshes, huge computers, and a massive amount of CPU time.

At present computational capabilities, DNS results are not yet realizable for highly turbulent flows in engineering applications.

II.5.2 Large Eddy Simulation (LES)

The LES is an alternate approach toward realizing more capable turbulent flow calculations. A far more refined mesh than the RANS system of equations is used in LES. The precision of LES in terms of performance and ability is someplace between RANS and the Direct Numerical Simulation (DNS). The largest eddies are normally equivalent in size to the characteristic length of the average flow. The lowest scales are accountable for the liberation of turbulence kinetic energy. There are two major steps involved in LES analysis: filtering and subgrid scale (SGS) modeling. Filtering is used for solving the large eddies involved while the SGS model addresses the small eddies that are unresolved in the filtering method.

Large unsteady turbulent eddies are proposed using this technique, though small scale dissipative turbulent eddies are modeled. The basic theory is that the smaller turbulent eddies are not dependent on coordinate system orientation and will always act in a statistically parallel and expectable manner, regardless of the turbulent flow field.

The main limitation of LES lies in the wall boundary layers that require high-resolution grids. Even big eddies convert to small eddies near the wall and need a Reynolds number dependent resolution. [20]

II.5.3 RANS

(Reynolds–Averaged Navier-Stokes) This approach is based on a statistical treatment of the Navier-Stokes equations, using the Reynolds decomposition.

When the flow is turbulent, it is possible to decompose any vector or scalar quantity into an average part and a fluctuating part. The average part is generally denoted by : $(\overline{\dots})$, and the fluctuating term by (\dots') . Following the properties of statistical averages , this approach is valid for all stationary or transient cases.

The non-linearity of the equations leads, in this processing model, to the appearance of new additional unknown terms, known as Reynolds tensions.

They introduce six additional unknowns without, however, adding any additional equations to the system. This gives a total of 4 equations for 10 unknowns, in other words, the classical system of equations becomes open (the number of unknowns is greater than the number of equations).

To solve the system, we therefore need to close it with complementary equations, the so-called closure equations.

Modelling the Reynolds stress term according to one of the turbulence models is based on the Boussinesq hypothesis, which relates Reynolds stresses to the mean rate of deformation of the flow:

- In this equation, we note the presence of two new variables used to model the Reynolds tensor, the turbulent viscosity μ_t and the kinetic energy k . We need two additional pieces of information to close the RANS equation system, but they must be used to deduce information about the velocity, length and characteristic time of the fluctuations.

- There are several types of two-equation turbulence models which are widely used in CFD simulations, because on the one hand they give a good compromise between the effort and accuracy of the numerical calculation and on the other hand they are much more sophisticated than zero equation models.
- In two-equation models, the turbulent velocity scale is calculated from the turbulent kinetic energy, which is provided by the solution of the transport equation.
- The turbulent length scale is estimated from two properties of the turbulence field, generally the turbulent kinetic energy and the dissipation rate.
- The dissipation rate of the turbulent kinetic energy is provided by the solution of the transport equation.

II.6. ALGEBRAIC (OR ZERO-EQUATION) MODELS

The most straightforward definition of V and L is with the so-called algebraic (or zero equation) class of models. These assume that V and L can be related by algebraic equations to the local properties of the flow, which is a straightforward process for two-dimensional boundary layer flows but can often be difficult in geometrically complex configurations. A version sometimes used in turbomachinery calculations is that from Baldwin and Lomax (1978). For example, in a simple wake or free shear layer, V is often taken as proportional to the velocity difference across the flow and L is taken as constant and proportional to the width of the layer. In a boundary layer close to the wall, V is given as $L \cdot \partial c / \partial y$ (or $L \cdot \Omega$ where Ω is the magnitude of the vorticity) and L is related to the wall-normal distance from the wall (y -direction). The outer part of the boundary layer is treated similarly to a wake. [21]

This is the main reason why these models are generally not recommended for turbomachinery applications of RANS methods. The model of Baldwin and Lomax (1978) is an algebraic two-layer turbulence model with the turbulent eddy viscosity defined by one expression in the inner layers close to the wetted surfaces and a different expression in the outer layers. The distinguishing feature of their model is the use of a function constructed from the product of vorticity and distance from the nearest surface.

This function has a sharp peak at a certain distance from the wall, and its location determines the changes in the equations for the mixing length in the inner and outer layer.

II.7. ONE-EQUATION MODELS

The one-equation models attempt to improve on the zero-equation models by using a turbulent eddy viscosity that no longer depends purely on the local flow conditions but considers the flow history, that is, where the flow has come from.

The majority of approaches seek to determine V and L separately and then to construct μ_t / ρ as the product of V and L . Almost without exception, V is identified with $k^{1/2}$, where k is the kinetic energy per unit mass of fluid arising from the turbulent fluctuations in velocity around the averaged velocity. A transport equation for k can be derived from the Navier-Stokes equations and this is the single transport equation in the one equation model. This equation is closed, i.e., reduced to a form involving only calculated variables, by introducing modelling assumptions.

II.7.1 Spalart-Allmaras

In turbulence models that use the Boussinesq approach, the main issue is how to calculate the turbulent viscosity. The model proposed by Spalart and Allmaras solves the transport equation for a quantity for which the shape of the kinematic turbulent viscosity has been modified.

The transport variable in the Spalart Allmaras model $\tilde{\nu}$ is identical to the turbulent kinematic viscosity except for the near-wall region. The transport equation $\tilde{\nu}$ for is :

$$\rho \frac{d\tilde{\nu}}{dt} = G_v + \frac{1}{\sigma_{\tilde{\nu}}} \left[\frac{\partial}{\partial x_j} \left\{ (\mu + \rho \tilde{\nu}) \frac{\partial \tilde{\nu}}{\partial x_j} \right\} + C_{b2} \rho \left(\frac{\partial \tilde{\nu}}{\partial x_j} \right)^2 \right] - Y_v \quad (2.7.1)$$

G is the production of the turbulent viscosity, is its destruction which occurs in the region close to the wall and is due to contact with the latter as well as the attenuation of the Viscosity.

With ν is the molecular kinematic viscosity. $\sigma_{\tilde{\nu}}$, C_{b2} are constants.

II.8. TWO-EQUATION MODELS

For general applications, it is usual to solve two separate transport equations to determine V and L , hence the name of the model. In combination with the transport equation for the

turbulent kinetic energy, k , an additional transport equation is solved for a quantity which determines the length scale, L .

This class of models is the best-known and the most widely used in industrial applications since it is the simplest level of closure which does not require geometry or flow regime–dependent input. Prior to the turn of the century, the most prevalent model was the k - ε model, where ε is the rate at which turbulent energy is dissipated to smaller eddies (Launder and Spalding, 1974). A modelled transport equation for ε is solved and L is then determined from the term $C_\mu K^{3/2} / \varepsilon$, where C_μ is a constant. This method is included in almost every commercial and inhouse code and is still heavily used in industrial applications. It has the merits of robustness and is useful for centrifugal compressor cases where the viscous effects are relevant, but the flow tends to be heavily influenced by three dimensional effects and rotational pressure gradients.

The k - ε model is less sensitive to free stream values but is often inadequate in adverse pressure gradients. Many different variants for circumventing this problem are found in the literature. An attractive option, the BSL (baseline) model has been proposed by Menter (1994) using a turbulence model, which retains the properties of k - ω close to the wall and gradually blends into the k - ε model away from the wall. This model has been shown to eliminate the free stream sensitivity problem without sacrificing the k - ω near-wall performance. [22]

The model (SST-CC) has been extensively tested on a wide range of both wall-bounded and free shear turbulent flows with system rotation and/or streamline curvature, including centrifugal compressor impellers (Smirnov et al.,2007). Gibson et al. (2017) have also found that the SST-CC improves the accuracy of the original SST model for modelling the flow in an impeller.

II.8.1 Standard Model k - ε

The k - ε model is the simplest of the complete two-equation models. This model assumes that the turbulent regime is fully established throughout the domain and that the effects of molecular viscosity are negligible compared with those of turbulent viscosity (away from the walls).It is based on the Boussinesq assumption that there is an analogy between the action of viscous forces and Reynolds stresses in mean flow. For high Reynolds numbers, the Reynolds stress terms are estimated by Launder & Spalding, (1974):

$$-\overline{\rho u_i u_j} = 2\mu S_{ij} - \frac{2}{3}\delta_{ij} - \frac{2}{3}\mu_i \delta_{ij} \frac{\partial U_k}{\partial x_k} \quad (2.8.1)$$

$$S_{ij} = \frac{1}{2} \left(\frac{\partial U_i}{\partial x_j} + \frac{\partial U_j}{\partial x_i} \right) \quad (2.8.2)$$

$$\rho \frac{d\tilde{v}}{dt} = G_v + \frac{1}{\sigma_{\tilde{v}}} \left[\frac{\partial}{\partial x_j} \left\{ (\mu + \rho\tilde{v}) \frac{\partial \tilde{v}}{\partial x_j} \right\} + C_{b2} \rho \left(\frac{\partial \tilde{v}}{\partial x_j} \right)^2 \right] - Y_v \quad (2.8.3)$$

S_{ij} is the deformation tensor.

The turbulent viscosity is given by :

$$\mu_t = \rho C_\mu \frac{k}{\varepsilon} \quad (2.8.4)$$

Where: $k = \frac{1}{2} \overline{u_i u_i}$ and $\varepsilon = \nu \left(\overline{\frac{\partial u_i}{\partial x_l} \frac{\partial u_i}{\partial x_l}} \right)$, are respectively the turbulent kinetic energy and its

dissipation rate. This satisfies the transport equations quoted below at any point in the flow domain. Two transport equations are used: one for the turbulent kinetic energy k and the other for the kinetic energy dissipation rate ε .

Equation for the turbulent kinetic energy k :

$$\frac{\partial(\rho k)}{\partial t} + \frac{\partial(\rho U_i k)}{\partial x_i} = \frac{\partial}{\partial x_j} \left[\left(\mu + \frac{\mu_i}{\sigma_k} \right) \frac{\partial k}{\partial x_j} \right] + 2\mu_i S_{ij} S_{ij} - \rho \varepsilon - Y_M \quad (2.8.5)$$

Dissipation rate equation ε :

$$\frac{\partial(\rho \varepsilon)}{\partial t} + \frac{\partial(\rho U_i \varepsilon)}{\partial x_i} = \frac{\partial}{\partial x_j} \left[\left(\mu + \frac{\mu_i}{\sigma_\varepsilon} \right) \frac{\partial \varepsilon}{\partial x_j} \right] + 2C_{\varepsilon 1} \frac{\varepsilon}{k} \mu_i S_{ij} S_{ij} - C_{\varepsilon 2} \rho \frac{\varepsilon^2}{k} \quad (2.8.6)$$

The coefficients of the models used by default in the ANSYS code are as follows:

Table II.1. Constants of the standard k- ε model. [10] ANSYS CFX 23R2

Constants	C_μ	σ_ε	σ_k	$C_{\varepsilon 1}$	$C_{\varepsilon 2}$
values	0.09	1.03	1.0	1.44	1.92

The **k-ε** model is widely used in engineering. It is indeed robust, economical in computation time and sufficiently accurate and validated for a wide range of turbulent flows. However, it gives poor results for an important category of situations such as unconfined flows, swirling flows and rotating flows.

II.8.2 K-ω standard Model

The standard k- ω model proposed by CFX is based on the model of Wilcox (1998). This model uses two transport equations: one for the turbulent kinetic energy k and the other for the specific dissipation rate ω.

Turbulent kinetic energy equation k.

$$\frac{\partial(\rho k)}{\partial t} + \frac{\partial(\rho U_i k)}{\partial x_i} = \frac{\partial}{\partial x_j} \left[\left(\mu + \frac{\mu_t}{\sigma_k} \right) \frac{\partial k}{\partial x_j} \right] + G_k - Y_k \quad (2.8.7)$$

Equation of specific dissipation rate ω.

$$\frac{\partial(\rho \omega)}{\partial t} + \frac{\partial(\rho U_i \omega)}{\partial x_i} = \frac{\partial}{\partial x_j} \left[\left(\mu + \frac{\mu_t}{\sigma_\omega} \right) \frac{\partial \omega}{\partial x_j} \right] + G_\omega - Y_\omega \quad (2.8.8)$$

In these equations G_k represents the generation of turbulent kinetic energy due to mean velocity gradients.

$$G_k = \mu_t S^2 \quad (2.8.9)$$

$$S = \sqrt{2S_{ij}S_{ij}} \quad (2.8.10)$$

S is the model of the average deformation tensor raten , G_ω the generation of ω, Y_k, Y_ω represent the dissipation of k and ω due to turbulence with :

$$\mu_t = \alpha^* \frac{\rho k}{\omega} \quad \text{et} \quad \omega = \frac{\varepsilon}{k}, \quad G_\omega = \alpha \frac{\omega}{k} G_k$$

$$\alpha = \frac{\alpha_\infty}{\alpha^*} \left(\frac{\alpha_0 + \frac{R_{el}}{R_\omega}}{1 + \frac{R_{el}}{R_\omega}} \right), \quad \alpha^* = \alpha_\infty^* \left(\frac{\alpha_0^* + \frac{R_{el}}{R_k}}{1 + \frac{R_{el}}{R_k}} \right) \quad (2.8.11)$$

$$R_{e_l} = \frac{\rho k}{\mu \omega}, R_k = 6\alpha_0^* = \frac{\beta_i}{3} \quad (2.8.12)$$

For high Reynolds numbers $\alpha^* = \alpha_\infty^* = 1$

The advantage of the k- ω model over the k- ϵ model is that it takes into account the effects due to turbulence in low Reynolds number flows. It can be used for compressible flows and allows parietal transfers to be taken into account. The Wilcox model is applicable to loaded flows, free-surface flows characterized by high shear stresses, jets and flows around an obstacle (wake phenomenon), and the diffusion of a dissolved pollutant.

Table II.2. Constants of the k- ω standard model. [10]

Constants	α_0^*	α_∞	α_0	β_0^*	β_i	R_B	R_k	R_ω	ζ^0	σ_k	σ_ω
values	1	0.52	0.11	0.09	0.072	8	6	2.95	1.5	2.0	2.0

II.8.3 Model k- ω SST (Shear Stress Transport)

This is the model chosen for the present study for both water and the contained phase. Turbulence can be defined as irregularities in the movement of a fluid and is characterized by the formation of vortices of all scales. The movement of fluid particles is random and unpredictable.

A turbulence model is used to predict the effects of turbulence in a flow without solving the problem of turbulent fluctuations on very small scales.

For flows in a centrifugal pump, the turbulence model with SST (Shear Stress Transport) is recommended. This model is robust and can accurately predict the disbands that occur on the walls of the internal components of a turbomachine. The turbulence models are based on the hypothesis of the relationship between the gradients of the mean velocities and the turbulent viscosity given by:

$$\overline{-\rho u_i u_j} = -\mu_t \left(\frac{\partial u_i}{\partial x_j} + \frac{\partial u_j}{\partial x_i} \right) + \left(\frac{2}{3} \mu_t \frac{U_m}{x_m} + \rho k \right) \delta_{ij} \quad (2.8.13)$$

x_j : Generalized coordinates.

U_j : velocity component in the direction of the coordinates.

ρ : Density.

μ_t : Turbulent viscosity.

K : turbulent kinetic energy.

The k-omega model assumes that the turbulent viscosity is related to the turbulent kinetic energy K and the turbulent frequency ω by the following relationship:

$$\mu_t = \rho \frac{k}{\omega} \quad (2.8.14)$$

$$\overline{-\rho u_i u_j} = \mu_t \left(\frac{\partial u_i}{\partial x_j} + \frac{\partial u_j}{\partial x_i} \right) - \frac{2}{3} \rho k \delta_{ij} \quad (2.8.15)$$

$$k = \frac{1}{2} \overline{u_i u_i} \quad (2.8.16)$$

II.8.4 Rotation and Curvature Correction

In order to account for the effects of rotation and curvature (RC) on the flow, the production term P_k in the k and ω equation gets multiplied by the function f_{r1} . This function was developed by Smirnov and Menter (90] and has the following form:

$$f_{r1} = \max \left[\min(f_{rot}, 1.25), 0 \right] \quad (2.8.17)$$

With:

$$f_{rot} = (1 + c_{r1}) \frac{2r^*}{1 + r^*} \left[1 - c_{r3} \tan^{-1} \left(c_{r2} \hat{r} \right) \right] - c_{r1} \quad (2.8.18)$$

The value of f_{r1} is larger than one for concave curvatures which results in enhanced production rate and less than one for convex curvatures leading to decreased production rate in the turbulent equations. Both r^* and \hat{r} depend on the strain rate tensor S_{ij} , the rotation rate tensor W_{ij} , and the angular velocity of the rotating frame of reference ω :

$$r^* = \frac{S}{W} \quad (2.8.19)$$

with the magnitude of the rotation rate tensor

$$W = \sqrt{2W_{ij}W_{ij}} \quad (2.8.20)$$

$$W_{ij} = \frac{1}{2} \left(\frac{\partial u_i}{\partial x_j} - \frac{\partial u_j}{\partial x_i} + 2\varepsilon_{mji}\omega_m \right) \quad (2.8.21)$$

And

$$\hat{r} = \frac{2W_{ik}S_{jk}}{WD^3} \left(\frac{DS_{ij}}{Dt} + (\varepsilon_{imn}S_{jn} + \varepsilon_{jmn}S_{in})\omega_m \right) \quad (2.8.22)$$

with the Levi-Civita symbol ε_{ijk}

$$D^2 = \max(S^2, 0.09\omega^2) \quad (2.8.23)$$

and the Lagrangian derivative of the strain rate tensor $\frac{DS_{ij}}{Dt}$. Note that the equations above are written in Einstein summation convention.

Table II.3. Tableau The constants for the SST RC turbulence model [11].

Constants	c_{r1}	c_{r2}	c_{r3}
Values	1.0	2.0	1.0

II.9. FLOW MODELLING AT THE WALL

Turbulent flows are significantly influenced by the presence of solid walls. In areas very close to the walls, viscosity effects are created, reducing fluctuations in tangential velocities (parallel to the wall). Outside this zone, turbulence appears more rapidly as a result of the production of turbulent kinetic energy due to the mean velocity gradient.

A number of experiments have shown that the near-wall region can be subdivided into two layers: the innermost layer and the viscous sub-layer, known as laminar flow, which are almost identical. Molecular viscosity plays a dominant and important role in heat transfer, further from the wall in the logarithmic layer turbulence dominates the mixing process, however there is a region in the logarithmic layer called the buffer layer where the effects of molecular viscosity and turbulence are of equal importance. The figure below illustrates the subdivisions of the region near the wall.[23]

II.9.1 Wall treatment

The treatment of the wall region is very important for the numerical simulation of turbulent flow. Two approaches are commonly used to model the flow in this region.

The first approach consists of solving the equations of the problem up to the solid wall on which the boundary condition is applied . solid wall to which the boundary condition is applied (known as the near wall).

The other alternative that can be considered is to stop the calculation at a certain distance from the wall and use a wall law to link the calculated region to the wall (called the wall law), in which case the wall law is not used to solve the flow but rather to calculate the appropriate boundary conditions to be applied at the first node.

The law approached in ANSYS CFX is an extension of the method of LAUNDER and Spalding ,in the logarithmic region the tangential velocity near the wall is related to the shear wall τ_ω by means of a logarithmic relationship for the velocity near the wall is given by the following equation :

$$u^+ = \frac{u_t}{u_\tau} = \frac{1}{k} \cdot \ln(y^+) + C \quad (2.9.1)$$

Where:

$$y^+ = \frac{\Delta y u_\tau}{\nu} \quad (2.9.2)$$

And:

$$u_\tau = \sqrt{\frac{\tau_\omega}{\rho}} \quad (2.9.3)$$

With:

u^+ is the velocity close to the wall, u_τ the friction velocity, u_t the known velocity tangent to the wall at a distance of Δy the wall, y^+ the distance from the wall, τ_ω the wall shear stress, k the Von Karman constant and C is a logarithmic constant depending on the roughness of the wall.

In terms of meshes, the two approaches for modelling close to the wall the choice of y^+ . The first approach (close to the wall) consists of solving the equations of the problem down to the interior of the viscous sublayer, in which case it is usual to use a mesh whose first node is very close to the wall, located at $y^+ \approx 1$.

The Spalart-Allmaras, $K-\omega$ And SST turbulence models are thus designed to solve right up to the wall. But the second approach (wall law) the first mesh must be located beyond the buffer sublayer $y^+ \geq 30$. The turbulence model $k-\varepsilon$ uses this method which reduces the number of computational meshes in the boundary layer. [7]

II.9.2 Automatic wall treatment

The problem becomes singular at separation points where the velocity near the wall u_t approaches zero, in the logarithmic region in this case the distance y^+ from the first node tends towards zero, to counter this problem in the ANSYS CFX software uses a velocity scale u^* instead of u^+ as follows:

$$u^* = C_\mu^{1/4} \cdot k^{1/2} \quad (2.9.4)$$

This scale has the useful property that it does not go to zero if u_t goes to zero, in the knowledge that the kinetic energy k is never completely at zero in a turbulent flow.

The following explicit equation for u_τ can be obtained:

$$u_\tau = \frac{u_t}{\frac{1}{k} \cdot \ln(y^*) + C} \quad (2.9.5)$$

The absolute value of the shear stress

$$\tau_w = \rho \cdot u_t \cdot u^* \quad (2.9.6)$$

$$y^* = \frac{(\rho \cdot u^* \cdot \Delta y)}{\mu} \quad (2.9.7)$$

In ANSYS CFX, for the treatment of the region near the wall, two methods can be easily used 'Scalable Wall Function' and 'Automatic Wall treatment'.

The first Scalable Wall Function method applies when a wall law is used, for example with the K turbulence model $k - \varepsilon$.

The basic idea of a scalable wall function is to limit the minimum value of y^* used in the logarithmic law, such that :

$$y^* = \max(y^+, 11.06) \quad (2.9.8)$$

The value of $y^* = 11.06$ is located at the intersection between the logarithmic law and the linear velocity profile of the viscous sublayer.

The calculation is therefore not allowed to go below this limit ($y^* = 11.06$), so all the points in the mesh are outside the viscous sublayer.

As for the second method, automatic wall treatment, it makes it possible to move on to a resolution down to the wall using a wall law within the same calculation, for example in the case where the $k - \omega$ and SST turbulence models are used.

In this method, the mesh used at the wall is very fine, since there is an analytical relationship for ω in the viscous sublayer given by the following formula:

$$\omega = \omega_s \cdot \sqrt{1 + \left(\frac{\omega_l}{\omega_s}\right)^2} \quad (2.9.9)$$

Where :

The analytical expression in the logarithmic region is given by the following equation:

$$\omega_l = \frac{u^*}{a_1 \cdot k \cdot y} \quad (2.9.10)$$

The corresponding analytical expression in the sublayer is given by the following equation:

$$\omega_s = \frac{6 \cdot \nu}{\beta \cdot (\Delta y)^2} \quad (2.9.11)$$

Δy : Being the distance between the first and second mesh.

II.10. BOUNDARY CONDITION

There are several types of conditions proposed for imposing boundary conditions

in CFX :

inlet pressure condition: using this condition, the inlet pressure is known and the corresponding flow velocity and the total pressure imposed for a compressible flow are found using the following relationship:

- Total inlet pressure

$$P_t = P_s \cdot \left(1 + \frac{\gamma - 1}{2} \cdot M^2 \right)^{\frac{\gamma}{\gamma - 1}} \quad (2.10.1)$$

- Total inlet temperature

$$T_t = T_s \cdot \left(1 + \frac{\gamma - 1}{2} \cdot M^2 \right) \quad (2.10.2)$$

- The choice of turbulence model (*SA* , *k - ε* , *k - ω* , *k - ω SST* , *k - ω SST (CC)*).
- Rotational speed N
- Pressure static (variable) condition at the outlet.

II.10.1 Wall condition

This boundary condition is used to specify the walls of the control volume. Either the part in relative motion (centrifugal compressor impeller) or the fixed part (diffuser) For viscous flows, the non-slip condition is associated with this boundary condition.

II.10.2 Periodicity condition

The periodicity condition is used when the calculation domain has a regular geometric distribution of fluid sub-domains (see(2.10.1)):

This condition makes it possible to reduce the number of mesh elements and therefore the calculation time.

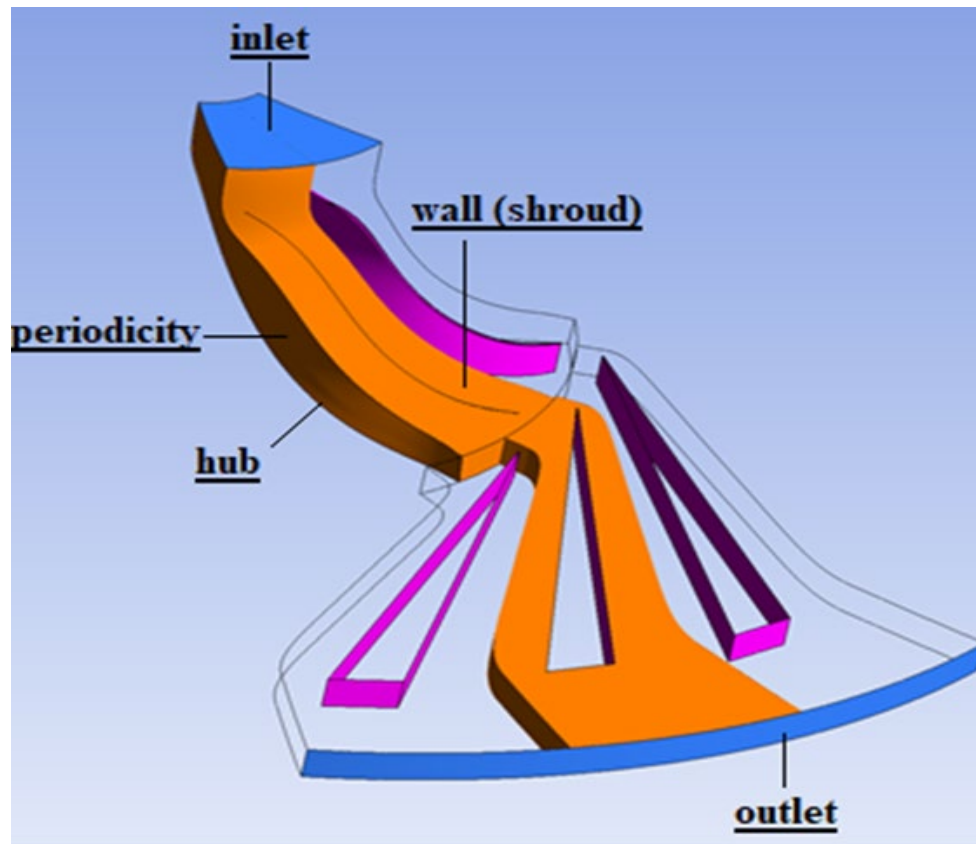


Figure II.10.1. Computational domain of the Radiver centrifugal compressor.

CHAPTER III: SIMULATION

III.1. INTRODUCTION

Computational fluid dynamics (CFD) is concerned with numerical solution of differential equations governing transport of mass, momentum, and energy in moving fluids. It is the process of mathematically predicting physical fluid flow by solving the governing equations using computational power. [24]

When an engineer designs a new product, such as a compressor, aerodynamics plays a crucial role in the overall performance of the design. However, aerodynamic performance is not easily quantifiable during the concept phase. Traditionally, the only way for an engineer to optimize their design is to conduct physical tests on product prototypes.

With the rise of computers and ever-growing computational power, the field of CFD has become a commonly applied tool for predicting real-world physics. In a CFD software analysis, fluid flow and its associated physical properties, such as velocity, pressure, viscosity, density, and temperature, are calculated based on defined operating conditions.

Every CFD tool, both commercial and/or open source, uses a mathematical model and numerical method to predict the desired flow physics¹. The most common CFD tools are based on the Navier-Stokes (N-S) equations¹. While the bulk of the terms in the Navier-Stokes equations remains constant, more terms can be added or removed based on the physics.

It is very important that the proper operating conditions, numerical methods, and physics are considered in order to conduct an accurate and successful CFD analysis. [24]

Equations of CFD

The main structure of thermo-fluids examination is directed by governing equations that are based on the conservation law of fluid's physical properties. The basic equations are the three laws of conservation:

1. Conservation of Mass: Continuity Equation
2. Conservation of Momentum: Newton's Second Law
3. Conservation of Energy: First Law of Thermodynamics or Energy Equation

These principles state that mass, momentum, and energy are stable constants within a closed system. In short, everything must be conserved. [25]

The investigation of fluid flow with thermal changes relies on certain physical properties. The three unknowns which must be obtained simultaneously from these three basic conservation equations are the velocity \vec{v} , pressure p and temperature T . Yet p and T are considered the two required independent thermodynamic variables.

The final form of the conservation equations also contains four other thermodynamic variables; density ρ , enthalpy h , viscosity μ , and thermal conductivity k ; the last two of which are also transport properties. These four properties are uniquely determined by the value of p and T .

Fluid flow should be analyzed to know \vec{v} , p and T throughout every point of the flow regime. Furthermore, the method of fluid flow observation based on kinematic properties is a fundamental issue. The movement of fluid can be investigated with either Lagrangian or Eulerian methods. [25]

- Lagrangian description of fluid motion is based on the theory to follow a fluid particle that is large enough to detect properties. Initial coordinates at time T_0 and coordinates of the same particle at time T_1 have to be examined. To follow millions of separate particles through the path is almost impossible.
- In the Eulerian method, instead of following any specific particle across the path, the velocity field is examined as a function of space and time.

Partial Differential Equations (PDEs)

The Mathematical model merely gives us interrelation between the transport parameters which are involved in the whole process, either directly or indirectly. Even though every single term in those equations has a relative effect on the physical phenomenon, changes in parameters should be considered simultaneously through the numerical solution, which comprises differential equations, vector-, and tensor notations.

The numerical solution is a discretization-based method used to obtain approximate solutions to complex problems that cannot be solved with analytic methods. As seen in Figure 1, solution processes without discretization merely give you an analytic solution which is exact but simple.

Moreover, the accuracy of the numerical solution highly depends on the quality of the discretization. Broadly used discretization methods might be specified, such as finite difference, finite volume, finite element, spectral (element) methods and boundary element. [26]

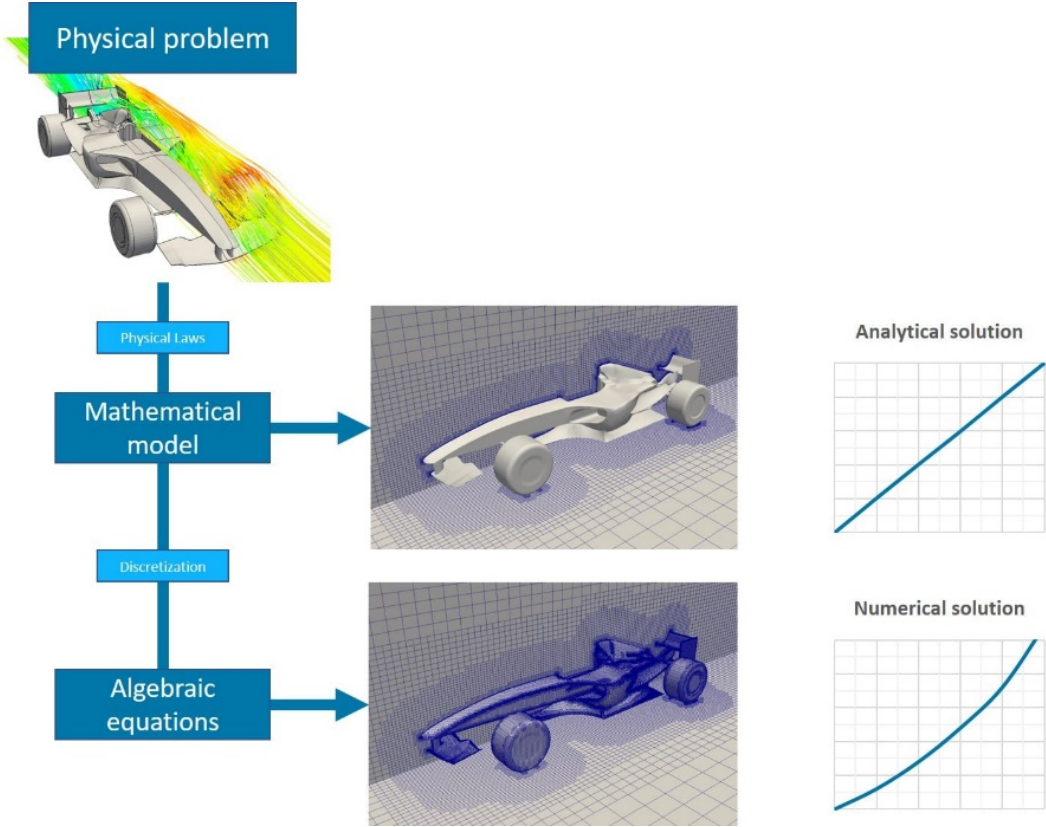


Figure III.1.1. Accurate numerical discretization helps linearize the Partial Differential Equations and capture the sensitive variable gradients.

Computational fluid dynamics (CFD) tools vary in accordance with the mathematical models, numerical methods, computational equipment, and post-processing tools used alongside them. For example, a single physical phenomenon could be modeled with two completely different mathematical approaches, numerical methods, and computational hardware.

That said, over the past decade, several codes/methods have become more common due to their robustness, simulations were carried out using the CFD code **ANSYS CFX 23R2**. Recognized for its outstanding accuracy and speed with turbomachinery applications. It offers streamlined turbo setups, blade design tool integration, and multi-stage CFD modeling.

III.2. INITIAL DATA FOR CREATING A NUMERICAL MODEL OF THE WORKING PROCESS OF A CENTRIFUGAL COMPRESSOR

The initial data for conducting a numerical study of a centrifugal compressor consists of several groups of parameters.

1. Parameters necessary for profiling the blades of the impeller and vane diffuser. This group includes: the number of blades, inlet and outlet constructive blade angles in several sections by height, geometry of the meridional section of the flow part (diameters, blade heights, rim width).
2. Parameters set when configuring the computational model of the compressor: the number of rotor revolutions, flow parameters at the inlet and outlet boundary. All necessary initial data are obtained as a result of the design calculation of the compressor and the thermodynamic calculation of the installation, which it is part of.

III.3. CONSTRUCTION OF A COMPUTATIONAL MODEL OF THE WORKING PROCESS OF A CENTRIFUGAL COMPRESSOR

Step 1. Launching the Ansys Workbench 23R2 program and creating a project, The Ansys Workbench program is designed for the integration of various Ansys company programs.

Intended for solving engineering and research tasks in different areas, as well as for organizing a simple and effective exchange of information between them.

The Workbench software shell is usually launched from the “*Start*” menu of the “Windows” OS:

Start → *Programs* → *Ansys23R2* → *Workbench23R2*

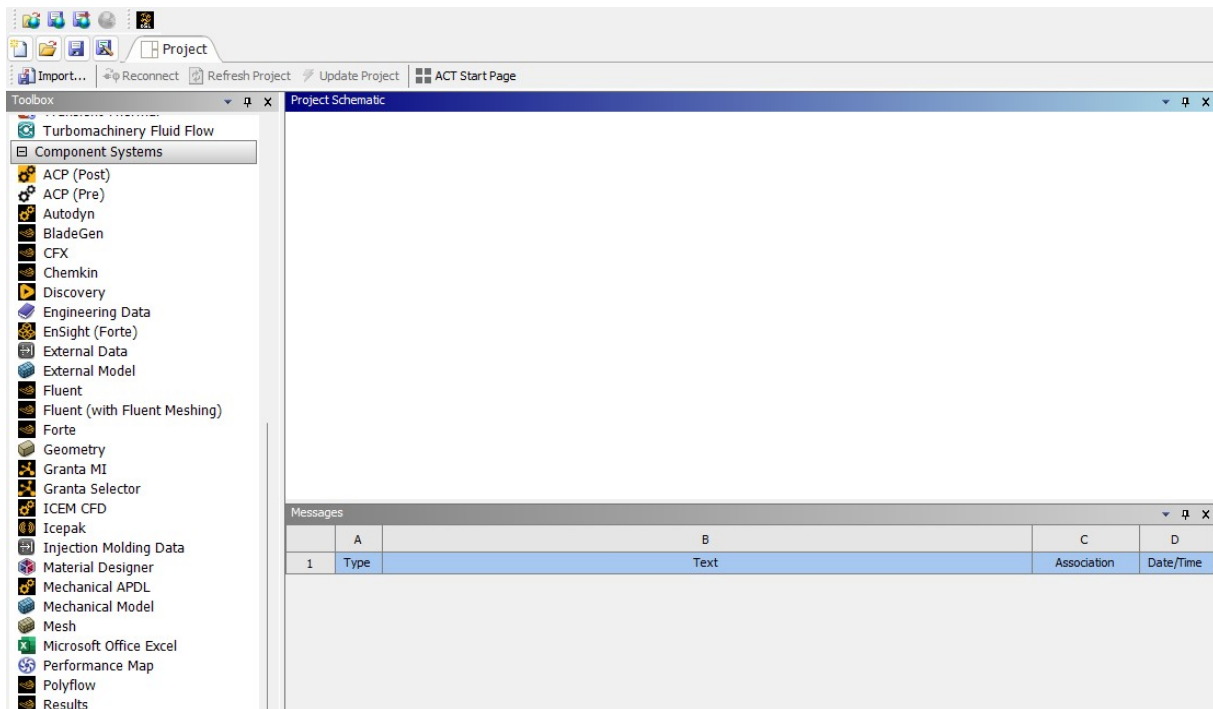


Figure III.3.1. Ansys Workbench program window.

As can be seen from the **Figure III.3.1**, the working window of the Ansys Workbench shell consists of three main parts:

- Main menu;
- Tool window;
- Window for constructing structural diagrams of computational tasks.

Work with project files (reading, saving, importing), setting the appearance of the Workbench shell window, and choosing the dimension in which the computational model will be created are all done in the main menu.

The basis of the Workbench shell working window is the window for constructing structural diagrams of computational tasks.

Working in Workbench is extremely simple and boils down to creating mnemonic diagrams in the area of constructing structural diagrams of computational tasks, reflecting data interactions between programs included in *Ansys 23R2*.

The programs are denoted by blocks, and they are divided into thematic sub-blocks. For example, solving a computational fluid dynamics (CFD) problem in the Fluent or CFX program is divided into sub-blocks corresponding to the stages that need to be solved each time when using this program. For example: geometry construction (Geometry), computational grid creation (Mesh), solver setup (Setup), solution (Solution), and post-processing (Results).

By establishing connections between blocks and sub-blocks, it is easy to describe the solution of complex interdisciplinary problems, or to involve various specialized programs in the creation of the model.

In this window, programs that will be used to solve the set task are placed, and the connections and information flows between them are shown. An example of a mnemonic diagram is shown in **Figure III.3.2**.

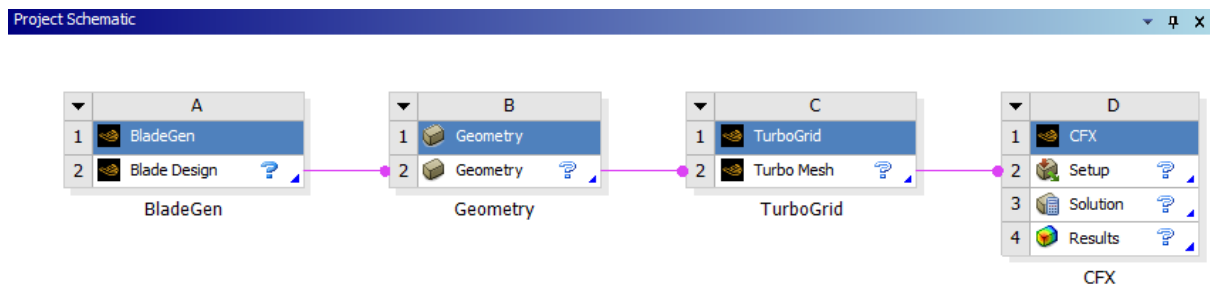


Figure III.3.2. Mnemonic diagram in Ansys Workbench.

Step 2. Creating a meridional profile of the impeller in *BladeGen*, the Ansys Workbench software suite includes the *BladeGen* program, which allows you to profile blade machines of different types based on the results of design calculations.

Before starting to create the geometry, you need to add the program you plan to work with - *BladeGen* - to the structural diagram construction area of Ansys Workbench.

To do this, you need to find it in the toolbox , click on the corresponding item with the left mouse button (LMB), and without releasing the mouse button, drag the element to one of the green rectangles that will appear in the structural diagram construction area. As soon as the mouse reaches one of the rectangles, its border will turn red. If you release the mouse button at this point, a block of the selected *BladeGen* program will appear in this rectangle.

With the block, you can launch the profiling program by double-clicking on the Blade Design menu with the LMB. As a result, the program window will appear.

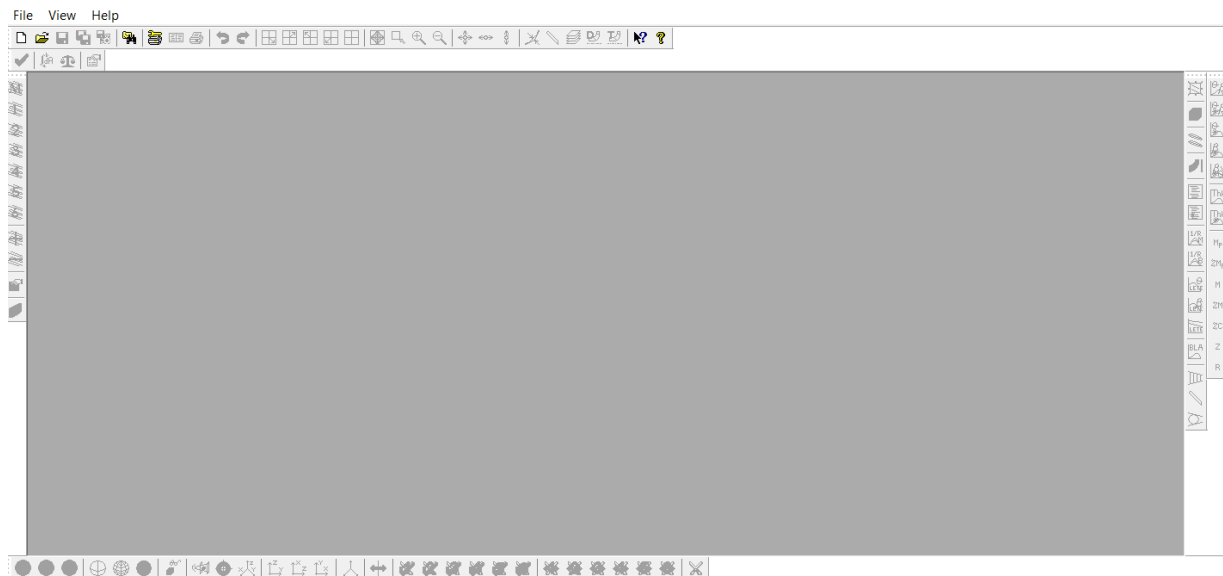


Figure III.3.3. *BladeGen* program window.

To profile the impeller of a centrifugal compressor in this window, you need to press the New button (creating a new project). As a result, a menu will appear, in which you need to specify the type of turbomachine whose blades the user wants to profile. To create an impeller for a centrifugal compressor, you should select the Radial Impeller item.

In the opened template for describing the geometry of the meridional section of the designed turbomachine, you should enter the main dimensions that define the geometry of the inlet and outlet sections of the blade row: radii and axial coordinates. Their numerical values are assigned based on the results of the design calculation of the compressor.

The correctness of the entered values is confirmed by pressing the “OK” button in the upper right corner of the menu. After that, the program will automatically switch to the template with which the main parameters of the blade profile are entered. Here you should enter the desired profile thickness and angular extent of the blade. Also in this template, in the # Blades field, you should enter the number of impeller blades.

The correctness of the entered values is confirmed by pressing the “OK” button in the upper right corner of the menu. Then you should also set the angular extent of the blade and its maximum thickness.

Step 3. Correcting the impeller geometry in accordance with the results of the design calculation, the blade shape of the impeller obtained in the previous step was generated automatically and is approximate. Therefore, at the next stage, it is necessary to correct the

blade geometry so that it corresponds to the results of the design calculation and the user's wishes. It is necessary to correct the shape of the meridional outline, the blade angles at the inlet and outlet, as well as the thickness of the profiles in the control sections, and if necessary, add splitters.

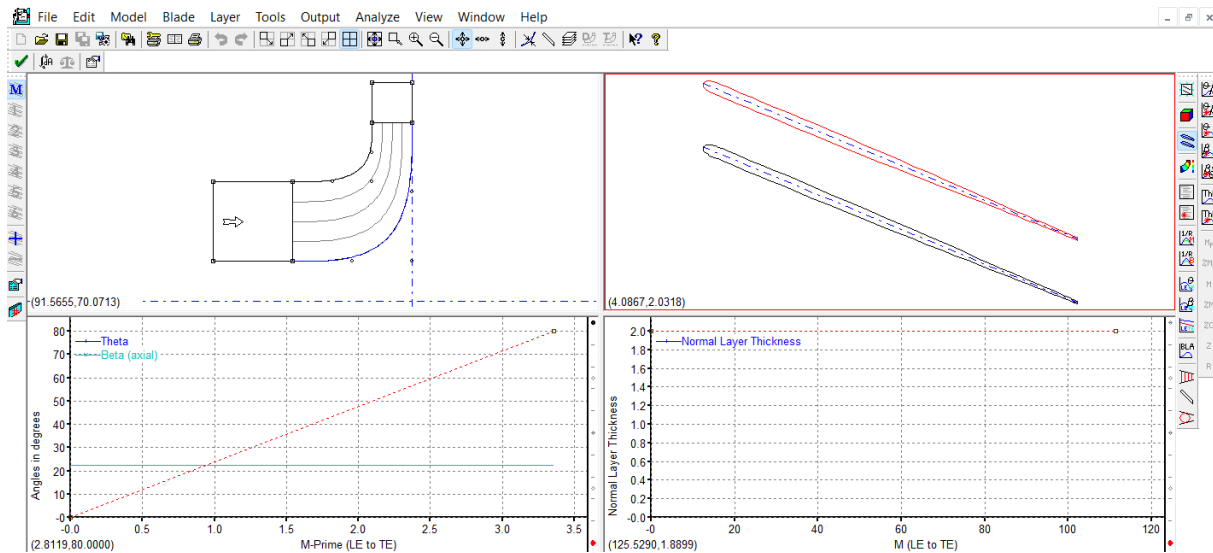


Figure III.3.4. Geometry of the impeller obtained in the first approximation.

Any control point of the meridional section of the impeller can be corrected if necessary. To do this, you should click the left mouse button (LMB) on the required point.

This point will be highlighted in red. If, without releasing the mouse button, you start moving it, the point will move according to the mouse movement. Obviously, it is difficult to achieve their exact position by moving points manually.

Therefore, you should click the LMB on the point for the second time. After this action, a menu with the coordinates of the selected point will appear. In it, you should enter the desired coordinate values.

In particular, when creating a computational model of a compressor, it is necessary to correct the position of the left and right points of the outlet boundary, since it is along it that docking with the outlet domain will be carried out.

The sizes of the two areas must match. For this, first, you need to click on the left point. In the menu that appears, you need to enter the required coordinates of the edited point, for example, radial (Vertical). The settings made should be confirmed by pressing the OK button.

Similarly, you should change the radial coordinate of the right point of the outlet boundary. Also, if desired, in the axial direction, you can shift the inlet boundary, increasing or decreasing the length of the inlet section.

Step 4. Correcting the shape of the meridional outlines the shape of the meridional section of the impeller of the centrifugal compressor, built in automatic mode, is far from perfect. Therefore, it should be corrected.

The shape of the meridional outline can be described in two ways: by a spline and by a Bezier curve. In both cases, it is necessary to set the positions of the control points that determine the geometry of the curve.

In the first case, these points lie directly on the curve, in the second case, the positions of the nodal points of the Bezier curve are set, which do not lie on the line. The number of points describing curves can be any, but it is usually convenient to use 4...5. Control point coordinates can be specified “manually” using the mouse, or directly entered from the keyboard. Obviously, the second method is more accurate, but for describing the shape of meridional outlines, the first method is more visual and effective.

The shape of the meridional outlines is conveniently described by setting the positions of the spline points lying directly on it. To do this, at the first stage, you need to select the outline, the shape of which the user wants to correct, with a single click of the LMB. Then you need to right-click (RMB) on the same curve. As a result, a menu will appear. In it, you should select the following commands:

Convert Points To → Splane Curve Point.

After that, a menu will appear in which you need to select the number of points that describe the shape of the spline. Four points will be enough for a quality description¹². After executing the command, the selected number of points (including the ends) will appear on the highlighted curve, A similar action should be performed with the second outline.

Then, by moving the points of both (hub and peripheral sections) with the mouse, you need to get such a shape of the meridional section that provides a smooth change in the area of the inter-blade channel. To do this, you need to select one of the points with a click of the LMB and, without releasing the mouse button, move it to the required position.

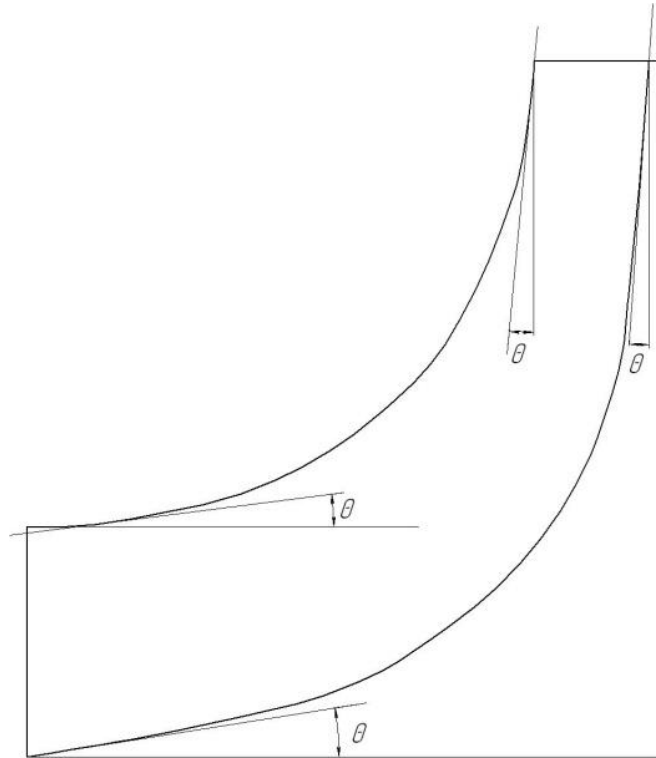


Figure III.3.5. Angles of inclination of the walls of the meridional bypass. [27]

A criterion for the quality of the obtained meridional section can be the graph of the change in the cross-sectional area of the compressor along the length of the flow part. To display it in one of the BladeGen program windows, you need to press the ***Quasi – Orthogonal Area Graph*** button in the left vertical menu. The area of the passage section should decrease smoothly without sharp jumps. When defining the shape of the meridional section.

Import the Geometric Model: In *DesignModeler*, to create and modify the geometry as needed.

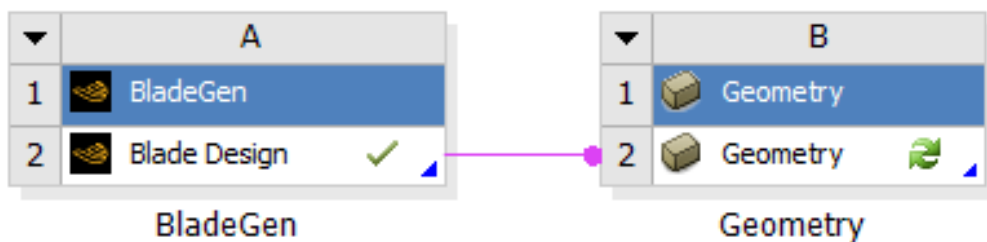


Figure III.3.6. Connected blocks of BladeGen and Geometry programs.

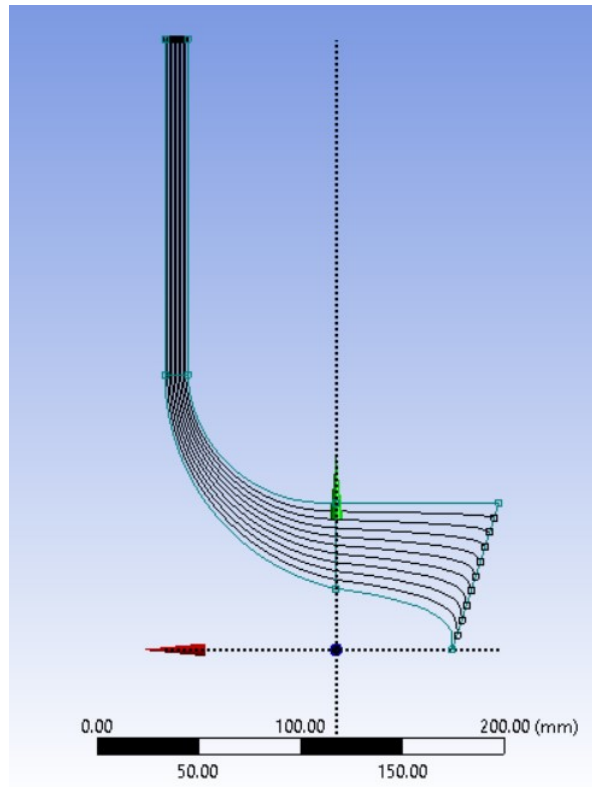


Figure III.3.7. Geometry of the impeller in *DesignModeler*.

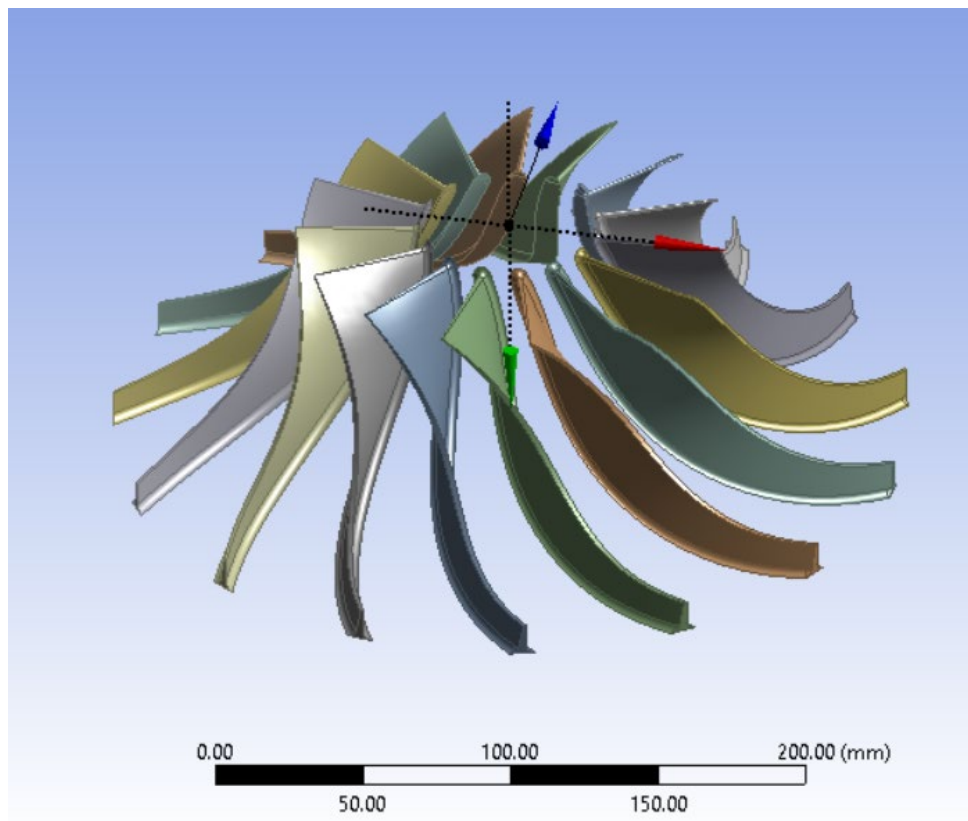


Figure III.3.8. 3D model of the impeller blades obtained in *DesignModeler*.

Step 5. Transfer of the created blade rim geometry to the TurboGrid program for building a finite element mesh at this stage, there is a fully described geometry of the impeller of the centrifugal compressor in the Geometry program. Based on it, it is necessary to create a computational model of the flow in the impeller and divide it with a structural finite element mesh. These actions are conveniently carried out in the TurboGrid program.

The creation of a finite element flow model in the impeller of the centrifugal compressor takes place under the control of the Ansys Workbench software shell. Its use allows you to fully automate the process of transferring information about the geometry of the blades from Geometry to TurboGrid.

After that, you need to launch the TurboGrid program by double-clicking on the Turbo Mesh item. In the opened program window, the blades of the impeller of the centrifugal compressor, created in BladeGen, will be automatically loaded, and based on them, the geometry of the computational domain will be formed.

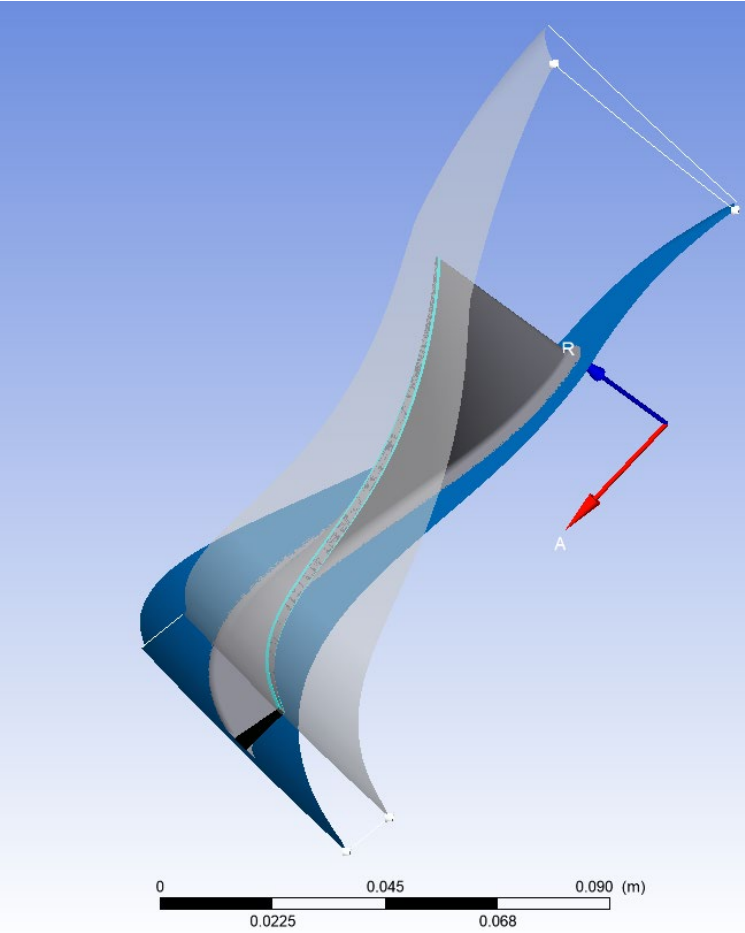


Figure III.3.9. TurboGrid program window with the loaded geometry of the impeller.

Step 6. Setting the radial gap size, the working blades of turbines without a band shelf have a radial gap between the upper end and the casing, which has a significant impact on the working process in the stage. Therefore, when modeling gas-dynamic processes in a turbomachine, it must be taken into account.

To describe the presence of a radial gap and its size in the TurboGrid program, you need to double-click the left mouse button on the Shroud Tip item (gap on the periphery), located in the Blade Set element in the object tree.



Figure III.3.10. Specifying the Radial Gap.

Step 7. Enabling automatic mesh update, this step must be performed, without it further mesh construction is impossible.

After each operation, TurboGrid automatically rebuilds the computational model, as well as the topology and mesh associated with it (if they were previously described).

This process takes a long time and interferes with working with the model when editing the created model. Therefore, by default, automatic rebuilding of the model after each operation is disabled.

At the same time, the options for building topology and mesh become unavailable. For this reason, before proceeding to mesh construction, automatic rebuilding of the computational model should be enabled.

To do this, you need to right-click on the Topology Set element, located in the project tree, and in the appeared pop-up menu, uncheck Suspend Object Updates (suppress object updates).

As a result, the Topology Set element will become bright (active), the inscription Suspended (suppressed) will disappear next to it, and the topology of the mesh will be built according to the settings available in the program by default. This process takes some time.

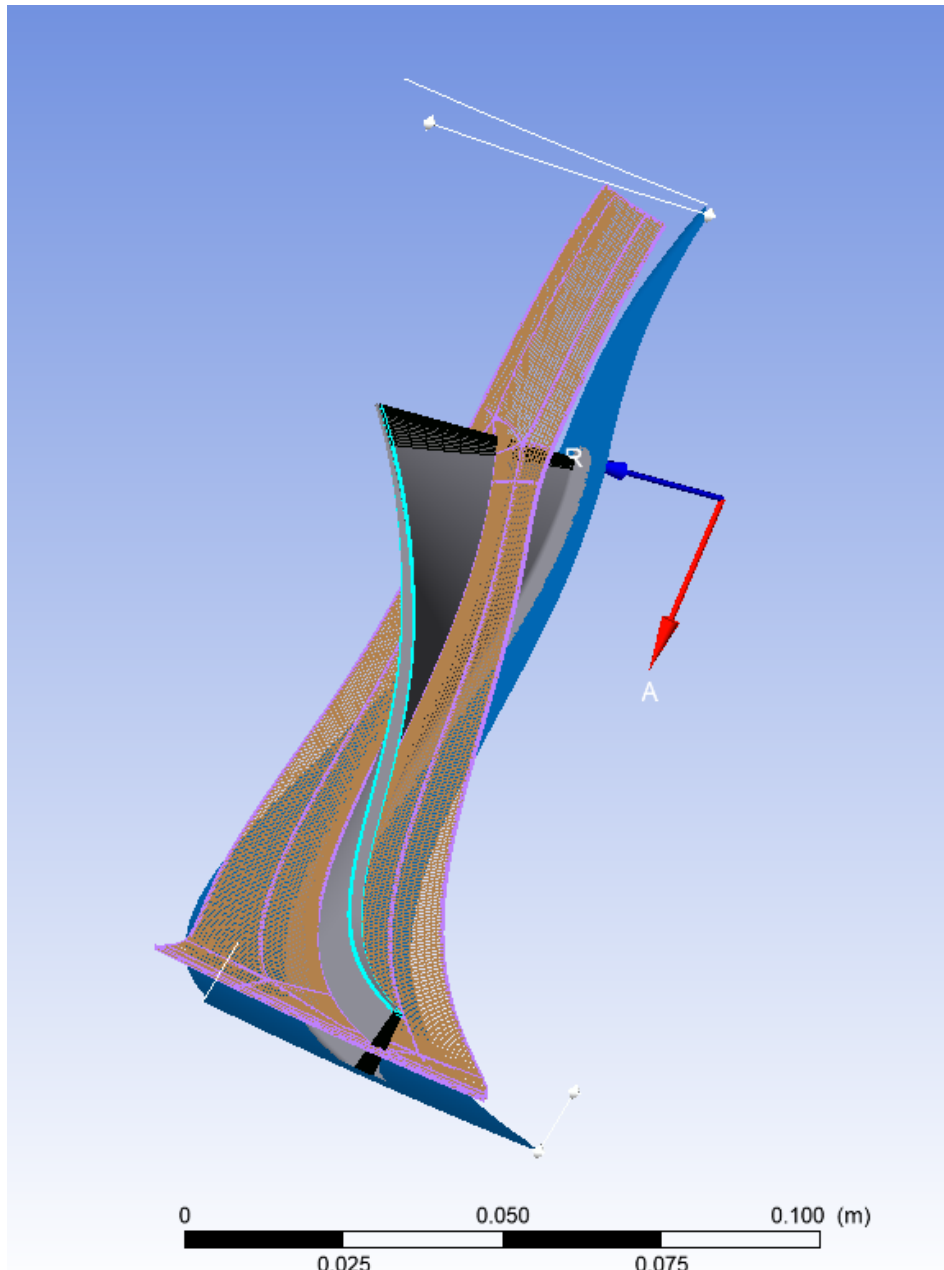


Figure III.3.11. Enable automatic grid updates.

Step 8. Description of mesh topology, when overlaying a finite element mesh on computational areas of complex geometry, for example, turbomachines, often the only way to get a high-quality orthogonal mesh is to use a block structure. The essence of this approach lies in dividing the geometry of the computational area into blocks, each of which can be guaranteed to be divided by a high-quality mesh.

This approach is implemented in the TurboGrid program in a fully automatic mode. Moreover, its use in most cases allows you to get a high-quality finite element mesh in the inter-blade channel without intervention and corrections from the user.

To perform the topology construction in automatic mode, you need to double-click the left mouse button in the object tree on the Topology Set item. In the appeared menu, in the *Topology Definition* → *Placement* list, you should select the *ATM Optimized* item and confirm the selection by pressing the *Apply* button.

Step 9. Setting the number of mesh elements, the number of finite elements and mesh density are important indicators that determine the accuracy of the calculation. The mesh density, especially in areas of high velocity gradients, for example, in boundary layers, should be sufficient for a high-quality description of the effects occurring there.

Setting the mesh density in the TurboGrid program is done in the Mesh Data menu, which can be called by clicking the left mouse button in the corresponding place of the object tree.

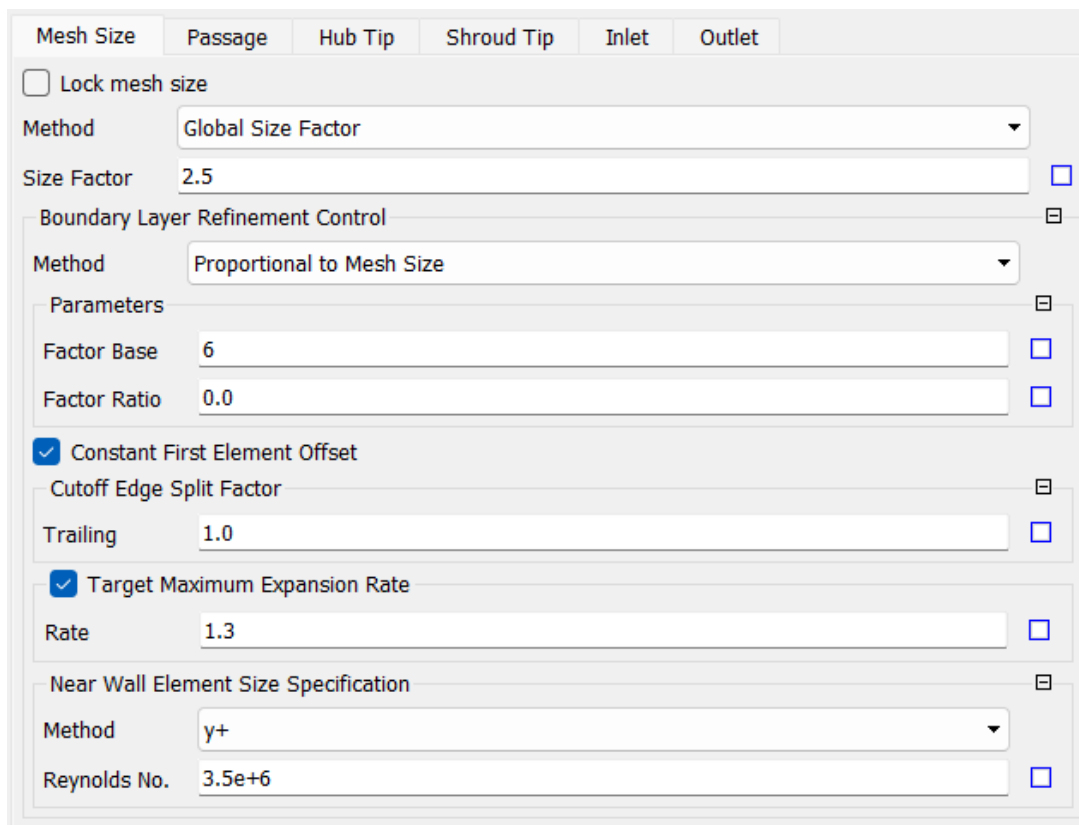


Figure III.3.12. Setting the density of the finite element mesh.

In this menu, in the Mesh Size tab, in the Method field, the method of setting the mesh density is selected. In this field, from the drop-down list, you should select the Global Size Factor item.

Also, the quality of the mesh at the blade walls should be described. To do this, in the Method field of the Near Wall Element Size Specification section, you should select the y+

item, and below enters the Reynolds number value characteristic for this impeller **Figure III.3.12.**

After completing the assignment of all fields, you need to confirm all the selected settings with the *Apply* button.

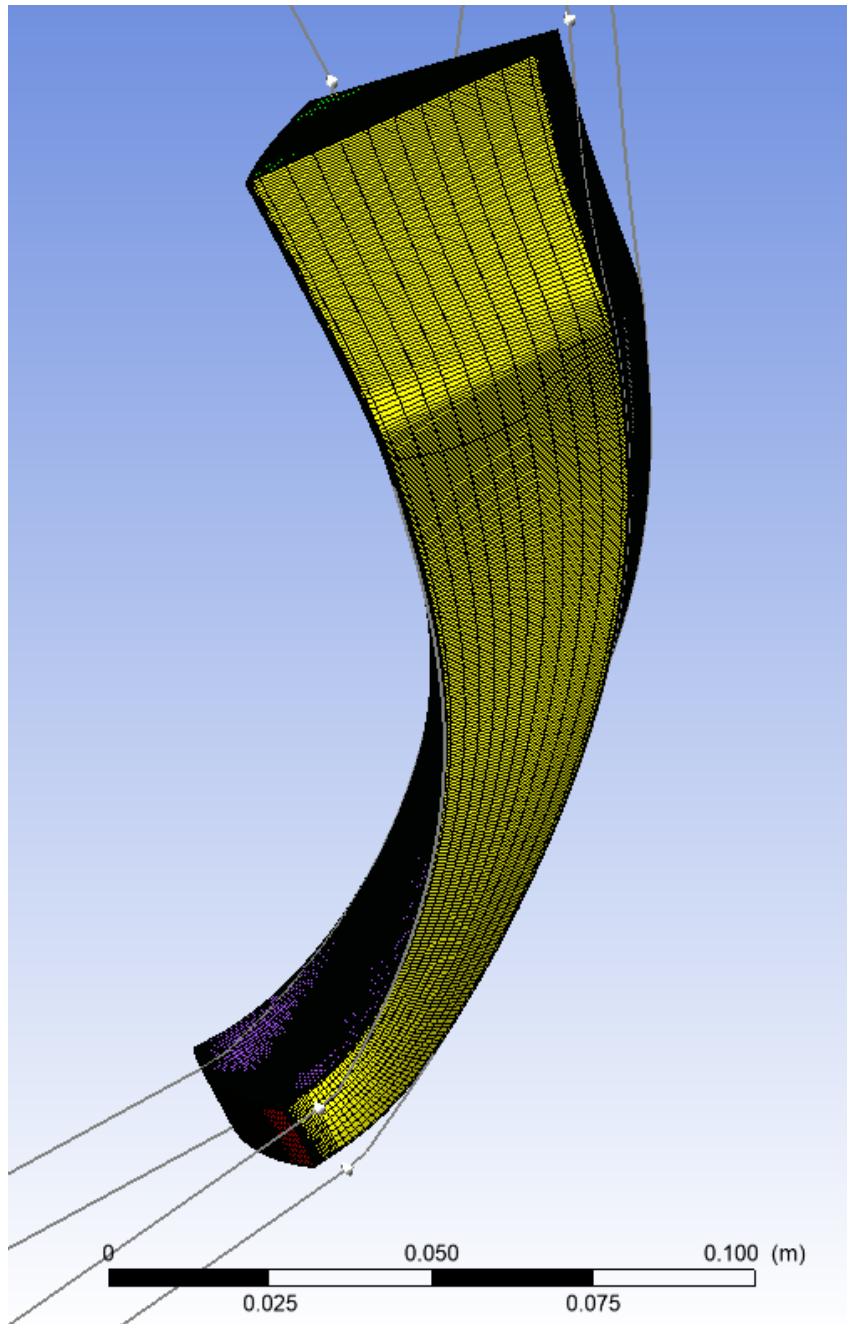


Figure III.3.13. 3D model of the impeller Mesh.

Step 10. Building a finite element mesh Now that the topology has been fully defined and the number of finite elements has been selected, you can generate a mesh by pressing the

Mesh button in the main menu of the TurboGrid program. Generation of a finite element mesh at this point, a three-dimensional mesh of the specified density will be created, and the mesh quality analysis (Mesh Analysis) in the project tree will become active **Figure III.3.14**.



3D Mesh	
Node Counts	
All domains:	1605540
Passage:	1605540

Figure III.3.14. Viewing information about the sect of finite elements.

Step 11. Mesh quality analysis After building the mesh, it is necessary to evaluate the quality of the mesh. It is performed using the following criteria:

- Maximum (Minimum) Face Angle - the maximum (minimum) angle between the edges of all cells that converge at a node, a measure of mesh skewness, for an absolutely orthogonal mesh it is 90 degrees.
- Maximum Element Volume Ratio - the ratio of the volumes of the maximum and minimum cells touching the node.
- Minimum Volume - the minimum volume of a cell, should have a non-negative value.
- Maximum Edge Length Ratio - the ratio of the lengths of the largest and smallest edges of the cells touching the node.
- Maximum Connectivity Number - the maximum number of cell connections.

For all parameters, recommended ranges of values are set. If it falls within the required range, the mesh is suitable for solving the problem. If one of the parameters has a value that goes beyond the default recommended ranges, the calculation error increases and there is a likelihood of solver failure.

To assess the quality of the constructed mesh in TurboGrid, use the Mesh Analysis command. You can access it by double-clicking the corresponding item in the project tree.

Mesh quality parameters that fall outside the recommended ranges in the Mesh Analysis menu are highlighted in red and marked with an exclamation mark.

Clicking on any of them will display cells in the visualization window where the selected quality criterion values exceed the recommended limits **Figure III.3.15**.

Mesh quality criteria are ranked by importance as follows (in descending order of importance):

- Minimum volume – should always be non-negative;
- Maximum/minimum cell angle – maximum value – 165, minimum – 15. However, going beyond these limits is acceptable.
- Ratio of edge lengths – exceeding 100 units is permissible;
- Ratio of volumes of elements with one node – this requirement is not mandatory;
- Number of connections – this requirement is not mandatory.









Domain		ALL			
	Mesh Measure	Value	% Bad	% ok	% OK
	Orthogonality Angle	30.6644 [degree]	0.0000	3.1053	96.8947
	Minimum Face Angle	29.4418 [degree]	0.0000	0.0000	100.0000
	Maximum Face Angle	157.791 [degree]	0.0000	0.0000	100.0000
	Edge Length Ratio	10095.1	5.7261	2.0951	92.1788
	Element Volume Ratio	11.7339	0.0000	1.0669	98.9331
	Minimum Volume	1.00984e-16 [m^3]	0.0000	0.0000	100.0000
	Connectivity Number	10	0.0000	0.0085	99.9915
	Skewness	0.75323	0.0000	0.0040	99.9960

Figure III.3.15. The value of the selected quality parameter.

The criteria Maximum Element Volume Ratio and Maximum Edge Length Ratio are not critical, and if they exceed the recommended values, it can be overlooked.

If the values of other mesh quality criteria exceed the recommended values, then a topology correction is required. However, when using the ATM Optimized topology, an acceptable mesh quality is almost always achieved.

After checking the mesh quality, the Mesh Statistics menu can be closed by clicking the Close button.

Step 12. Saving the created mesh model of the turbine blade row to save the created finite element model of the turbine blade row, press the *Save Mesh* button in the main menu of TurboGrid. In the window that appears, specify the file name – ‘Rotor’ and click the *Save button*. This creates a file for Ansys CFX with the extension *.gtm – (Rotor.gtm) in the working folder.

III.4. CONSTRUCTION OF THE COMPUTATIONAL MODEL OF THE WORKING PROCESS OF THE BLADE DIFFUSER

Step 1. Description of the blade diffuser geometry in the first approximation, it is also advisable to create a computational model of the flow in the blade diffuser in the Ansys Workbench environment using the BladeGen and TurboGrid programs, similar to how it was done when creating the impeller model.

For this, in the Ansys Workbench program’s schematic creation window, you need to create a new BladeGen block (separate from the impeller) and launch this program. This process is no different from the one described in section 2.

To create a new blade diffuser profiling project in the BladeGen window, you need to press the new button (*creating a new project*). As a result, a menu will appear where you need to select the type of turbine blade that the user wants to profile. For the blade diffuser - Radial Diffuser.

In the opened template for describing the geometry of the meridional section of the designed blade row, you should enter the main dimensions that describe the inlet and outlet sections.

Their numerical values are taken from the results of the design gas-dynamic calculation of the stage. The correctness of the entered values is confirmed by pressing the “OK” button in the upper right corner of the menu.

After that, the program will automatically go to the template where the main parameters of the blade profile are entered. Here you should enter the desired profile thickness and angular extent of the blade.

The correctness of the entered values is confirmed by pressing the “OK” button in the upper right corner of the menu. After that, the program will generate the blade geometry in the first approximation **Figure III.4.1**.

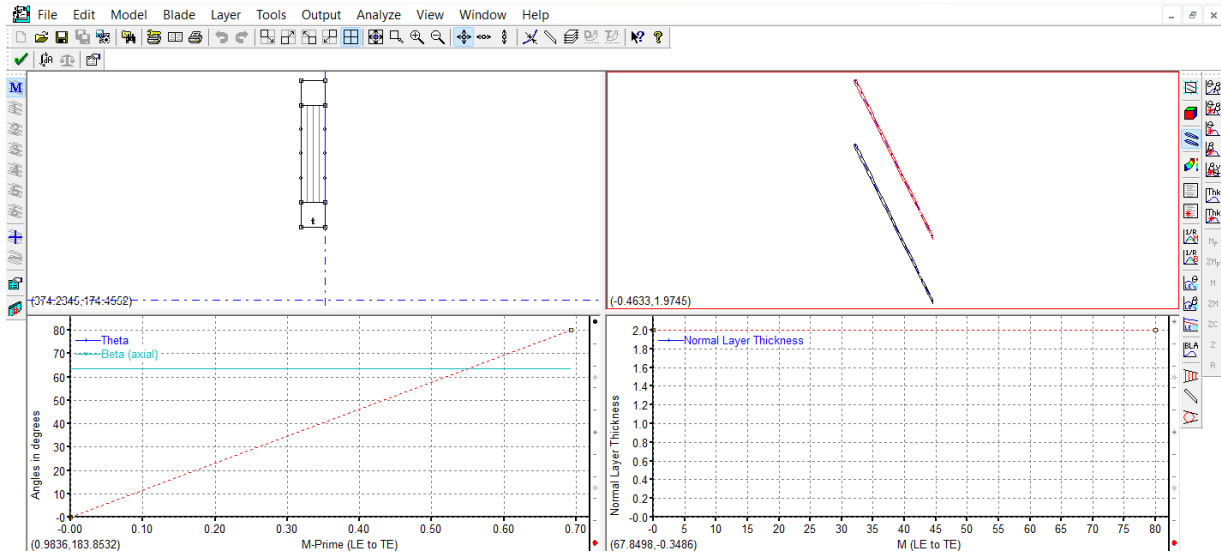


Figure III.4.1. Blade diffuser geometry obtained automatically in the first approximation.

Step 2. Adjustment of blade geometry in accordance with the results of the design calculation.

The blade shape of the diffuser obtained at the previous stage was generated automatically and is approximate. Therefore, at the next stage, it is necessary to adjust the blade geometry in such a way that it corresponds to the results of the design calculation and the user’s desire. It is necessary to correct the shape of the meridional contour, the values of the blade angles at the inlet and outlet, as well as the thickness of the profiles in the control sections, and add splitters (if any).

The meridional contours of the diffuser obtained at the previous stage are described by a Bezier curve, however, they need to be corrected: transform the curve into an arc and two straight lines. To do this, you need to split the spline at the reference points, using the Split Segment at Point operation.

After splitting the spline, it will be possible to change the position of the reference points of the meridional section. Any control point of the meridional section of the blade diffuser can be corrected if necessary.

To do this, you need to click the left mouse button on the required point. This point will be highlighted in red.

If, without releasing the mouse button, you start to move it, the point will move according to the user's desire. Obviously, it is difficult to achieve the exact position of the moving point in this way. Therefore, you should click the left mouse button on the point for the second time. After this action, the Point Location Dialog menu will appear with the coordinates of the selected point. In it, you should enter the desired coordinate values.

Step 3. Changing the shape of the blade profile's trailing edge, in automatic mode, the BladeGen program created blades with a rounded leading edge and a cut-off trailing edge. To describe that the trailing edge should also be rounded, you need to press a button in the left side menu. In the appeared Blade Property Dialog menu, select the LE/TE Ellipse tab. There, the type of description of the trailing edge TE Type is changed from cut-off (Cut-off) to rounded (Ellipse).

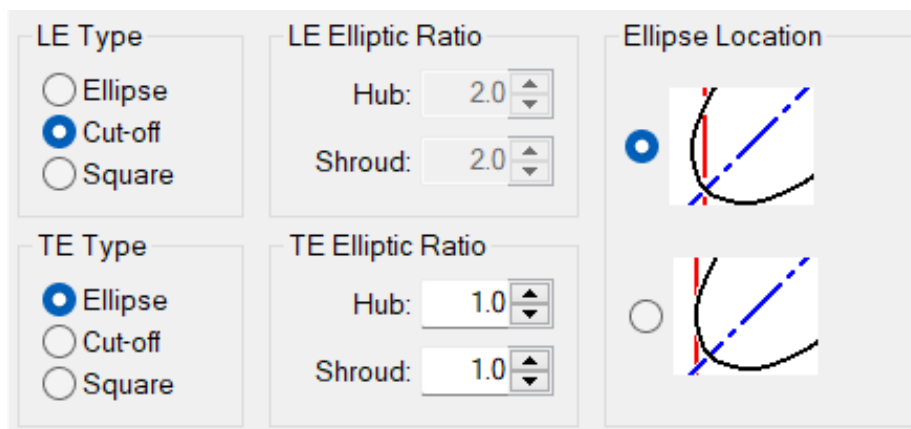


Figure III.4.2. Changing the type of the blade's trailing edge.

Step 4. Adding the TurboGrid program module to the Ansys Workbench project, the next step is to create a mesh model of one of its inter-blade channels in the TurboGrid program based on the spatial geometry of the diffuser created in the BladeGen program.

For this, it is necessary to add a TurboGrid module to the Ansys Workbench project, which is linked to the previously used BladeGen module. To do this, you need to right-click on the BladeGen module in the structural diagram construction window and select the Transfer Data to New command from the list that appears, and then select TurboGrid from the list of programs.

As a result, data will be automatically transferred from BladeGen to TurboGrid.

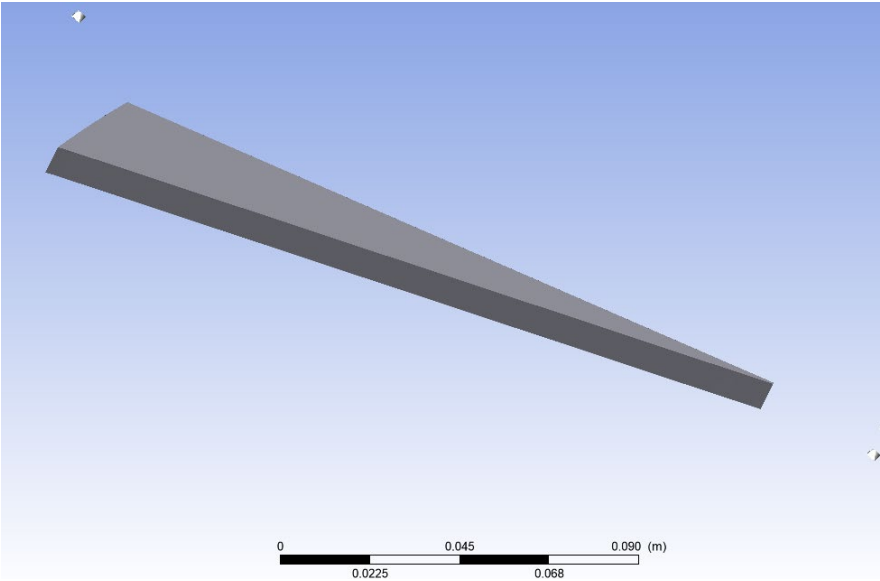


Figure III.4.3. 3d model of the Blade diffuser obtained in *TurboGrid*.

Step 5. Launching the TurboGrid program, the program is launched by double-clicking the left mouse button on the TurboGrid module in the Ansys Workbench program workspace. After launching, the program automatically loads data about the geometry of the blade diffuser, and the user only has to adjust the parameters of the finite element mesh.

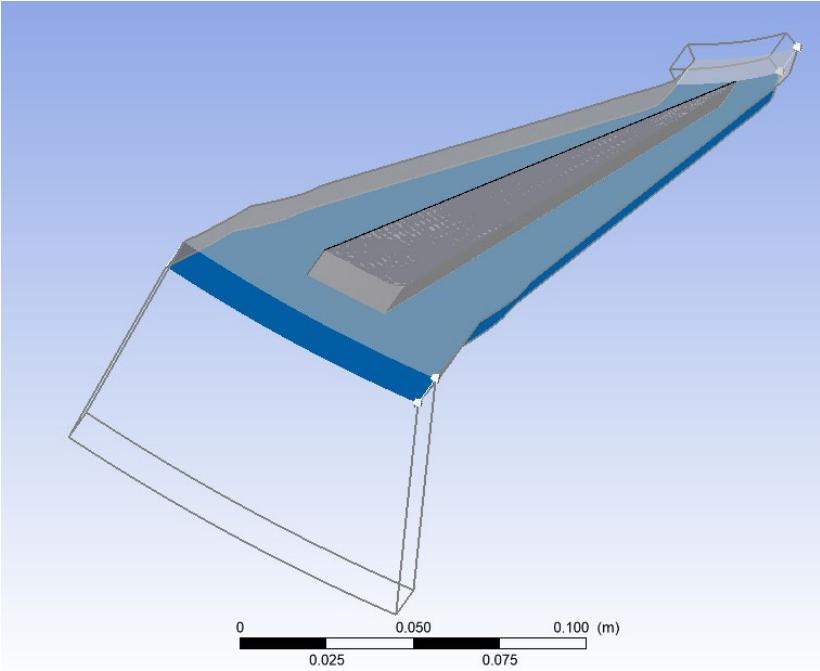


Figure III.4.4. TurboGrid program window with the loaded geometry of the diffuser.

Step 6. Description of the inlet and outlet sections, the next step is to set (refine) the position of the inlet and outlet boundaries of the blade vane computational domain.

To display the inlet (Inlet) and outlet (Outlet) boundary, you need to check these boundaries in the project tree. After that, the inlet boundary is highlighted in green, the outlet - in red.

You can see that by default, the inlet and outlet are set at some distance from the boundaries of the computational domain. The fact is that TurboGrid automatically positions the inlet and outlet areas so that the size of the computational domain is minimal, but sufficient for constructing a high-quality mesh around the blade feather.

Since the model of the process in the diffuser will be used in a single compressor model, this is unacceptable, as both boundaries must exactly coincide with adjacent elements. Therefore, it is necessary to set the inlet and outlet exactly along the boundaries of the computational domain.

For this, you should open the properties editing menu of the inlet area by double-clicking the LMB on the Inlet item in the project tree. The main part of it is a table containing the coordinates of the inlet boundary points.

Step 7. Description of the mesh topology When overlaying a finite element mesh on computational areas of complex geometry, for example, turbomachines, often the only way to get a high-quality orthogonal mesh is to use a block structure.

The essence of this approach lies in dividing the geometry of the computational area into blocks, each of which can be guaranteed to be divided by a high-quality mesh. This approach is implemented in the TurboGrid program in a fully automatic mode.

In it, the construction of a finite element mesh begins with the division of geometry into structural blocks. The principal scheme of dividing geometry into blocks in the program is called topology (*Topology*).

In the TurboGrid program, the construction of topology can be performed in a fully automatic mode. However, as practice shows, for mixed-type diffuser, it is necessary to use a standard topology with control points.

To construct the topology, you need to double-click the LMB in the object tree on the Topology Set item. In the appeared menu, in the *Topology Definition* → *Placement list*, you should select the Traditional with Control Points item and confirm the selection by pressing the *Apply* button.

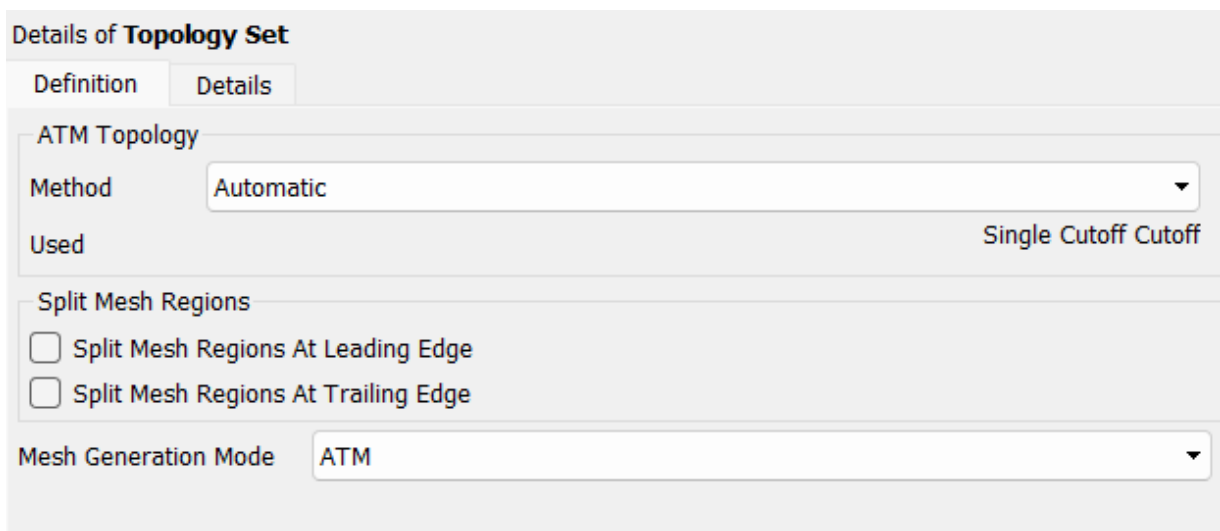


Figure III.4.5. Description of the mesh topology in automatic mode.

Step 8. Setting the number of mesh elements, the number of finite elements and mesh density are important indicators determining the accuracy of the calculation.

The mesh density, especially in areas of high velocity gradients, for example, in boundary layers, should be sufficient for a high-quality description of the effects occurring there.

Setting the mesh density in the TurboGrid program is done in the Mesh Data menu, which can be called by clicking the LMB in the corresponding place of the object tree.

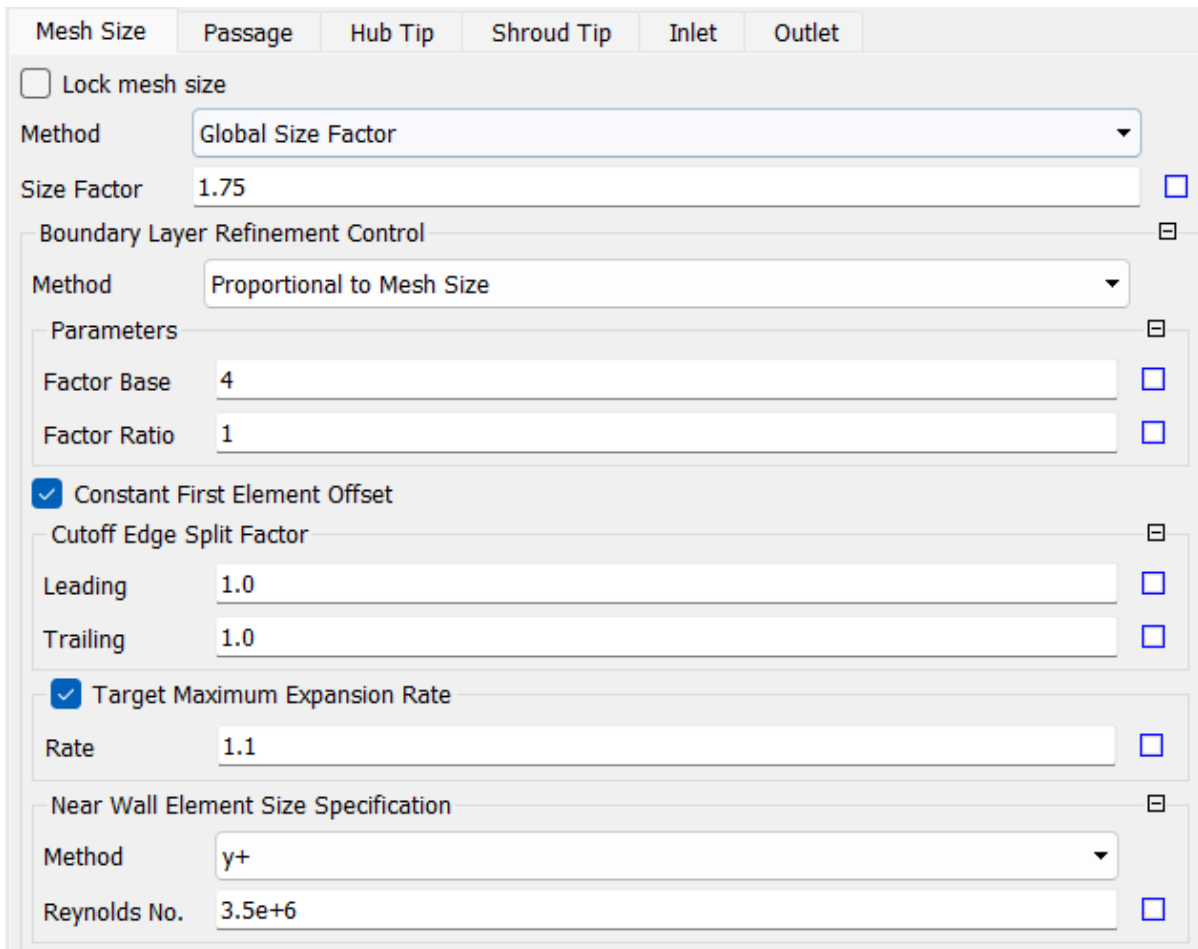


Figure III.4.6. Setting the density of the finite element mesh of the diffuser.

In this menu, in the Mesh Size tab, in the Method field, the method of setting the mesh density is selected. In this field, from the drop-down list, you should select the Global Size Factor item.

Also, the quality of the mesh at the blade walls should be described. For this, in the Method field of the Near Wall Element Size Specification section, you should select the y+ item, and below enters the Reynolds number value characteristic for this impeller **Figure III.4.6.**

Upon completion of all field assignments, you need to confirm all the selected settings with the Apply button. As a result of the operation, a preview of the obtained mesh will appear on the surfaces of the meridional outlines.

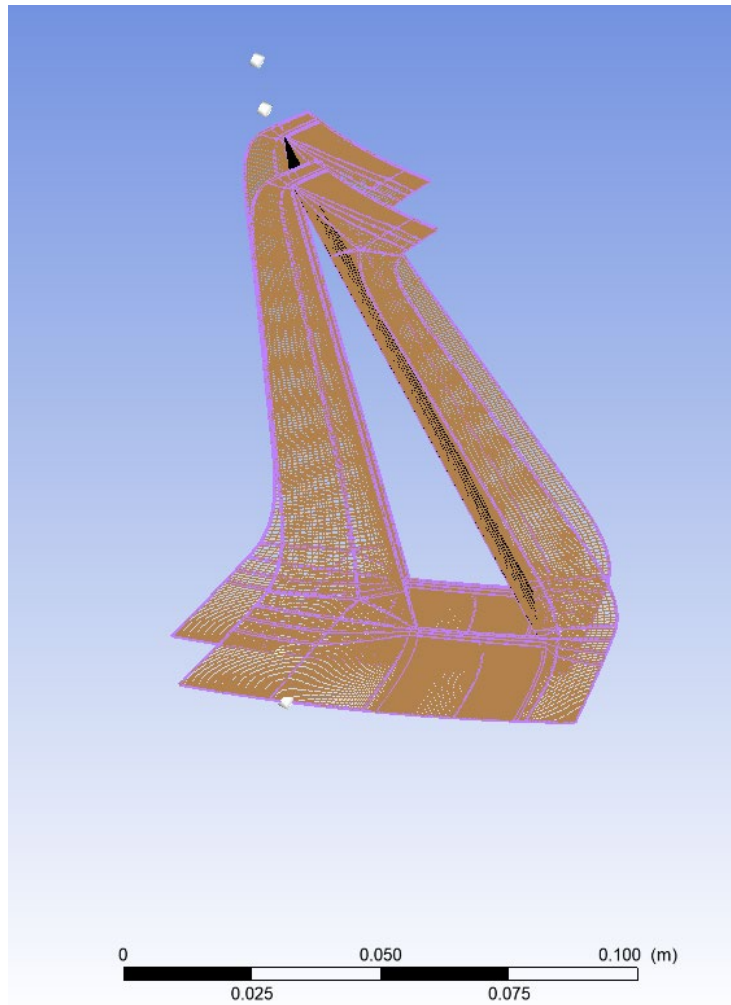


Figure III.4.7. A preview of the obtained mesh.

Step 9. Building a finite element mesh If as a result of creating a mesh in the project tree **there are signs**, then this means that there are elements with a negative volume in the mesh you generated, or the quality parameters of the mesh go beyond the recommended ones.

The peculiarity of the chosen topological division is the possibility of manually moving the control points of topological blocks.

For convenience of moving control points, you need to right-click in the visualization window and select the Transformation tab, then Blade-to-Blade (Theta M).

Then in the top menu, you need to enable cursor binding to geometry using the icon. After that, you need to select the control point with the LMB and, holding the LMB pressed, move it.

By moving the topological control points, you can achieve a significant improvement in the quality parameters of the computational mesh.

Now, when the topology has been fully defined and the number of finite elements has been selected, you can generate a mesh by pressing the Generate button in the 3D-Mesh menu.

At this point, a three-dimensional mesh of the specified density will be created (**Figure III.4.8**) and the mesh quality analysis (Mesh Analysis) in the project tree will become active.

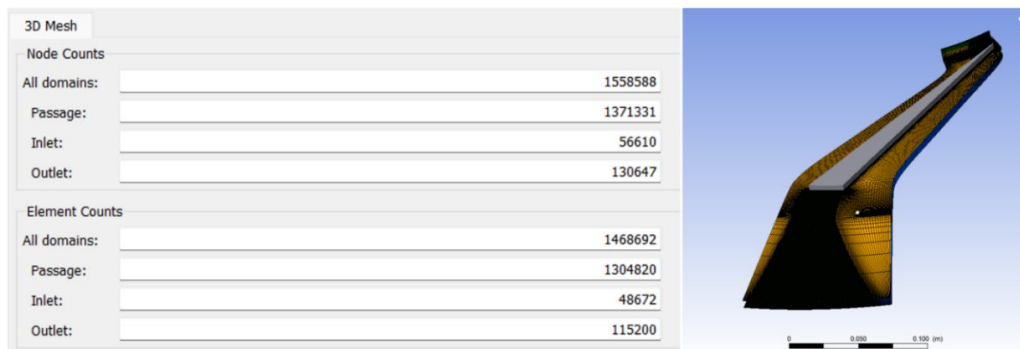


Figure III.4.8. Viewing information about the finite element mesh.

Mesh quality control is carried out in the same way as when creating blade rims of a centrifugal compressor (Section 2)

Step 10. Saving the created mesh model of the blade diffuser to save the created finite element model of the axial turbine blade vane, you need to press the *Save Mesh* button. In the appeared window, you need to specify the file name - “Stator” and press the Save button.

As a result, a file for Ansys CFX with the extension *.gtm - Stator.gtm is created in the working folder.

III.5. TECHNOLOGY OF COMPUTATIONAL STUDY OF THE WORKING PROCESS OF A CENTRIFUGAL COMPRESSOR STAGE

Step 1. Launching the *Ansys CFX* program, the creation of a numerical model of the compressor under study, based on previously created computational models of its components, and the calculation and processing of its results are carried out in the *Ansys CFX* program, which is part of the *Ansys Workbench* software suite.

To launch Ansys CFX in such a way that the previously created computational model of the impeller is automatically loaded into the program, you need to perform the following actions:

- Right-click on the Turbo Mesh item of the Turbo Grid sub-block;
- In the appeared list, select the command Transfer Data to New;
- In the second opened list, select CFX. Next, you need to add the created diffuser models to the same CFX block. For this, the following sequence of actions is performed:
- Left-click on the Turbo Mesh item of the Turbo Grid sub-block, related to the diffuser;
- Without releasing the LMB, “drag” the cursor to the Setup item of the CFX block.
- Perform the specified actions of all diffuser models included in the system. As a result, in the window of building structural diagrams of Ansys Workbench, a CFX block will appear, linked with TurboGrid blocks (**Figure III.5.1**).

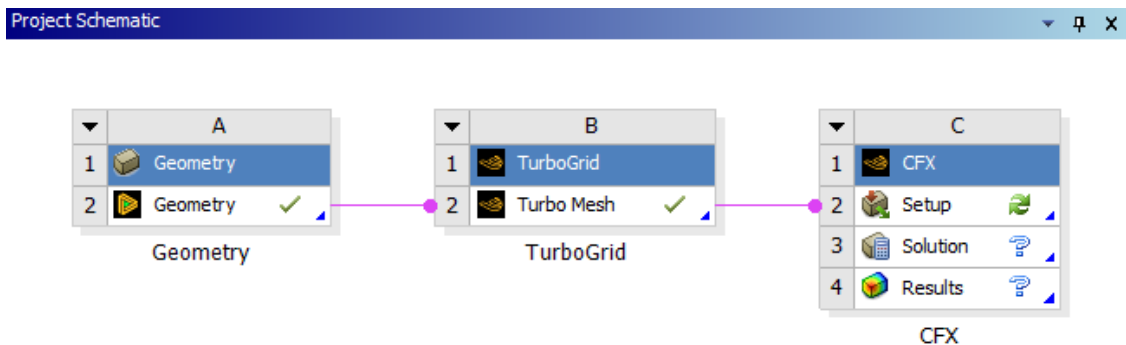


Figure III.5.1. View of the area for building structural diagrams after adding the *Ansys CFX* module.

After that, you should double-click the LMB on the Setup line of the CFX block. As a result, the preprocessor window (module for creating a numerical model) of the *Ansys CFX Pre* program will open with a computational model of the impeller and diffuser loaded into it (**Figure III.5.2**).

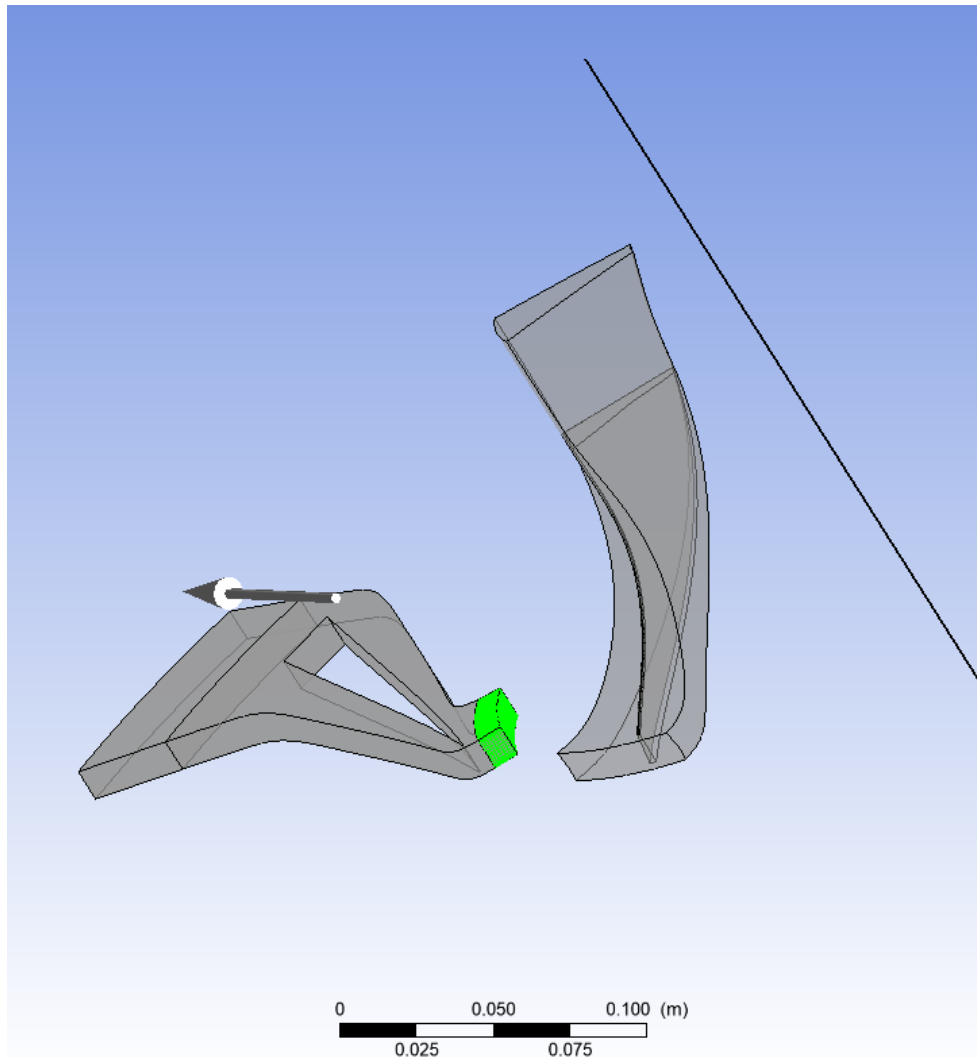


Figure III.5.2. Ansys *CFX Pre* program window with the loaded impeller and diffuser model.

Step 2. Matching the impeller and outlet system meshes, As can be seen from the figure, the computational models of the impeller and diffuser do not coincide with each other (the exit from the impeller does not border with the entrance to the first diffuser).

To correct these problems, you need to perform the following actions.

Rotate the radial diffuser by 45° relative to the OZ axis. For this, you also need to use the Transform Mesh command, but make different settings there. In particular, in the Transformation field, you should select the method of transforming the model – Rotation (rotation). In the Axis field, the axis of rotation is selected (Z), and in the Rotation Angle field – the angle of rotation - -45° . The settings made are confirmed by pressing the Apply button (**Figure III.5.3**).

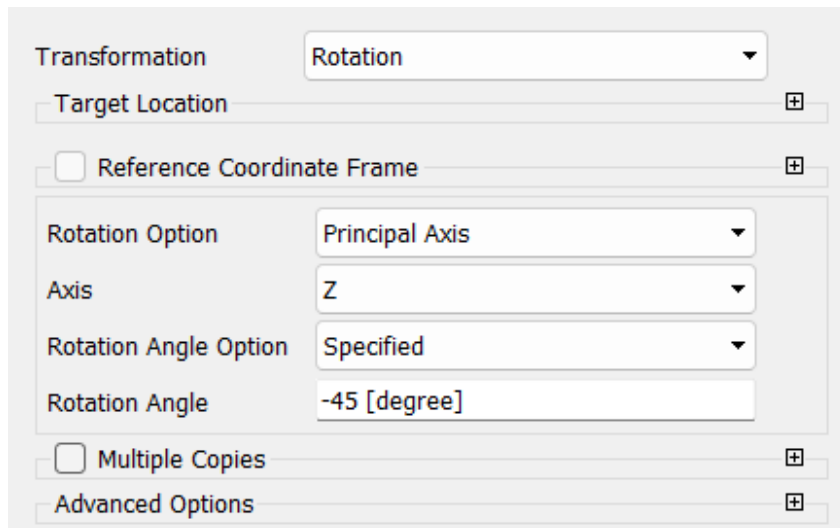


Figure III.5.3. Rotating the outlet system model around the OZ axis.

Step 3. Launching the turbo template, The Ansys CFX Pre software suite has a special Turbo template, which helps the user to create a computational model of the working process in a turbomachine in an automated mode, significantly reducing the labor intensity of its description. To launch the turbo template, you need to select the Tools item in the top menu and activate the Turbo Mode command in the appeared list.

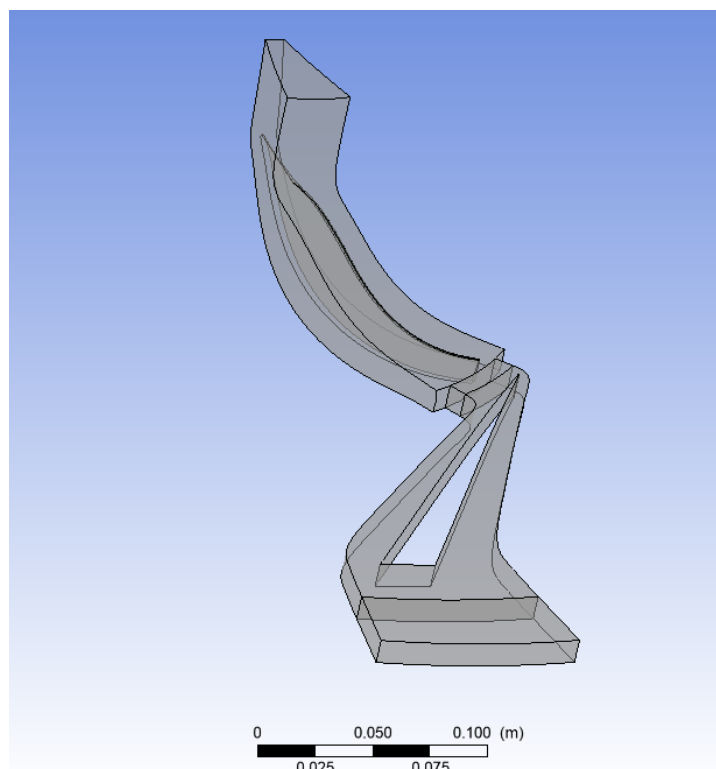


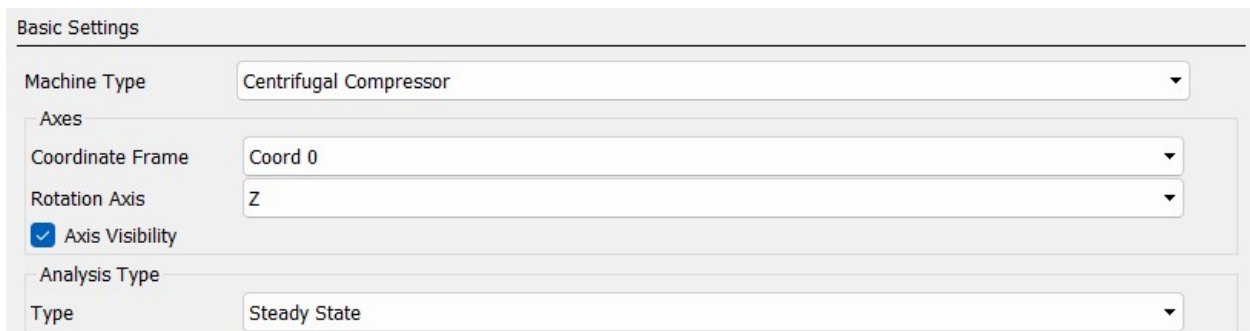
Figure III.5.4. Result of matching the compressor elements.

After launching the command, the user will sequentially get access to several forms in which it is necessary to enter information about the modeled turbomachine.

Step 4. Choosing the type of turbomachine, Setting the task, and the axis of the turbomachine

After activating the turbo template, the first dialog box will appear in which you need to specify the type of turbomachine, set the task, and the axis of rotation. To do this, you should make the following settings:

1. In the Machine Type field (type of turbomachine) from the drop-down list, the type of turbomachine is selected - Centrifugal Compressor (centrifugal compressor).
2. In the Rotation Axis field, the axis of rotation is selected - the Z axis.
3. It is indicated that the task will be solved in a stationary setting by selecting the Steady State item in the Type list (**Figure III.5.5.**).
4. The choice is confirmed by pressing the Next button



Basic Settings	
Machine Type	Centrifugal Compressor
Axes	
Coordinate Frame	Coord 0
Rotation Axis	Z
<input checked="" type="checkbox"/> Axis Visibility	
Analysis Type	
Type	Steady State

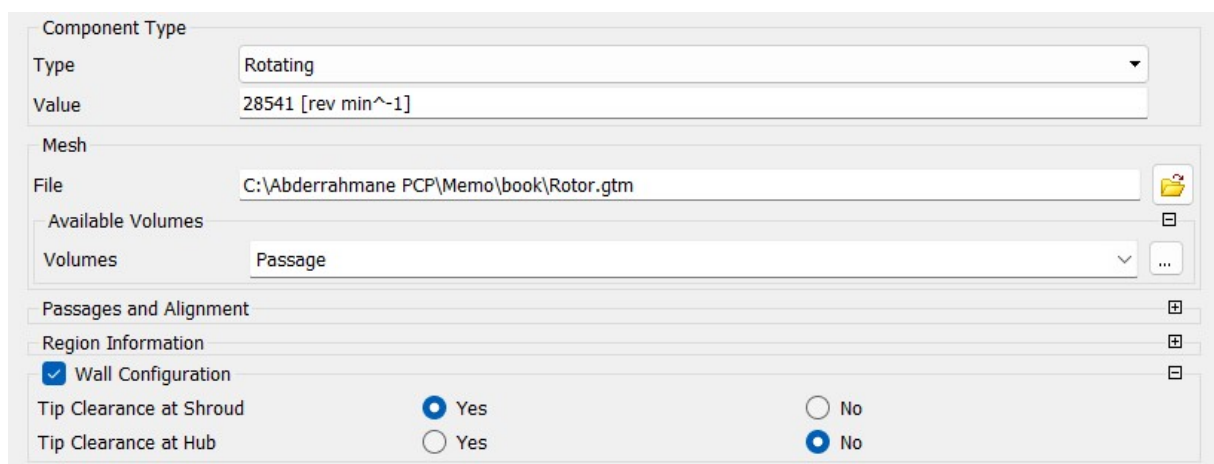
Figure III.5.5. Filling in the first dialog box of the turbo template.

Step 5. Adding components included in the turbomachine After completing the previous step, The user will go to the next page of the turbo template, where it is necessary to indicate which parts make up the studied turbomachine, in what order they are arranged, and specify the previously created files containing finite element models. Here, the motion parameters of the computational models are also determined.

It should be noted that the program automatically determined that the modeled centrifugal compressor consists of one moving element including all domains, which does not correspond to reality.

To describe the components of the modeled turbomachine and the order of their sequence, you need to perform the following actions.

1. Describe the first element of the compressor in the order of sequence - the impeller. For this, in the Components list, you need to select the component **R1** with a click of the LMB. After that, elements describing the properties of this component will appear below the list. For the impeller, you need to make sure that in the Type field it is indicated that this element rotates (*Rotating*). In the Value field, the rotation frequency value is entered. Please note that the direction of rotation is indicated in the model building window by an arrow, and if necessary, it can be changed by changing the sign of the rotation frequency. In the Available Volumes field, you should indicate the compacts of the computational domain related to the impeller. The selected domains are highlighted in green in the model building window. For the modeled compressor, for the **R1** area, only the impeller domain (Passage), created in section 2 (**Figure III.5.6**), should be left highlighted.



The screenshot shows a software interface for configuring a component. The 'Component Type' section has a 'Type' dropdown set to 'Rotating' and a 'Value' field containing '28541 [rev min^-1]'. Below this is the 'Mesh' section, with a 'File' field containing 'C:\Abderrahmane PCP\Memo\book\Rotor.gtm' and an 'Available Volumes' dropdown set to 'Passage'. Further down, the 'Passages and Alignment' section is expanded, showing a 'Wall Configuration' checkbox that is checked. The 'Region Information' section is also expanded. At the bottom, there are two sections for 'Tip Clearance': 'Tip Clearance at Shroud' with a 'Yes' radio button selected, and 'Tip Clearance at Hub' with a 'No' radio button selected.

Figure III.5.6. Setting the parameters of the impeller domain.

2. Describe the other components of the stage - diffuser. To add an additional element to the stage model, you need to right-click on the Components item. A list will appear in which you should select the Add Component command. After its launch, a dialog box will appear in which you should specify the name of the newly added component and its type (moving or stationary). The diffuser of the modeled compressor is stationary.

After performing the specified manipulations, the name of the created component will appear as the bottom line in the Components list.

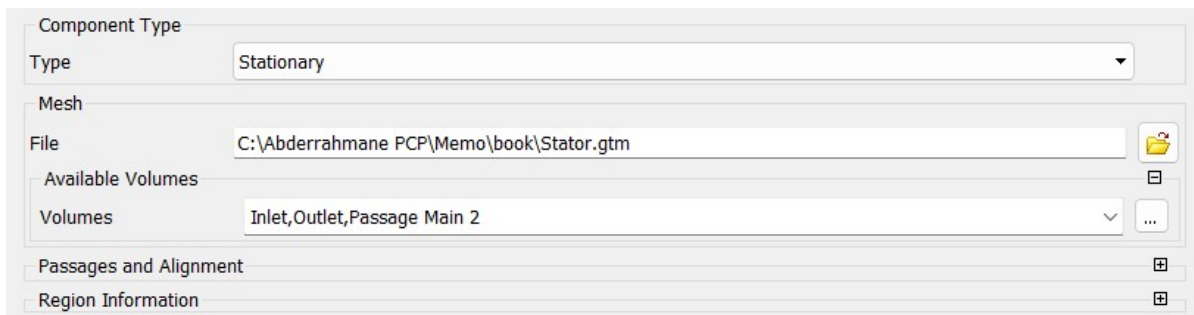


Figure III.5.7. Setting the properties of the outlet system.

3. Set the parameters for the first diffuser. Here you need to specify which of the finite element meshes loaded into CFX corresponds to the newly created component. For this, in the list, in the Available Volumes field, you need to select the mesh corresponding to the radial diffuser (Inlet, Outlet, Passage Main 2) (**Figure III.5.7**).
4. Go to the next page of the turbo template by pressing the Next button.

Step 6. Setting the values of flow parameters at the boundaries, On the next page of the template, the user should set the numerical values of the flow parameters at the inlet and outlet boundaries, specify the turbulence model and the properties of the working fluid. The setting is done in the following sequence:

1. In the Fluid field, it is specified that air, obeying the ideal gas equation (Air Ideal Gas), will be accepted as the working fluid.
2. In the Flow Direction field, it is specified that the flow direction at the inlet boundary will be indicated normal to the boundary (Normal to Boundary).
3. A reference pressure, Reference Pressure, equal to zero is set.
4. In the Turbulence list, the **Shear Stress Transport SST** turbulence model is selected.
5. In the Inflow/Outflow Boundary Templates list, select the combination of inlet and outlet boundary conditions that will be used when solving the problem. For modeling the compressor described in section 2, it is advisable to use the combination P-total Inlet P-static Outlet. This will indicate that the user intends to specify the values of total

pressure and total temperature at the inlet boundary, and static pressure will be specified at the outlet boundary.

6. In the P-Total field, enter the value of the total pressure at the inlet boundary in Bars.
7. In the P-Total field, enter the value of the total temperature at the inlet boundary in Kelvin.
8. In the P-static field, enter the value of the static pressure at the outlet of the compressor in Bars (or enter it as an input parameter to use different values).
9. In the Interface Default Type field, you need to select the method of data transfer between the domains of the impeller and the outlet system Stage. When using such an interface, data from the block located higher in the flow is averaged in the circumferential direction and transferred to the next block as an input boundary condition.
10. After performing the specified settings, you should go to the next page of the turbo template by pressing the *Next* button.

Physics Definition

Fluid: Air Ideal Gas

Model Data

Reference Pressure: 0 [bar]

Heat Transfer: Total Energy

Turbulence: Shear Stress Transport

Inflow/Outflow Boundary Templates

None

P-Total Inlet P-Static Outlet

P-Total Inlet Mass Flow Outlet

Mass Flow Inlet P-Static Outlet

Inflow

P-Total: 0.6 [bar]

T-Total: 296 [K]

Flow Direction: Normal to Boundary

Outflow

P-Static: BP

Interface

Default Type: Stage (Mixing-Plane)

Solver Parameters

Figure III.5.8. Setting the values of flow parameters at the boundaries.

Step 7. Checking the created interfaces, the next page of the turbo template contains a list of created interfaces. An interface is additional boundary conditions that are imposed on the mesh of the working area. These conditions include periodicity on the side faces of domains, as well as the order of connection between adjacent parts of different domains. At this stage, it is necessary to check the correctness of the creation of interfaces and then go to the next page by pressing the Next button.



Figure III.5.9. Interface control page.

Step 8. Checking boundary conditions, the next page of the turbo template provides a list of created boundary conditions. They need to be checked, corrected if necessary, and go to the next page by pressing the Next button.



Figure III.5.10. Boundary control page.

At this stage, the work of this wizard is completed, and you exit to the usual ANSYS CFX – Pre menu. To do this, in the operation tab, you need to select Enter General Mode and press the Finish button. The standard view of the *ANSYS CFX – Pre* program working window will appear on the screen.

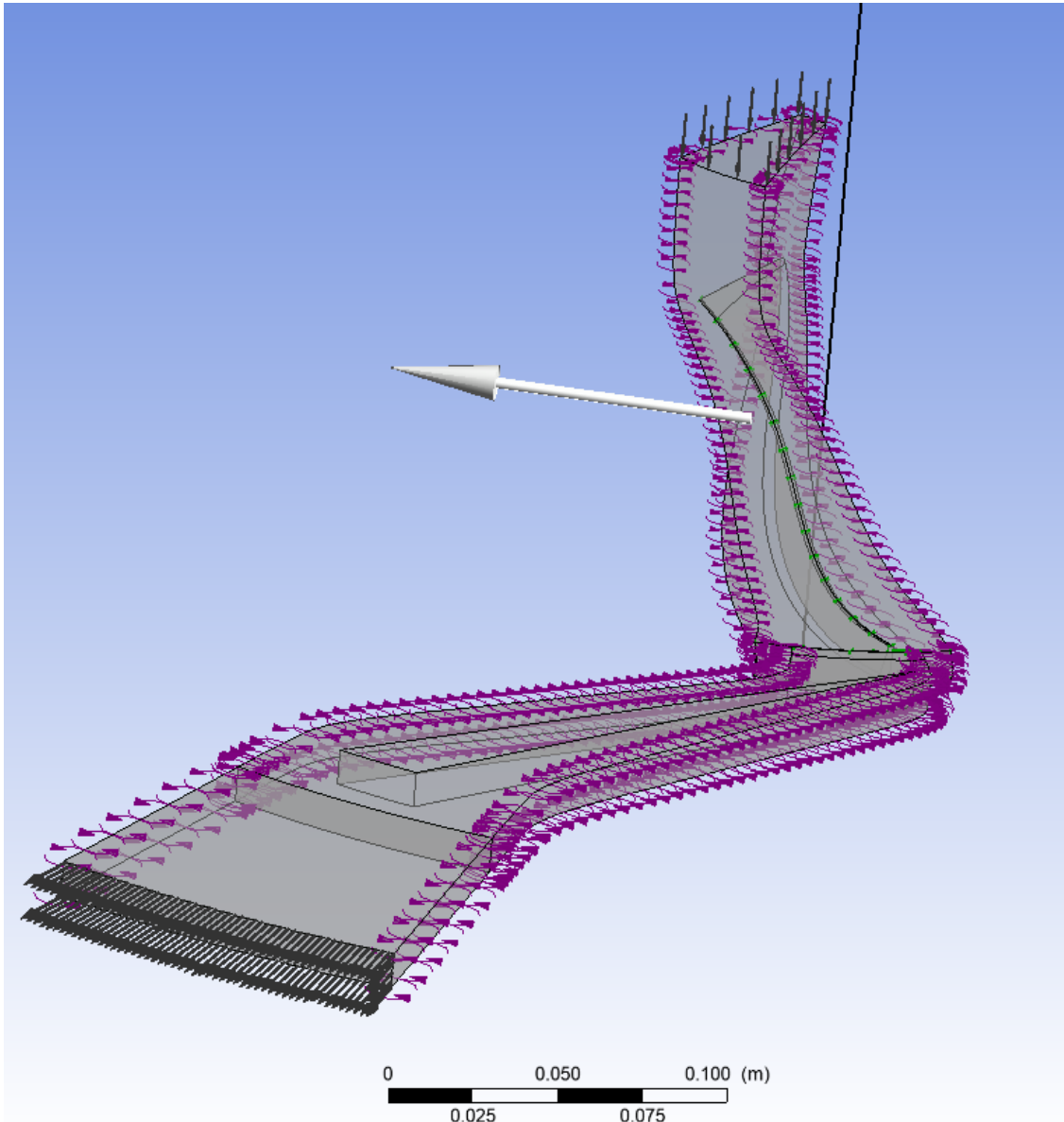


Figure III.5.11. View of the model in Ansys *CFX – Pre* program after completing the work of the turbo template.

At this point, the creation of a numerical model of the working process in the model compressor is completed. The settings made need to be saved by pressing the Save button. After that, the Ansys *CFX – Pre* program window can be closed.

- In the Initialization Option list, indicate that the task will be solved from “scratch” (Initial Condition);
- In the Run Mode list, indicate that the task will be solved using several processors of one computer (if the used computer has them) (Platform MPI Local Parallel);

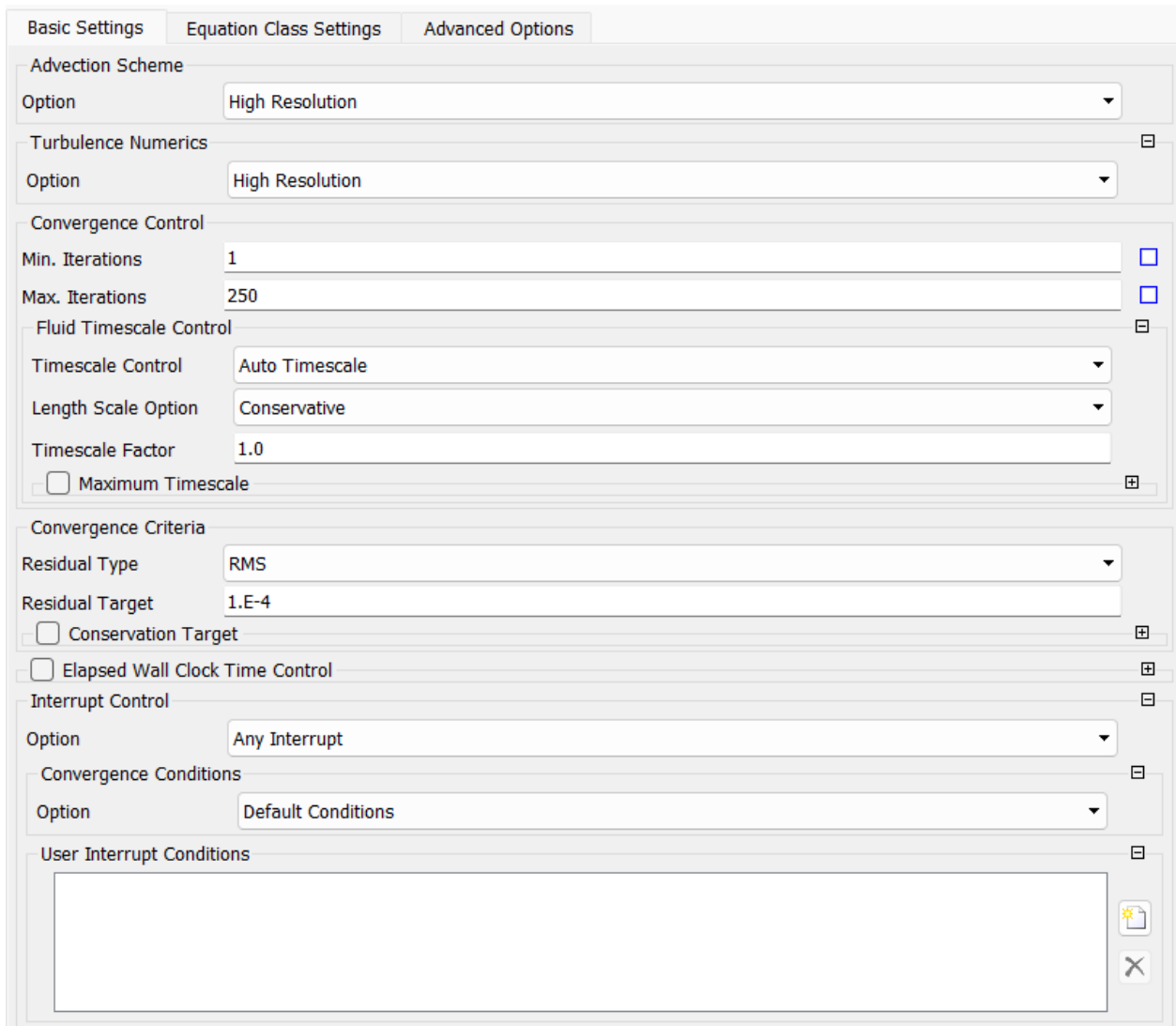


Figure III.5.12. Setting the solver parameters.

- Using the “+” and “-” buttons, set the required number of cores for solving the task;
- Start the calculation process by pressing the Start Run button.

After that, the process of solving the task will start, and in the Ansys CFX Solver program window, the change in residuals will be displayed as a text file and graphs (**Figure III.5.14**).

The solution process will stop automatically if the maximum number of iterations specified when setting the solver parameters is performed, or if the residuals for all equations are less than the specified value.

If necessary, the solution process can be stopped by pressing a button in the top menu.

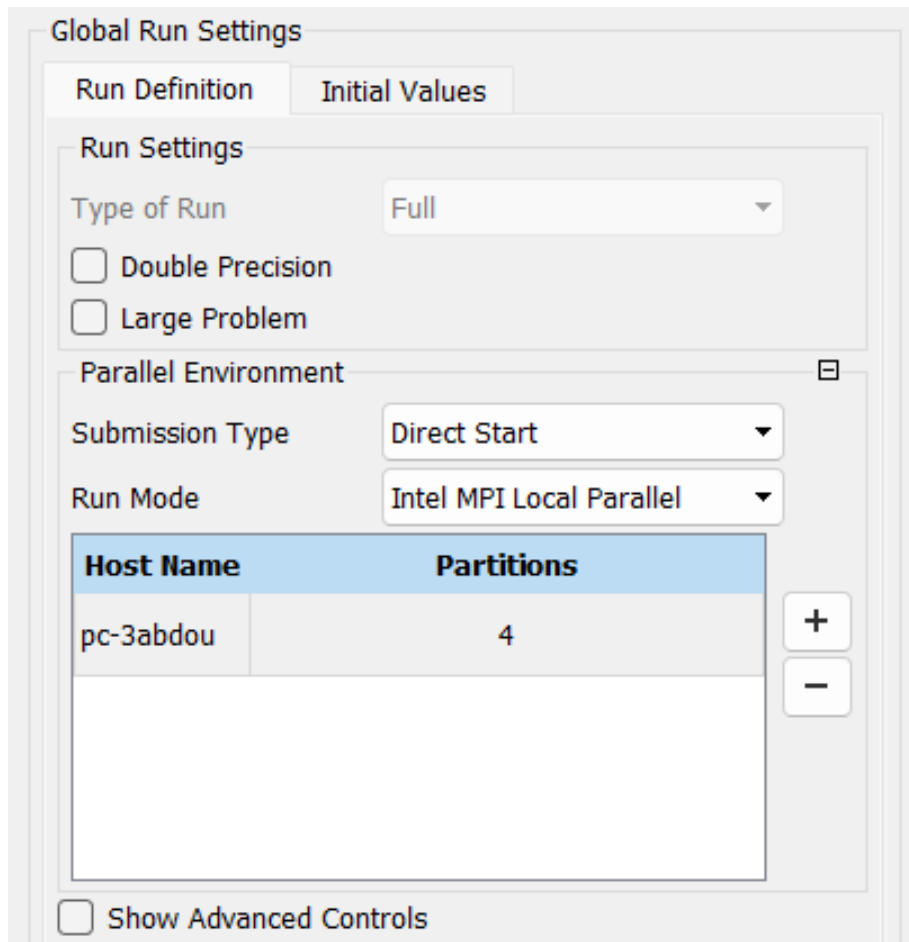


Figure III.5.13. Starting the task-solving process.



Figure III.5.14. View of the Ansys CFX Solver program window during the solution process.

Table III.5. Compressor details for $r4/r2 = 1.14$ at **80%** speed.

Shaft speed (80%)	28,541 <i>rpm</i>
Impeller tip radius (r2)	135 <i>mm</i>
Number of impeller blades	15
Blade back sweep angle at impeller exit	38°
Impeller leading edge tip clearance	0.684 <i>mm</i>
Impeller trailing edge tip clearance	0.358 <i>mm</i>
Number of diffuser vanes	23
Diffuser vane setting angle (α_{4SS})	16.50°
Diffuser channel height	11.10 <i>mm</i>
Diffuser leading edge radius	140.40 <i>mm</i>
Plane 2M radius	139 <i>mm</i>
Plane 8M radius	335 <i>mm</i>

CHAPTER IV: RESULTS

IV.1. INTRODUCTION

The following sections present the results obtained by each turbulence model. Where possible, predictions are compared to experimental data. One dimensional data is available for all operating points considered, e.g., pressure and temperature, whereas local experimental contour plots are available the operating points P, M and S.

Boundary conditions

The inlet conditions were specified as a total pressure of **0.6 bar** and a total temperature of **296 K** (23°C) based on the recommendations by the authors of the test case. The fluid is defined as Air Ideal Gas and the no-slip boundary condition was defined at all solid wall surfaces. The specific heat capacity at constant pressure C_p and ratio of specific heats γ are **1005 J/kg·K** and **1.4**, respectively. It is known that CFD solvers run into difficulty at/near the stall/surge and choked flow conditions depending on the outlet boundary condition specified. Typically, a static pressure boundary condition is placed at the outlet near choke conditions and a mass flow boundary condition near stall/surge. [1]

In this analysis, the exit corrected mass flow rate $\dot{m}_{exit\ Corr}$ has been used. It is a function of the stage mass flow rate, and mass averaged total temperature and pressure at the outlet plane, 8M (Ansys 23R2). This makes it more stable compared to a static pressure or regular mass flow rate condition. Finally, the location of the impeller-diffuser interface is mid-way along that $r_4/r_2 = 1.14$.

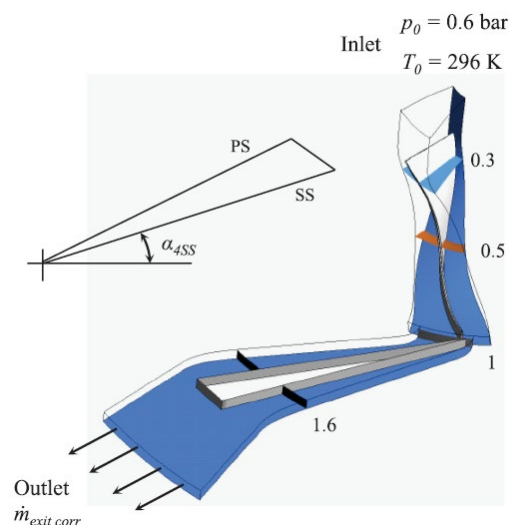


Figure IV.1. Computational domain and boundary conditions.

Three operating points were simulated along the 80% Speedline (**P** [near surge], **M** [mid Speedline] and **S** [near choke]) to determine how each turbulence model performs under different operating conditions.

IV.2. GRID CONVERGENCE STUDY WITH MESH SENSITIVITY AND VALIDATION

A grid convergence analysis was carried out to ensure that the solution was grid independent and the discretization error low. Three grids, namely coarse, medium and fine were simulated at the operating points using the **Shear Stress Transport SST** turbulence model.

This model was chosen for its numerical stability over a range of operating conditions. [28]

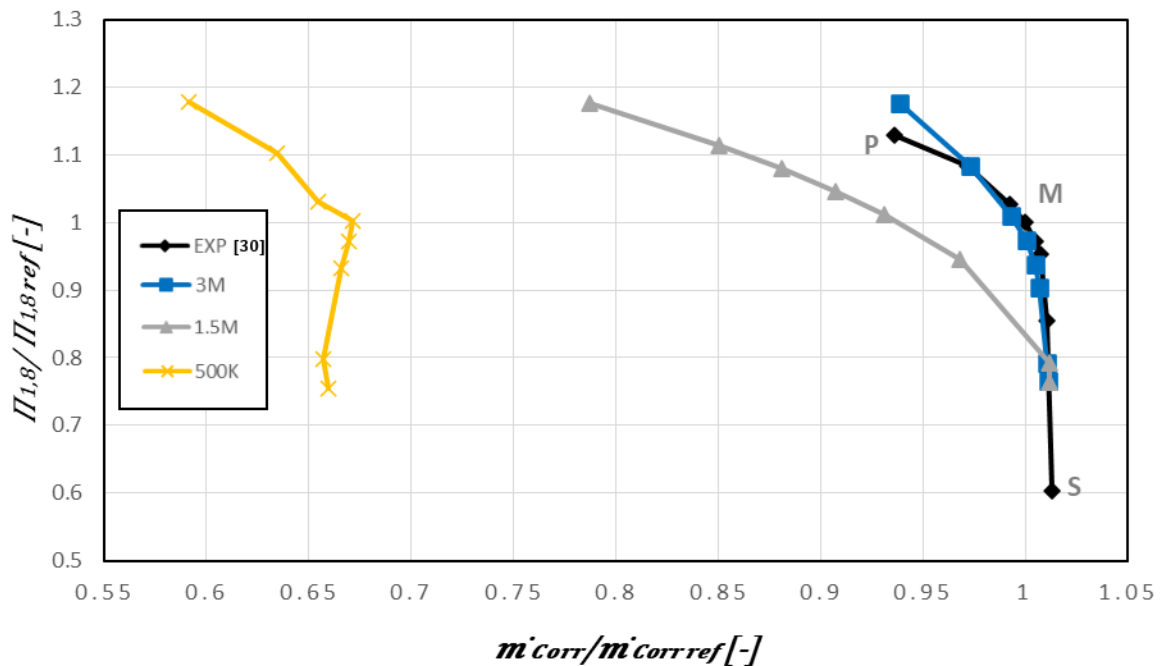


Figure IV.2.1. Total to-total pressure ratio of different grids at various operating points.

The number of elements for each grid from coarse to fine was **0.5 million (0.5M)**, **1.5M** and **3M**. Convergence was deemed to be achieved whenever the RMS residuals were less than $1E-04$, and the global imbalances of mass, momentum and energy are less than 0.1% . The percentage change in several overall parameters for operating point **P** are shown in **Table IV.2.1**.

Table IV.1. Grid refinements at the operating point P.

	$\Pi_{1,8M}$	$\tau_{1,8M}$	$\eta_{1,8M}$
C [0.5M]	1.65148	1.39793	0.41032
M [1.5M]	1.67143	1.34283	0.47436
F [3M]	1.67729	1.34472	0.47273

Another method used for analyzing the simulations for grid independence was by comparing circumferentially mass averaged, spanwise velocity profiles at a number of streamwise locations through the compressor stage. The streamwise locations of the turbosurfaces used to compute the velocity profiles can be seen in **Figure IV.1**. The velocity profiles are non-dimensionalised by the blade tip speed U_2 (≈ 403 m/s). In the rotating and stationary frames of reference, the relative and absolute velocities are used respectively.

The normalized velocity is shown in **Figure IV.2.2** for the operating point **P**, where the line colors correspond to the streamwise planes defined in **Figure IV.1**. The coarse grid shows a larger difference near diffuser channel exit compared to the medium and fine grids.

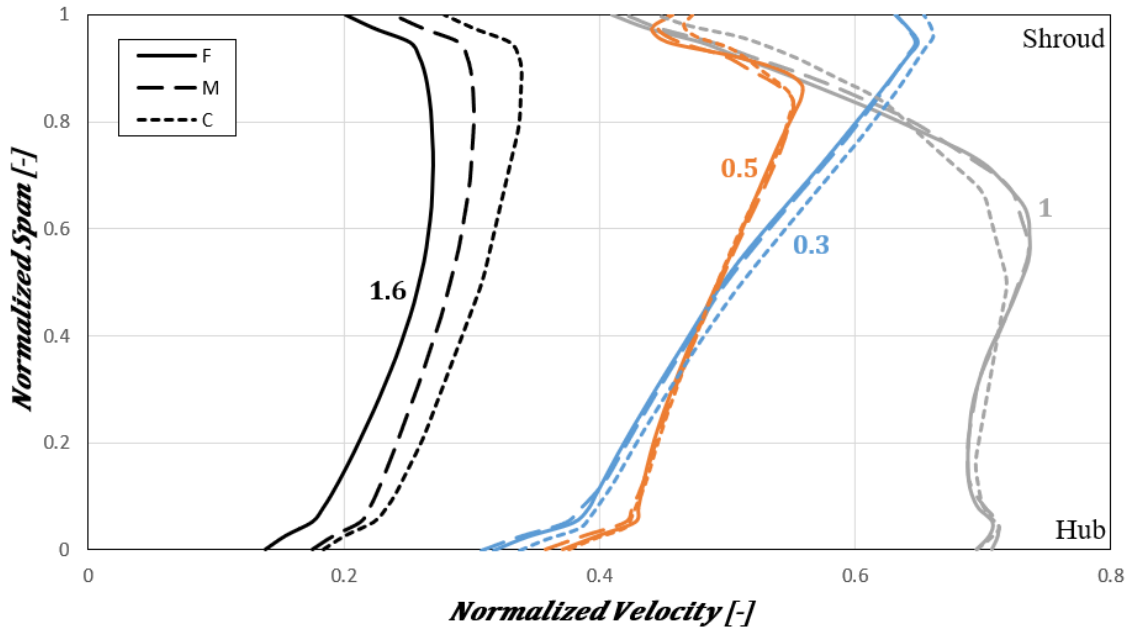


Figure IV.2.2. Velocity profiles of different grids at various streamwise locations at the operating point P.

This is due to an increased level of blockage predicted within the diffuser channel compared to the other two grids, where specifically, the coarse grid predicts 25% and the medium and fine grids predict approximately 15% channel blockage.

Based on the results of the grid convergence analysis, the Fine grid is chosen for its accuracy.

IV.3. PROCESSING OF CALCULATION RESULTS AND COMPARISON WITH DESIGN CALCULATION DATA

Processing of calculation results is carried out in the Ansys *CFX Post* program. To launch it, you should double-click the LMB on the Results line of the CFX sub-block in the Ansys Workbench mnemonic diagram construction window.

IV.3.1 The influence of the turbulence model

Using five types of turbulence models **k-ε** (K Epsilon); **k-ω** (K Omega); **S-A** (Spalart-Allmaras); **SST** (Shear Stress Transport) and **SST-CC** (Shear Stress Transport-Curvature Correction).

Global Speedlines:

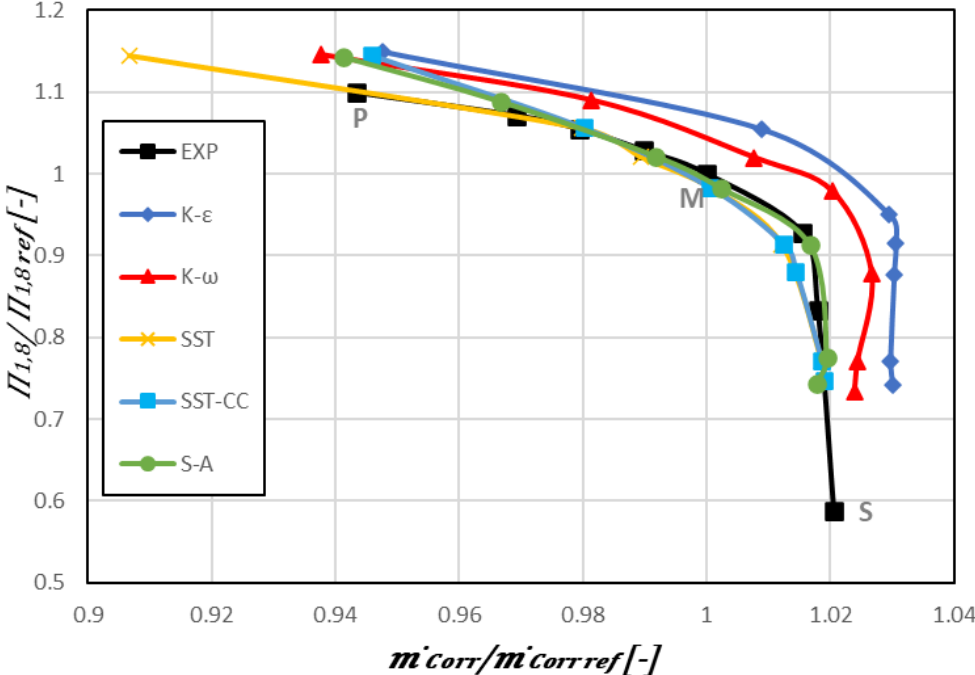


Figure IV.3.A.1. Total to-total pressure ratio of different models at various operating points.

Firstly, the Total to-total pressure ratio predictions of the compressor stage are presented in the form of Speedlines. Speedlines are shown in **Figure IV.3.A.1** for a number of different operating points of the compressor. Each model predicts the performance of the compressor in good agreement with the experiment in most cases, where the differences from the Experiment [8] are generally quite small (less than 2% in most cases).

The pressure ratio is predicted in good agreement with the experiment by each turbulence model. **S-A** predicts the total-to-total pressure in good agreement with the experiment at the operating point **P** and it predicts the total-to-total efficiency most accurately of all the models considered. The **Curvature Correction** applied to the **SST** model reduces the discrepancy in terms of total-to-total pressure ratio. However, the main drawback of the correction is in the form of a slightly reduced work input. The **k- ω** is slightly better than the **k- ϵ** . However, the differences between the models are not significant.

Measurement plane comparison:

Measurement plane Blade-to-blade. Since the **SST** model predicts the static pressure rise and the stagnation pressure loss coefficient in good agreement with the Experiment [7], this model was used as a basis for comparison to the other models with respect to entropy within the diffuser channel **Figure IV.3.A.3**.

Furthermore, at this off-design operating point (**P**), the **SST** predicts the static pressure and total-to-static efficiency best out of all models implying that this model reflects the experiment realistically with respect to one-dimensional values.

Within the diffuser channel, the **S-A**, **k- ϵ** and **k- ω** models predicts a high level of entropy generation beginning shortly downstream of the diffuser throat, which spreads towards the center of the channel, mixing with the low entropy flow near the suction side, and subsequently introduces further losses.

On the other hand, the **SST** model predicts a similar level of entropy generation downstream of the diffuser throat on the pressure side in a relatively small region, but does not tend to spread further downstream. This relatively short passage of high entropy predicted by the **SST** model is due to a small separation bubble near the shroud, whereas the **SA** model shows large flow separation.

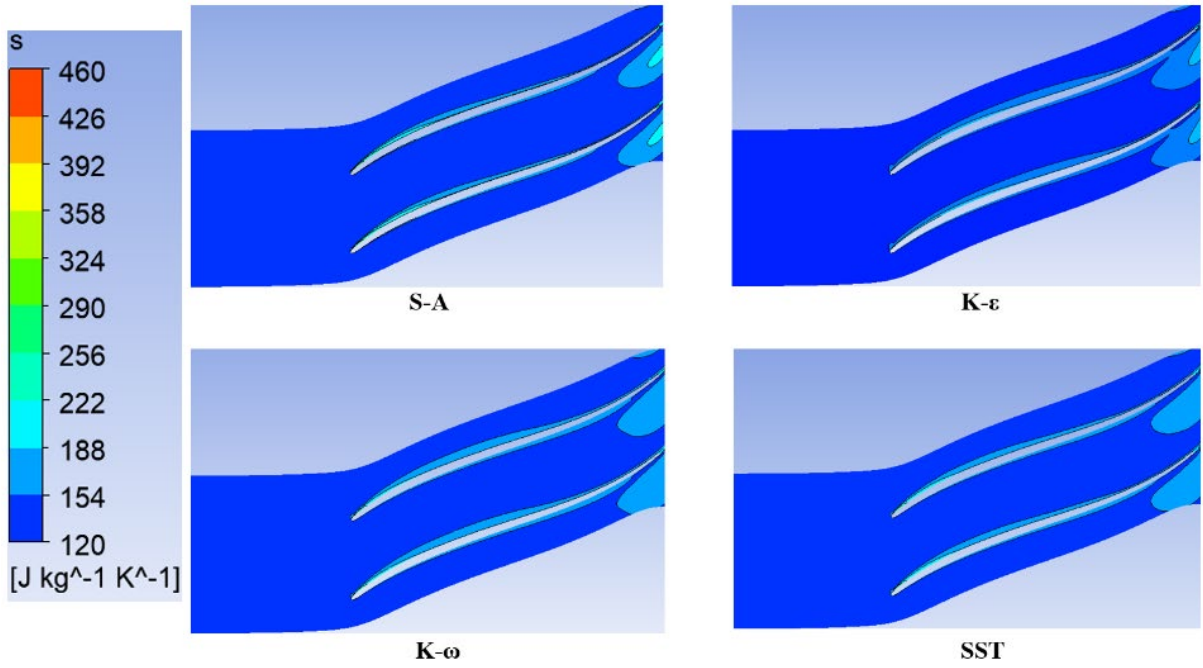


Figure IV.3.A.2. Entropy field in the impeller of different models at the operating point P.

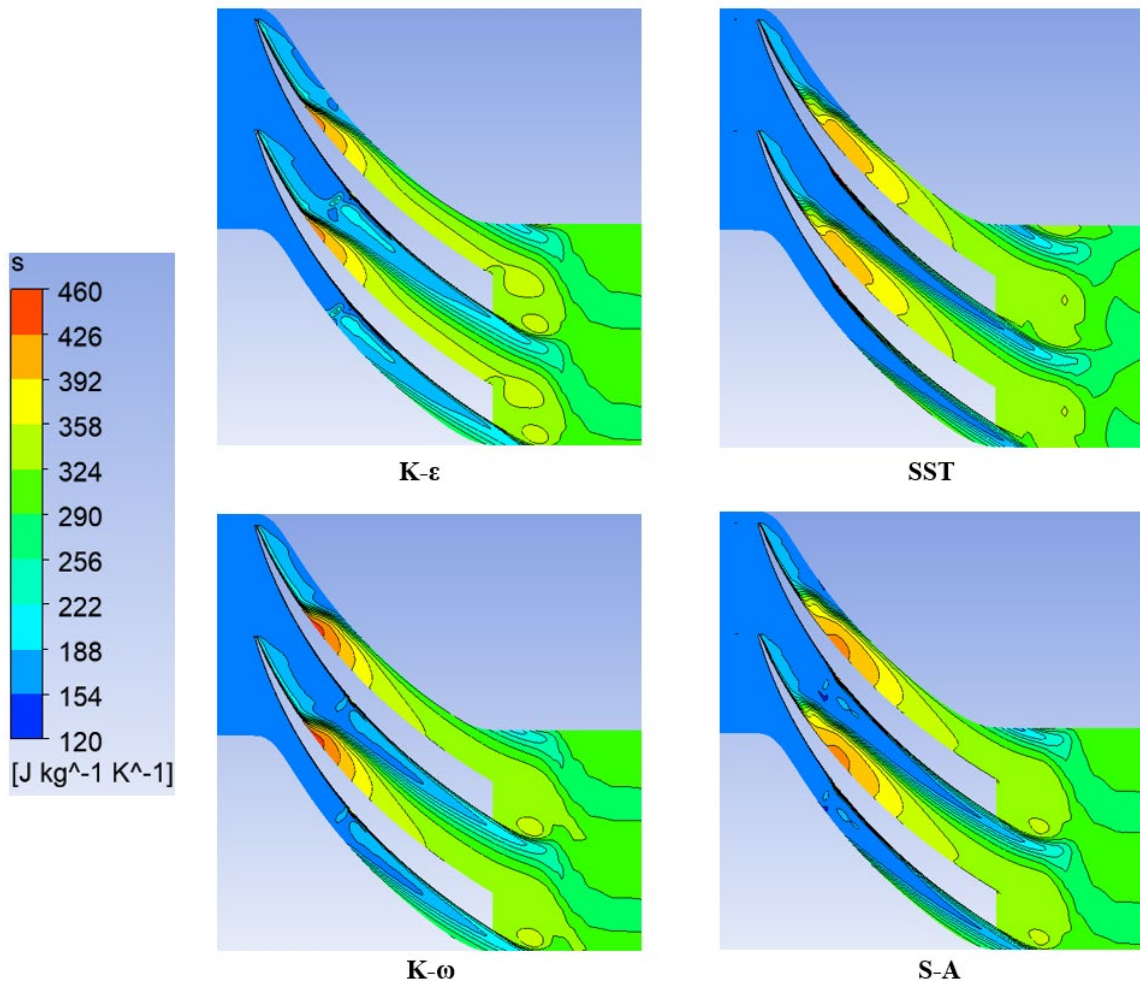


Figure IV.3.A.3. Entropy field in the diffuser of different models at the operating point P.

IV.3.2 Simulation analysis in the centrifugal compressor

The SST model provides accurate results over the entire Speedline of the present test cases whilst keeping the solution time low, with the increased accuracy in the prediction of pressure ratio and efficiency by the SST-CC model near surge compared to the original SST.

So, we chose the SST-CC model and the operating point M in order to determine certain aerothermodynamic parameters that influence the performance of the centrifugal compressor stage, among other things, pressure and temperature.

a) *The impeller*

1. Static pressures in the impeller

We distinguish a distribution of static pressure on three planes:

1.1. Meridian Plane

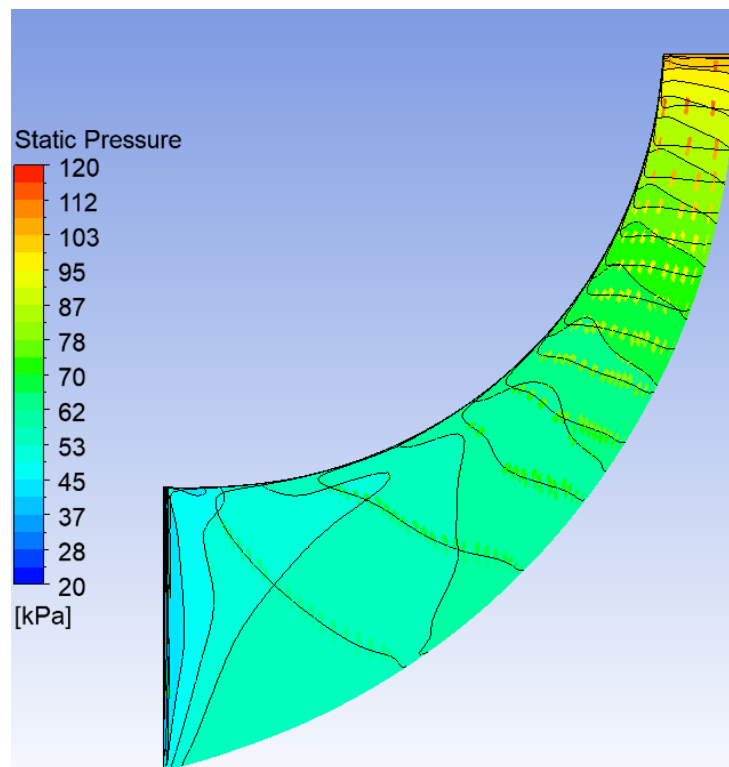


Figure IV.3.B.1. The contours of static pressure on a meridian plane of the wheel.

From the theoretical analysis given in **Chapter I**, we can geometrically divide the wheel into three zones:

– Zone “1”: At the entrance of the wheel, the radius r is small and the average radius R_m of curvature tends towards infinity since the flow is axial, this implies that the centrifugal force is important. So, the pressure gradient is established from the hub to the casing.

– Zone “2”: In the middle of the channel (in the axial radial bend), the curvature in this plane is strong but it is finite, however the centrifugal force opposes that of the force due to the curvature but it is dominant. Thus, the pressure gradient from the casing to the hub is negative.

– Zone “3”: At the exit of the wheel, the radius of curvature r is almost equal to zero, so the curvature force is negligible and the centrifugal force becomes weak, since the average radius R_m is large, so the pressure gradient is negative from the casing to the hub.

So, the mobile wheel of the compressor will increase the energy of the fluid in the form of stop pressure and heat, such as the increase in total pressure to a part and which will increase the static pressure.

1.2. Blade-to-blade plane Figure

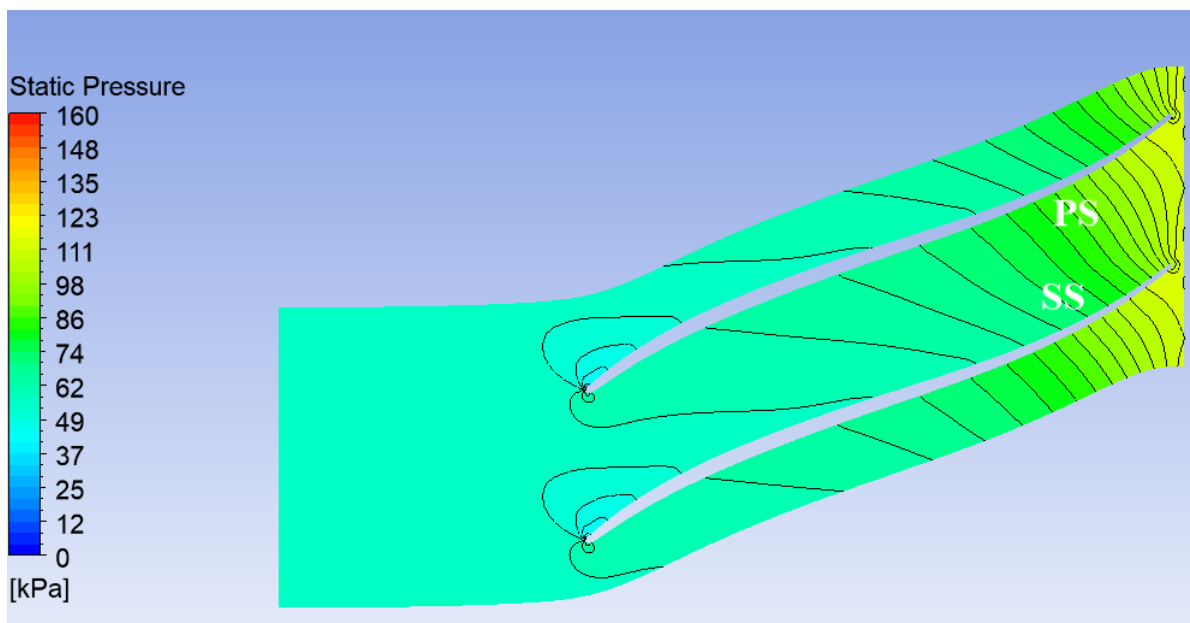


Figure IV.3.B.2. The static pressure field on a blade-to-blade plane.

The evolution of the isobars in the blade-to-blade plane can explain the following phenomena:

At the entrance of the wheel: The two forces which are, the Coriolis and centrifugal forces due to the rotation of the wheel are null, the pressure gradient according to the equation

(in **Chapter I**) is always positive from the extrados of a blade to the intrados of the next blade, and this because of the effect of the centrifugal force due to the curvature of the blade.

At the exit of the wheel: There are three forces which are, the inertia force of the particle, the centrifugal force due to the curvature of the pallet and the Coriolis force.

But, in this case, the centrifugal force due to the curvature is null since its radius is large, so the centrifugal force is always less than that of the Coriolis force, and this according to the equation of balance in the blade-to-blade plane that the pressure gradient remains positive.

1.3. Orthogonal planes

The figure below represents the evolution of static pressure in orthogonal planes. In Orthogonal Planes, the pressure gradient is positive at the extrados of a blade towards the intrados of the next blade and this, because of the influence of the Coriolis force and the force due to the curvature.

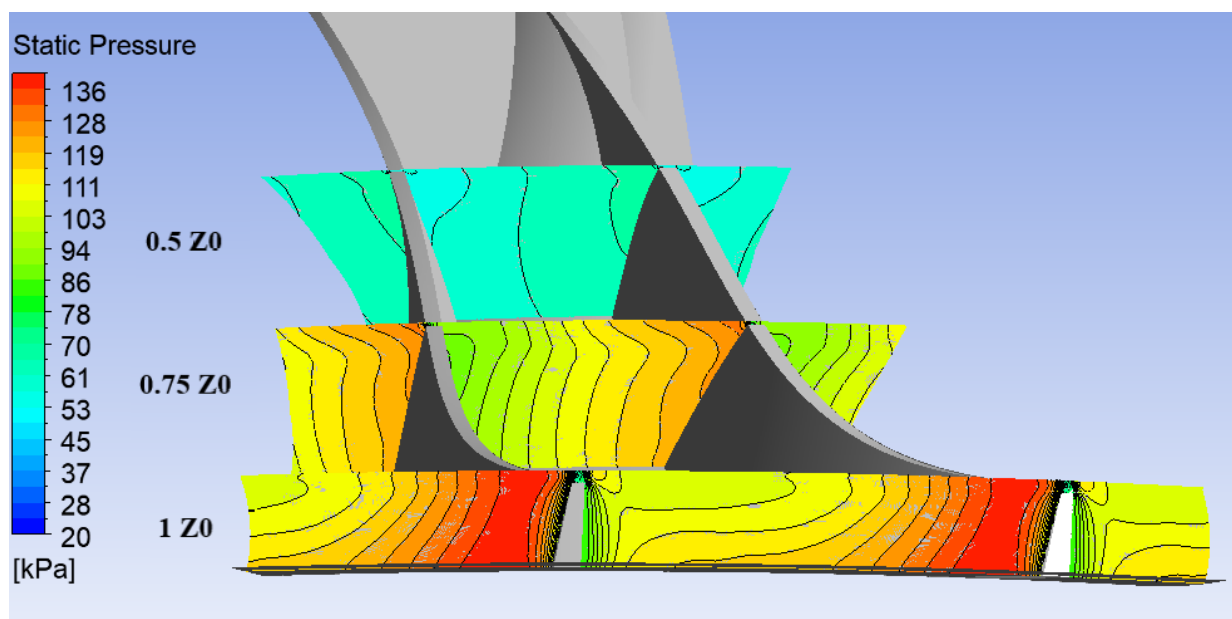


Figure IV.3.B.3. The static pressure field on orthogonal planes.

In the plane at **0.5 Z0**, we observe the creation of a zone of low-pressure value on the SS side compared to the main blades, due to the creation of a vortex zone.

And on the other PS side, the pressure values are higher at the following plane: **0.75 Z0** as well as on the plane at the **Exit of the wheel (1 Z0)**, where the same phenomenon is always created, but the vortex zone decreases more and more until the exit of the wheel.

Therefore, in general in the fluid passage channel of the compressor wheel, a vortex zone is created in the opposite direction to the direction of rotation, which leads to the creation of a low-pressure region in the vicinity of the *SS* side for the main blades as well as for the intercalary blades on the other *PS* side where, the pressure is higher.

1.4. The effect of mass flow variation on the pressure distribution in the compressor blades

Figure IV.3.B.4 represent the distribution of static pressure on the blades and for air flows $\dot{m}=1.15 \text{ Kg/s}$ and $\dot{m}=1.2 \text{ Kg/s}$ at the rotation speed of 28541 rpm in the 50% span plane.

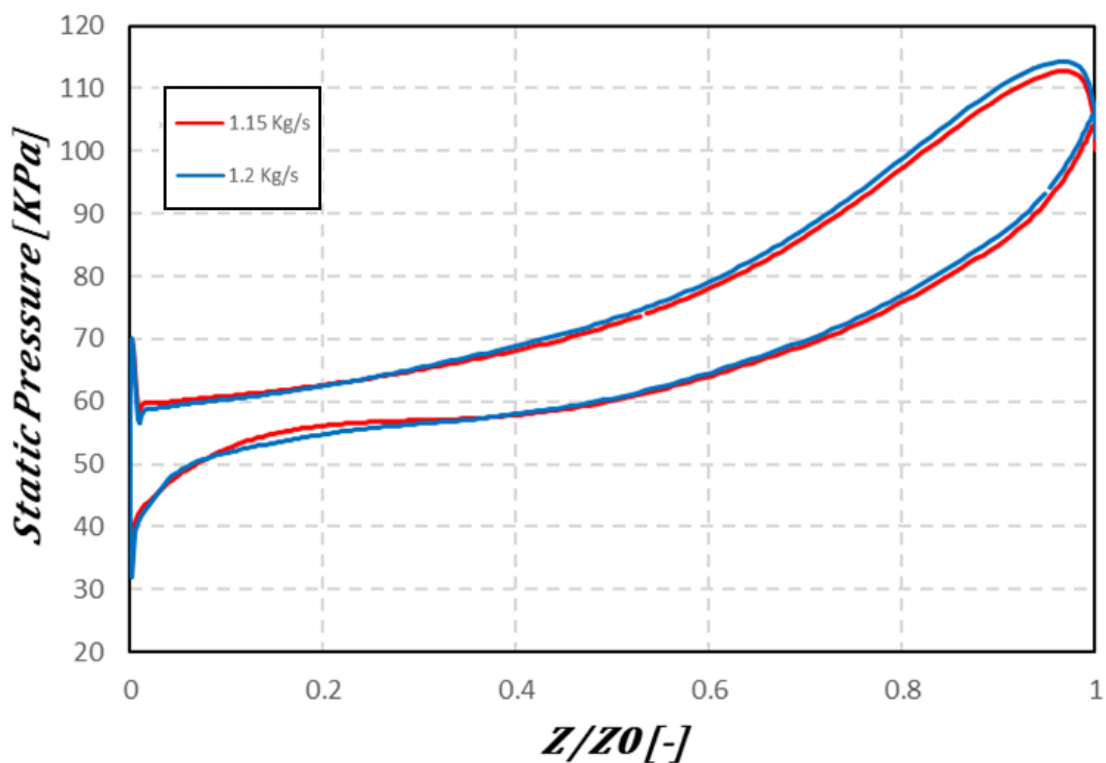


Figure IV.3.B.4. The effect of the variation of air flow on the distribution of static pressure for the blades.

According to this figure, we observe that the profile of static pressure distribution varies slightly depending on the air flow.

In **Figure IV.3.B.4**, for the flow $\dot{m}=1.2 \text{ Kg/s}$, the pressure is higher, the increase in pressure on both sides (intrados and extrados) remains higher when the air flow is at the nominal point compared to the other flow, since the displacement of the operating point of the wheel tends towards the blocking flow of the compressor.

2. The variation of static pressure (SP) and total pressure (TP) in the mobile wheel

Figure IV.3.B.5. represents the variation of total and static pressure in the compressor wheel.

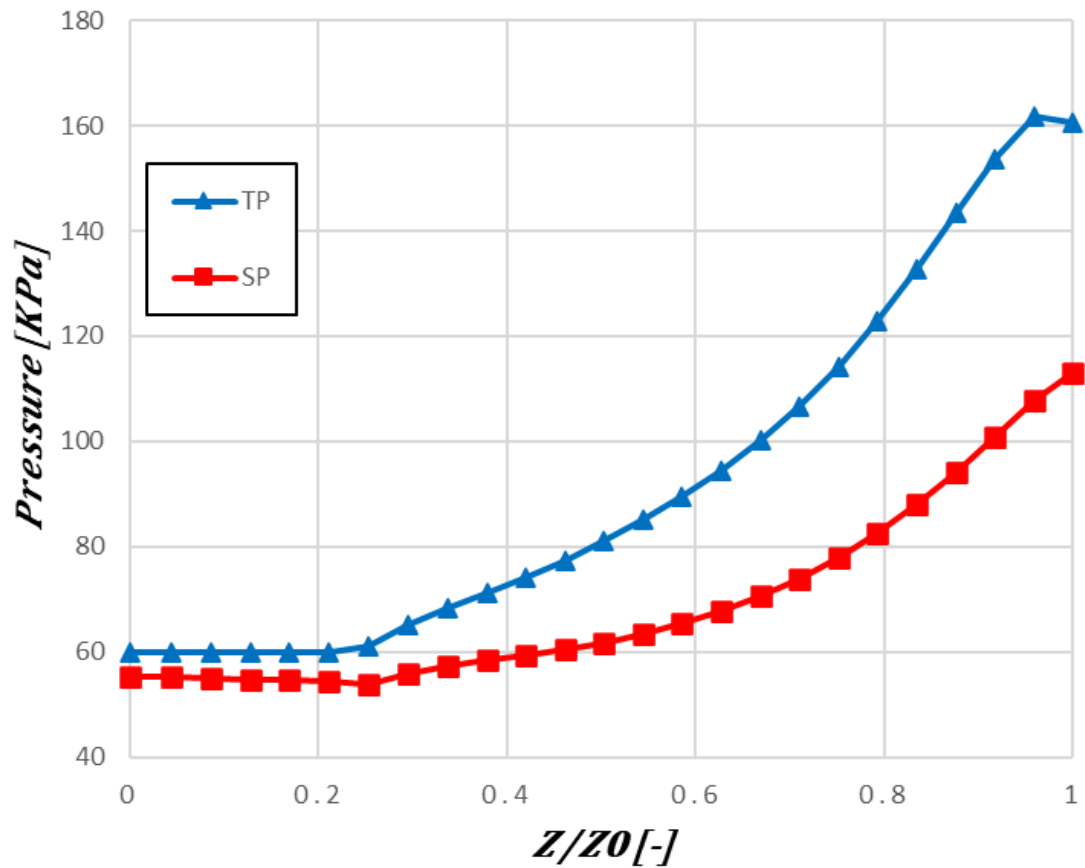


Figure IV.3.B.5. The variation of static and total pressure in the wheel.

It can be divided into two intervals of the rate Z/Z_0 :

1. When $0 < Z/Z_0 < 0.35$: We observe no variation for both pressures (static, total), since in this zone no obstacle can influence the movement of the fluid (work equals zero).
2. When $0.35 < Z/Z_0 < 1$: We observe an increase in total and static pressure up to the exit of the wheel with maximum pressure values, in this zone the energy of the fluid will increase in the form of stop pressure. This increase in total pressure, which is that of stop pressure, will increase the static pressure and the kinetic energy of the fluid.

3. Variation of static temperature (ST) and total temperature (TT) in the mobile wheel

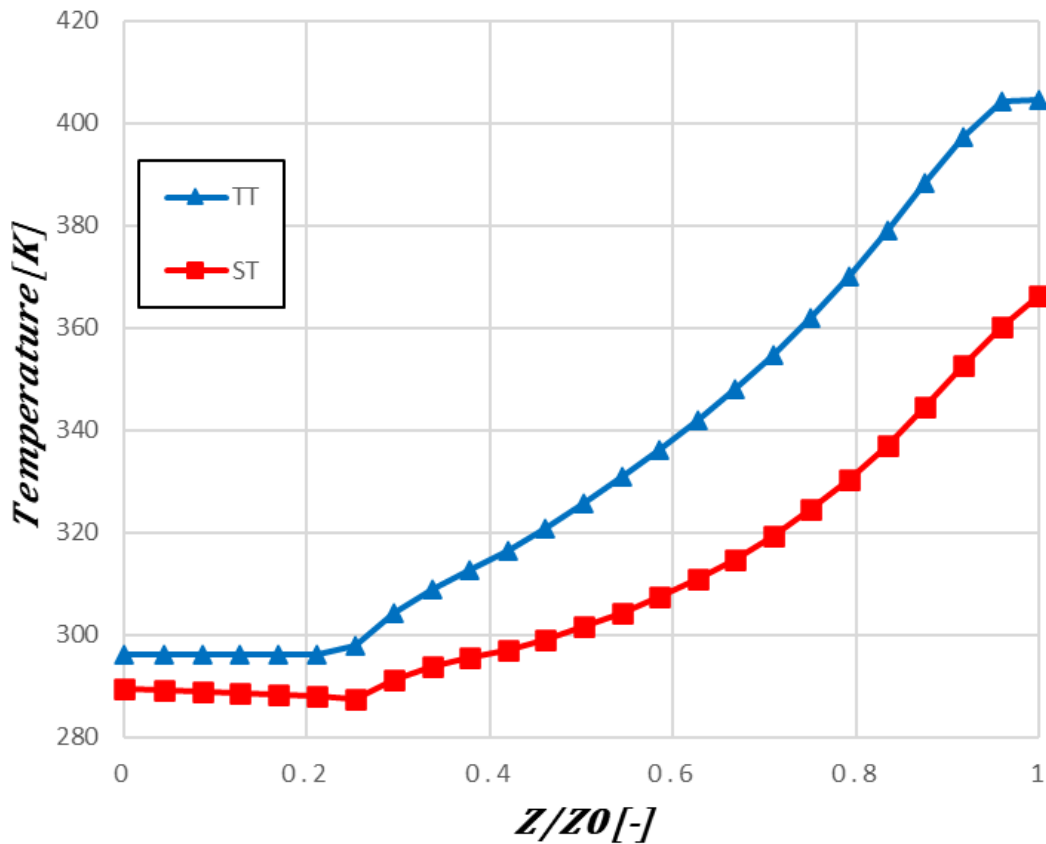


Figure IV.3.B.6. Variation of static and total temperature in the wheel.

The curves given in **Figure IV.3.B.6** can be interpreted in two intervals:

1. When $0 < Z/Z_0 < 0.55$: We observe no variation for both temperatures (static, total), since in this zone no element can have an effect on the movement of the fluid (work equals zero).
2. When $0.55 < Z/Z_0 < 1$: We observe an increase in total and static temperature up to the exit of the wheel with maximum temperature values, in this zone the energy of the fluid will increase in the form of heat. Consequently, this increase in total temperature will increase the static temperature and the kinetic energy of the fluid.

4. Distribution of Mach number

In **Figure IV.3.B.7**, we represent the evolution of the relative Mach number in the meridian plane.

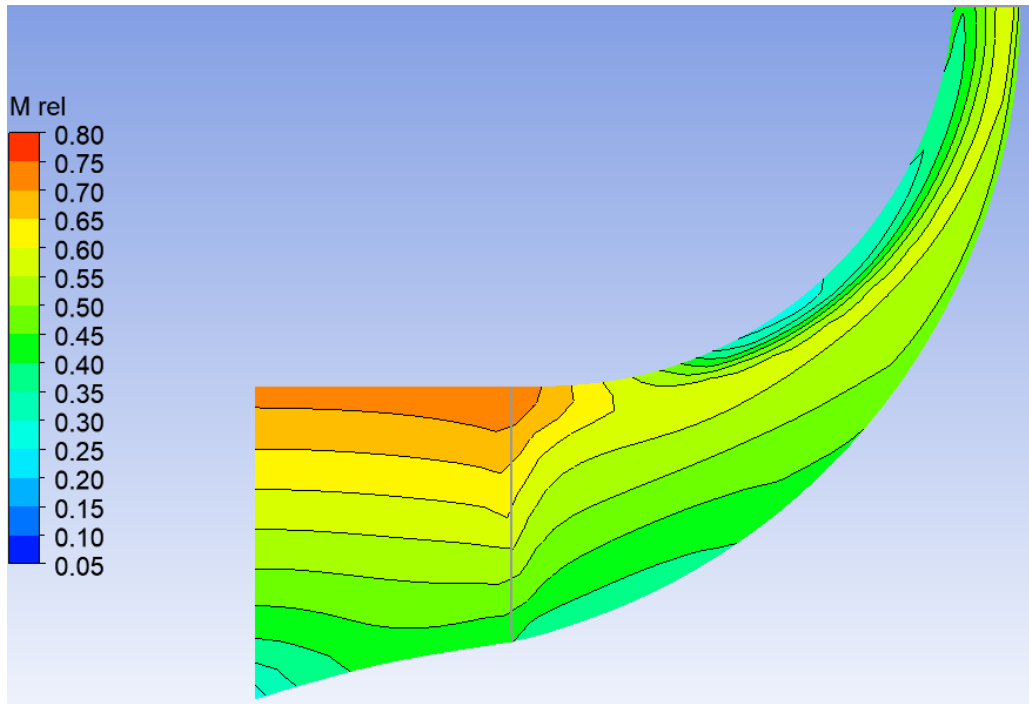


Figure IV.3.B.7. Variation of the relative Mach number in the meridional plane.

From the figure, we notice that zones with low variation of the relative Mach number appear at the entrance of the cone, and at the level of the zone close to the head of the blades in the vicinity of the casing.

On the other hand, the creation of these zones is due to the effect of flow recirculation and the vortex of play.

Then, a slight increase in the relative Mach number on the hub side until it reaches the value **0.55**, due to the increase in tangential speed (influenced by the shape of the blade curvature). On the other hand, it becomes weak and reaches a Mach number equal to **0.30** at the exit of the wheel.

In **Figure IV.3.B.8**, we give the evolution of the relative Mach number in the blade-to-blade plane with respect to the position **50%** to the blade span. We observe, from this figure, that the relative Mach number remains constant until the entrance of the wheel, since no parameter can influence the speed of the flow in the channel.

On the intrados side with respect to the main and intercalary blades, the fluid flow accelerates slightly then it becomes weak at the exit of the wheel, this is due to the curvature of the surface of these blades (decrease in the tangential speed of the flow).

On the other hand, on the extrados side, the flow of the fluid flow decelerates until the creation of zones of low values of the relative Mach number, since a phenomenon of detachment and recirculation of the fluid is created (this influences the tangential speed of the flow) and also the effect of the direction of rotation of the wheel.

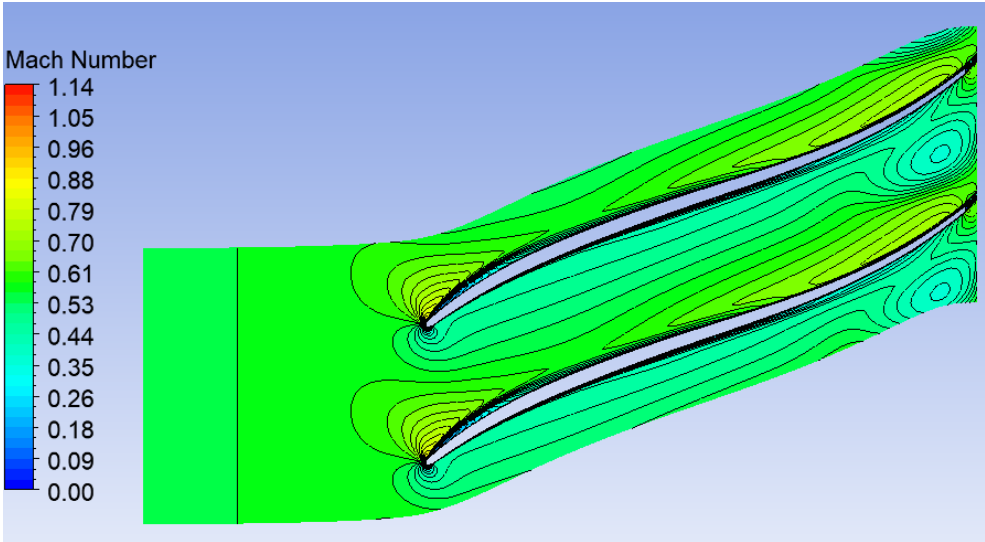


Figure IV.3.B.8. Variation of the relative Mach number in the blade-to-blade plane.

5. The effect of blade curvature and their rotation on the turbulent boundary layer

From the study conducted by Moore [29] on the boundary layer and under the combined effect of curvature and wheel rotation, the author a blade-to-blade plane in order to predict the effect of rotation and curvature on turbulence.

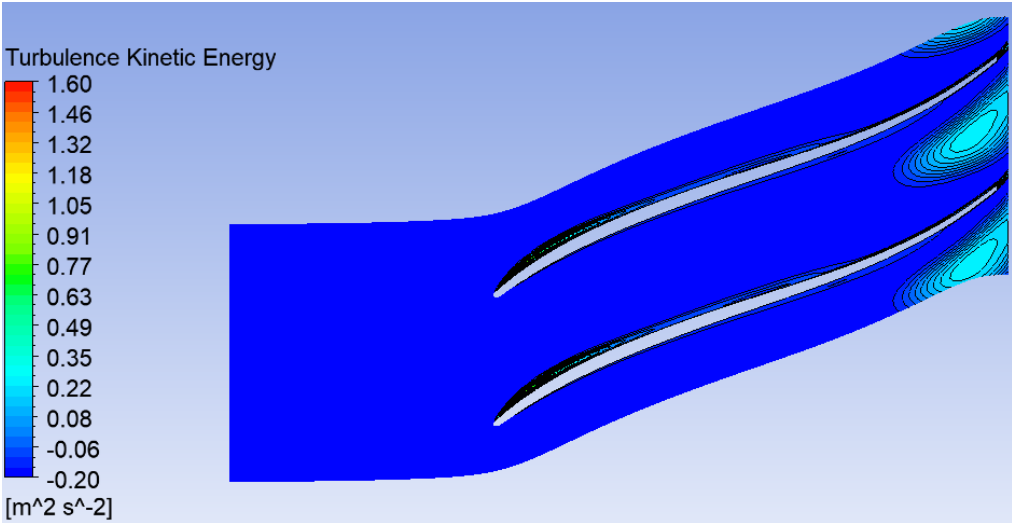


Figure IV.3.B.9. Variation of turbulence energy.

6. Entropy (S)

6.1. The variation of entropy (S) in the blade-to-blade planes

Figures **IV.3.B.10**, **IV.3.B.11** and **IV.3.B.12** below represent the variation of entropy in the blade-to-blade planes relative to the positions **20%**, **50%** and **80%** of the span.

From these figures, we observe large zones of entropy energy on the extrados side of the main and intercalary blades.

For figures **IV.3.B.10** and **IV.3.B.11**, the entropy values on the extrados side are higher, as there is creation of detachment and recirculation zones of the flow.

In addition, in the 80% plane, the entropy values are larger compared to the other planes, as the interaction of the flow between the wheel and the casing is more significant and creates detachment zones.

Entropy represents the energy losses in the mobile wheel.

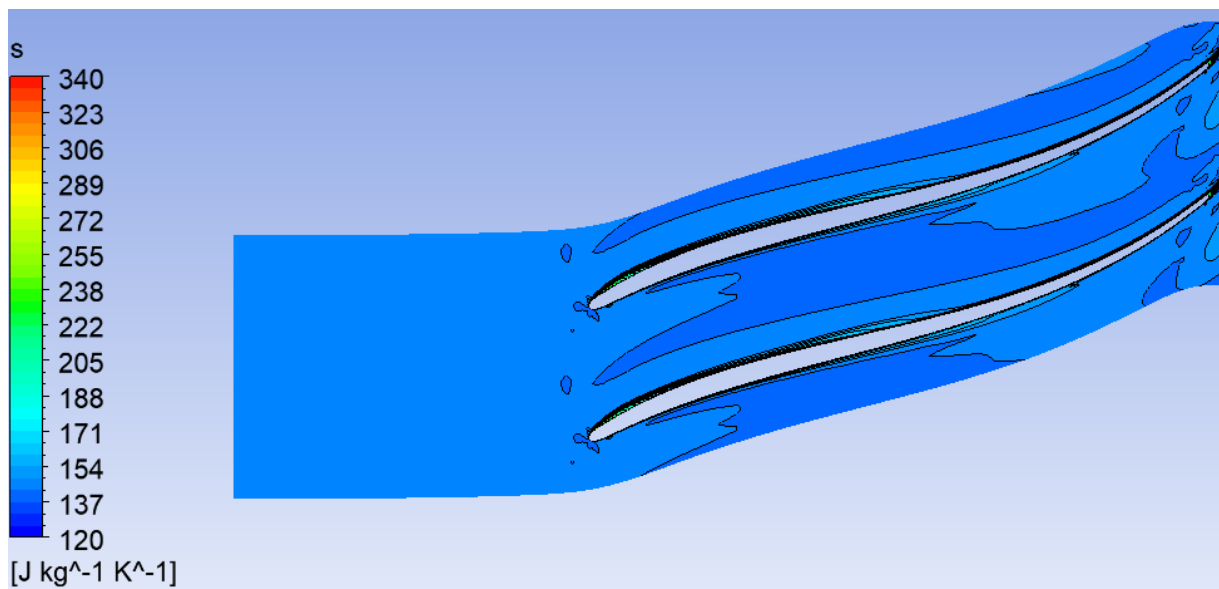


Figure IV.3.B.10. The variation of entropy in the blade-to-blade plane relative to the 20% span plane.

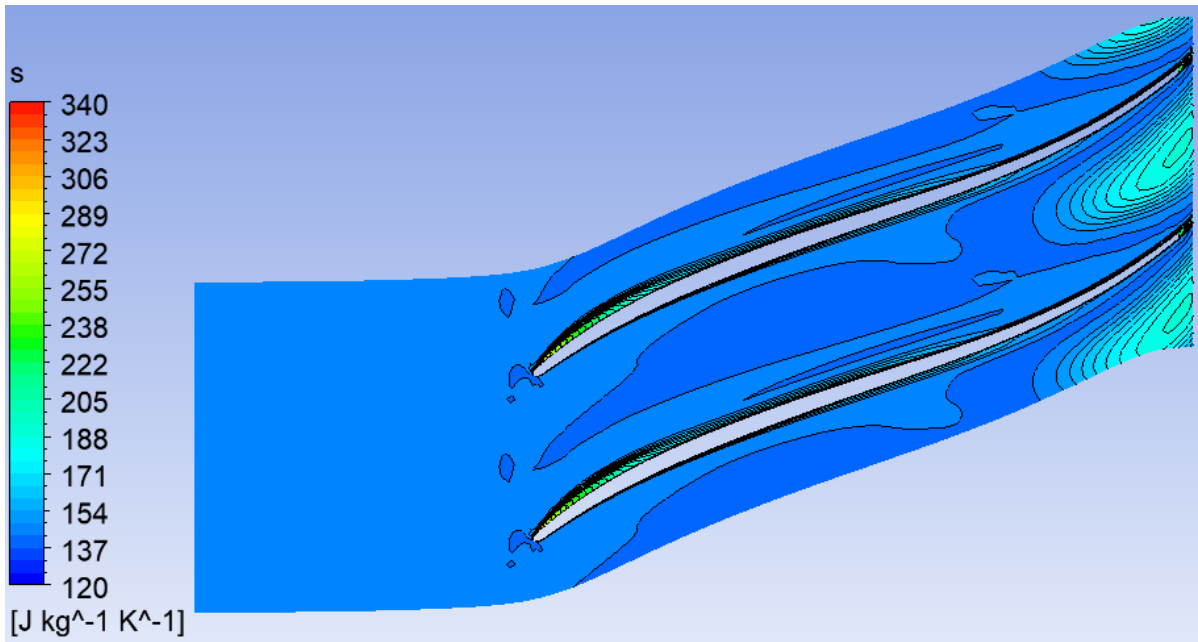


Figure IV.3.B.11. The variation of entropy in the blade-to-blade plane relative to the 50% span plane.

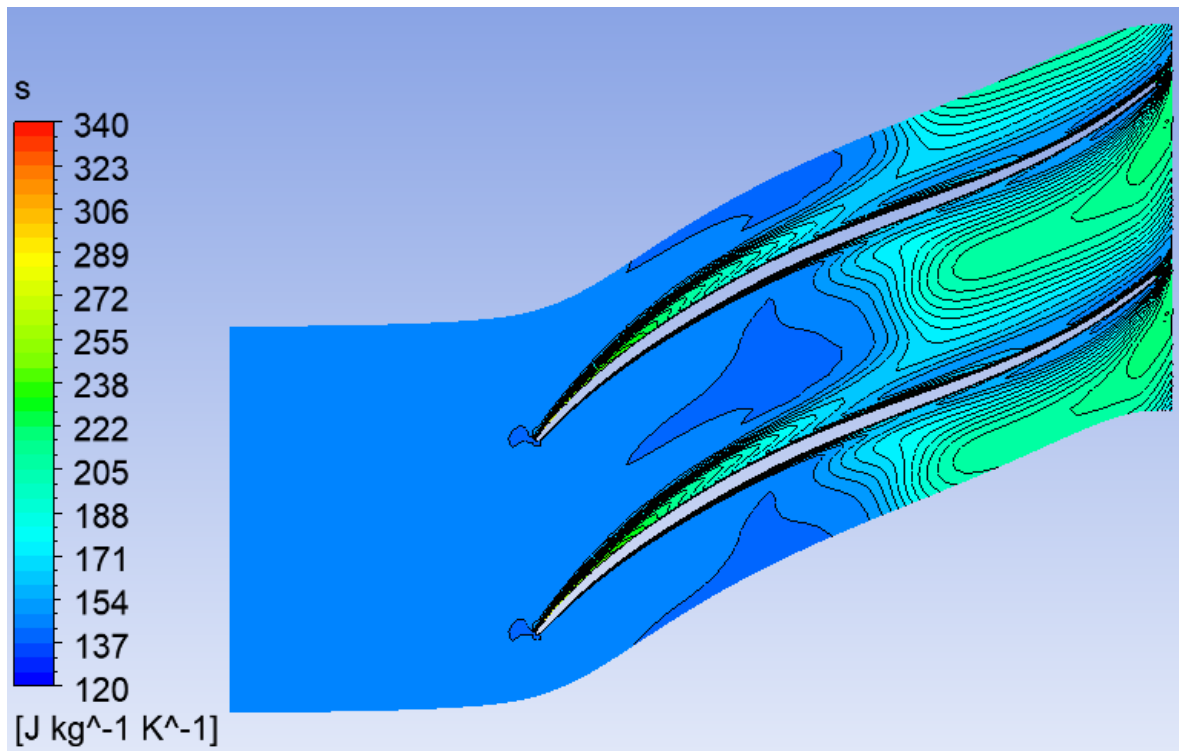


Figure IV.3.B.12. The variation of entropy in the blade-to-blade plane relative to the 80% span plane.

6.2. The variation of entropy in the orthogonal plane

Figure IV.3.B.13 represents the variation of entropy in the orthogonal plane at the wheel outlet, we notice from this figure that at the wheel outlet the entropy becomes higher on the extrados side, but also low on the intrados side of the same blade.

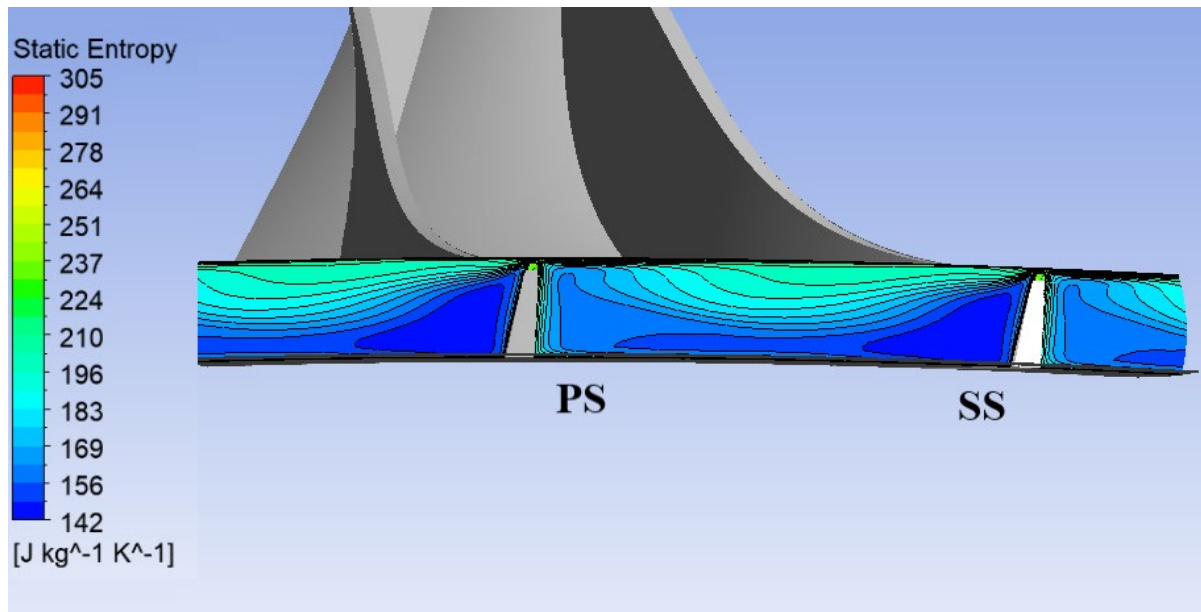


Figure IV.3.B.13. The variation of entropy in the orthogonal plane at the wheel outlet.

b) *The diffuser*

1. Total and static pressures in the diffuser

They are defined in three planes: the meridian plane, the blade-to-blade plane, and the orthogonal plane.

1.1. Total and static pressure fields in the meridian plane

From **Figure IV.3.B.14**, we notice a slight increase in static pressure as well as a decrease in total pressure, such as at the diffuser level the flow slows down due to the divergent shape of the passage section and the effects of losses.

This slowdown also allows to convert part of the kinetic energy of the fluid into an increase in static pressure.

The decrease in the total pressure field is due to the increase in loss effects.

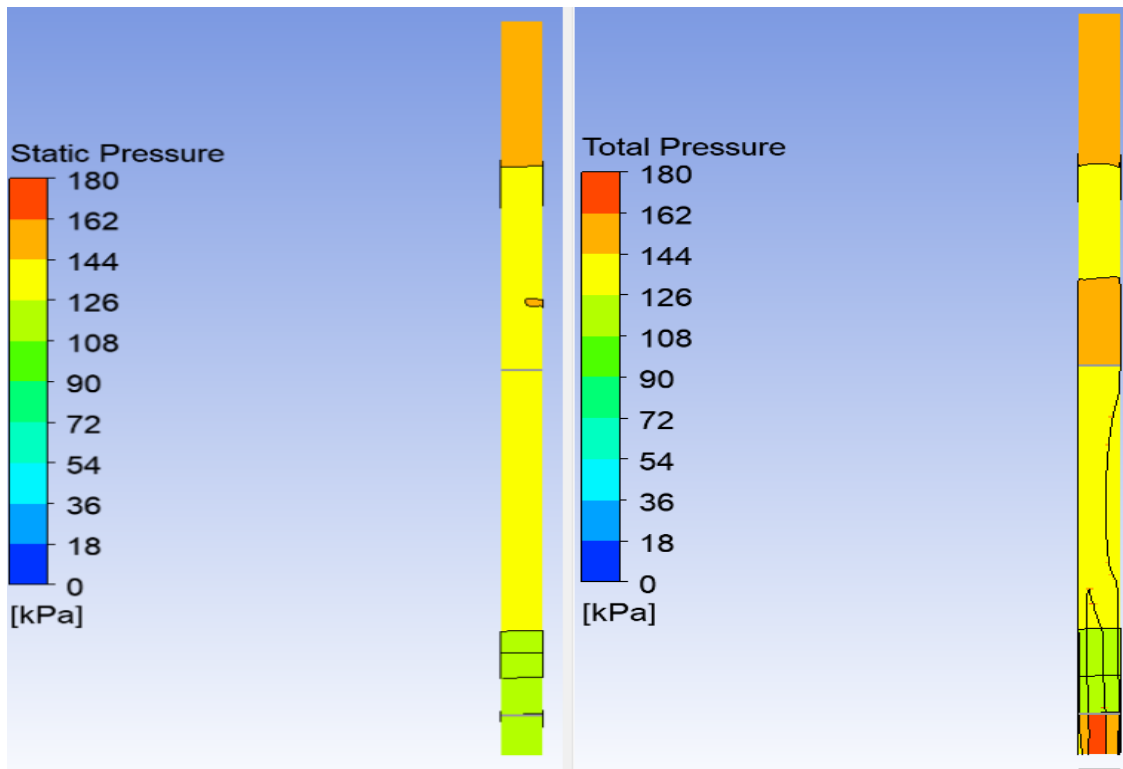


Figure IV.3.B.14. Static (SP) and total (TP) pressure fields.

1.2. Pressure field in the blade-to-blade plane

In this plane, we study the analysis of the evolution of the static and total pressure fields.

1.2.1. Total pressure field

Figure **IV.3.B.15** represents the evolution of the total pressure field in the blade-to-blade plane at 50% relative to the span height.

The figure shows a decrease in total pressure due to the effects of losses in the flow passage section. On the intrados side (*PS*), there are areas of low total pressure compared to that of the extrados side (*SS*) at the radial part of the diffuser, since on the side (*PS*) the effects of losses (vortex, flow recirculation) are considerable compared to the side (*SS*).

On the extrados side (*SS*), we noticed a decrease in total pressure in the radial part of the diffuser, then a rapid decrease in pressure on both sides because, the losses are higher.

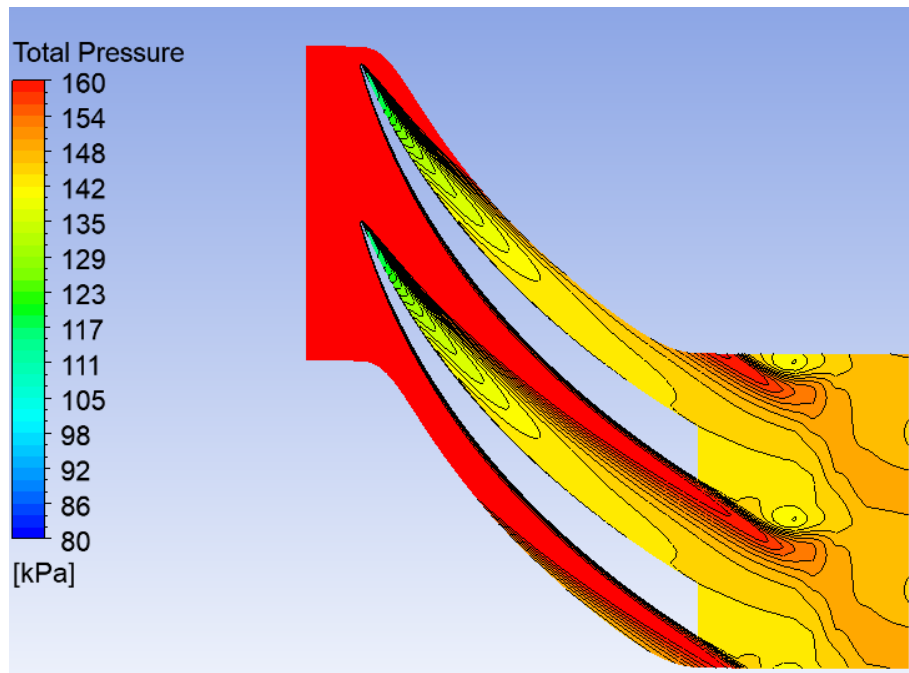


Figure IV.3.B.15. Total pressure field in the blade-to-blade plane relative to the span height at 50%.

1.2.2. Static pressure field

Figure IV.3.B.16 represents the evolution of the static pressure field in the blade-to-blade plane at 50% relative to the span height.

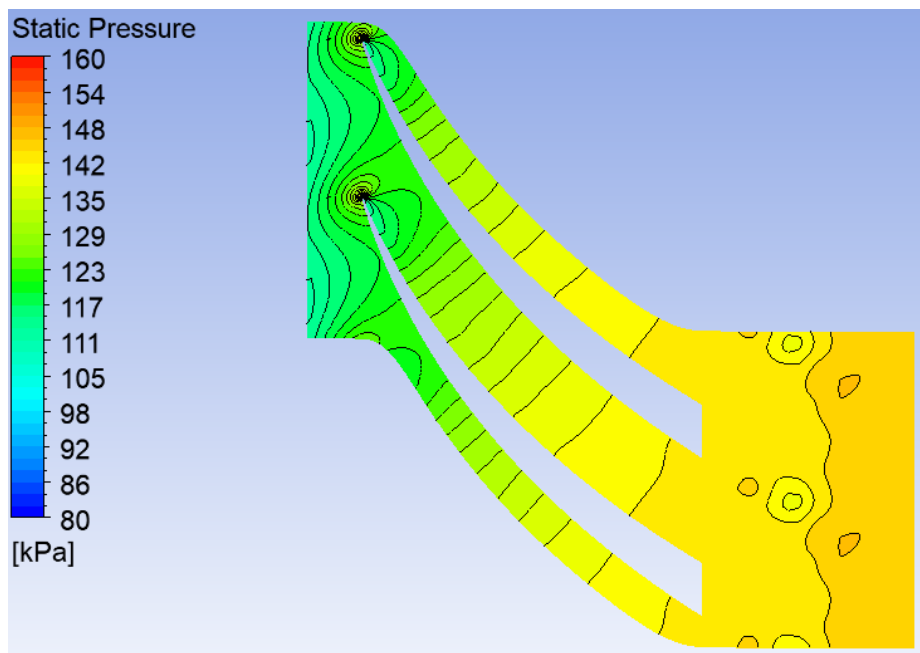


Figure IV.3.B.16. Static pressure field relative to the span height at 50%.

From the figure, we notice an increase in static pressure in the diffuser. In addition, the distribution of the static pressure field on the extrados side (*SS*) is higher compared to the intrados side (*PS*) and near the leading edge the pressure field is maximum (stagnation point), and this is due to the effects of energy losses, the angle of incidence of the flow as well as the geometric shape of the passage section.

1.3. Total pressure field in the orthogonal plane

Figure IV.3.B.17 represents the evolution of the total pressure field in the orthogonal plane at the diffuser.

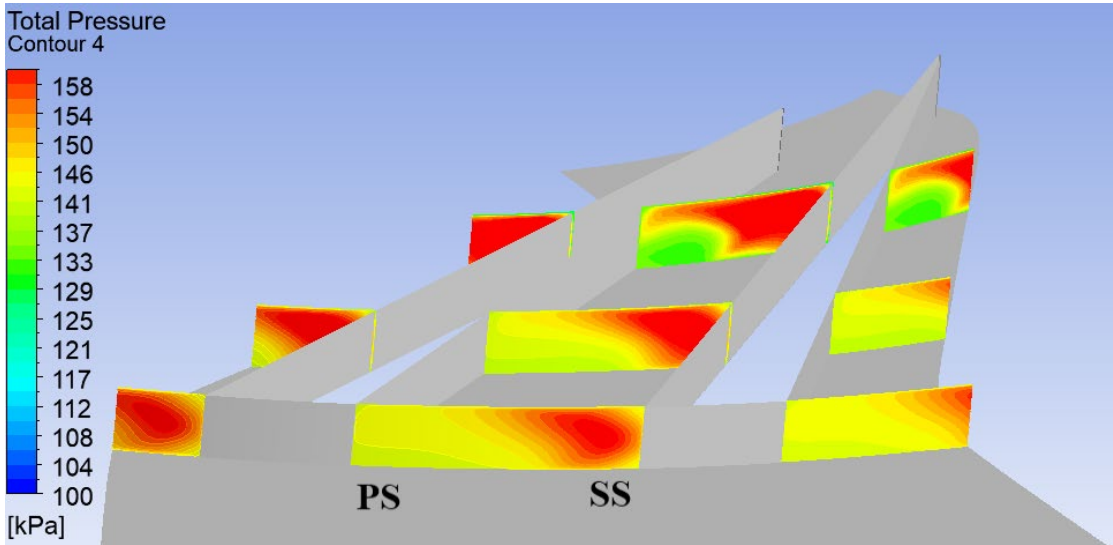


Figure IV.3.B.17. Total pressure fields at the diffuser.

From the figure, we can note the presence of a large pressure zone which takes minimum values at the diffuser outlet which, it is very close to the side (*SS*), since there is creation of phenomena of detachment and recirculation of the fluid. Therefore, these favor the increase in losses, which results in a decrease in total pressure.

1.4. Distribution of static pressure on the blades

Figure IV.3.B.18 represents the distribution of static pressure on the diffuser blade at 50% relative to the span height.

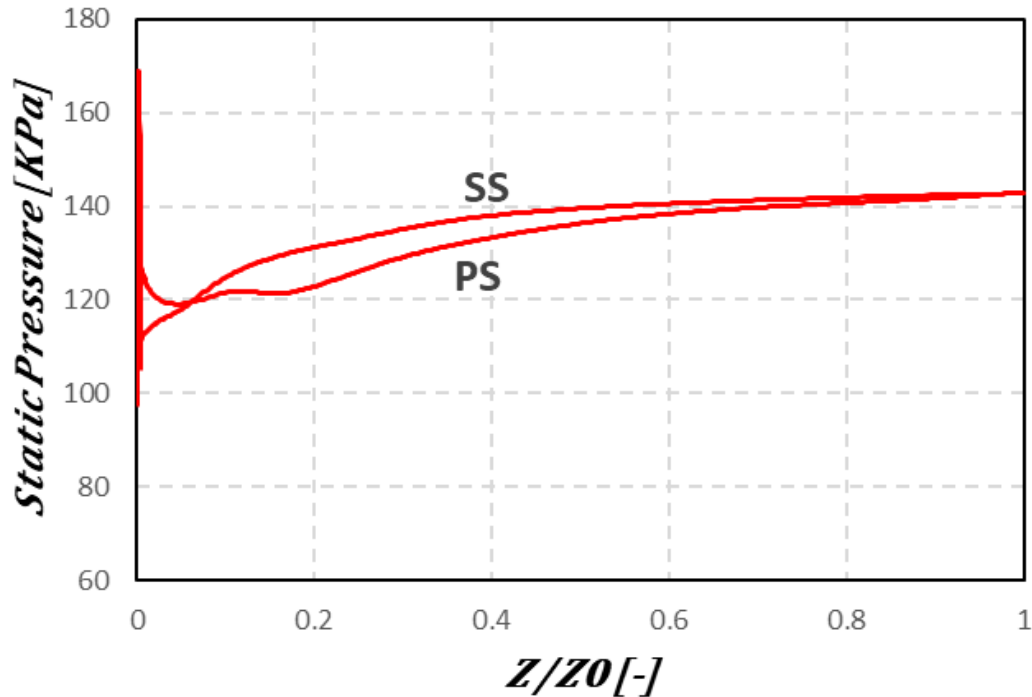


Figure IV.3.B.18. Distribution of static pressure.

The figure above shows an increase in pressure on the extrados side (**SS**) of the diffuser to reach maximum values at the leading edge, then it decreases.

On the intrados side (**PS**), the pressure is minimal at the leading edge and will then increase, to reach an almost constant value.

In the axial part of the diffuser, we do not notice any pressure difference on both sides (**PS** and **SS**).

Because the effects of losses, the fluid passage section and the aerodynamic shape of the blades have an influence on the pressure distribution.

1.5. Variation of total and static pressures in the diffuser

Figure **IV.3.B.19** represents the variation of total and static pressure in the diffuser.

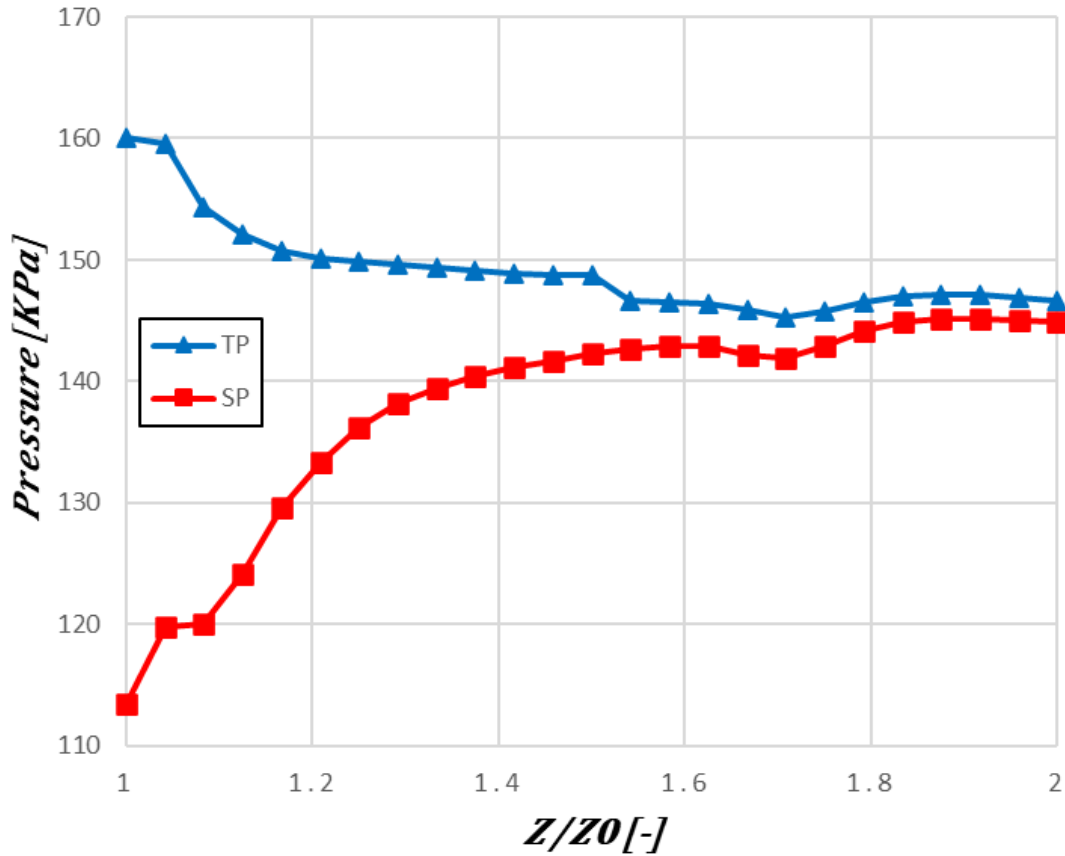


Figure IV.3.B.19. Variation of total and static pressure in the diffuser.

From the curve of the figure, we notice a decrease in total pressure in the diffuser, due to the effects of losses.

In addition, we notice an increase in static pressure up to the diffuser outlet, due to the passage section of the fluid flow (divergent section).

2. Entropy field in the blade-to-blade plane

Figure IV.3.B.20 represents the variation of the field in the blade-to-blade plane at 50% relative to the span height. From this figure, we notice that the entropy field is maximal on the intrados side (*PS*) corresponding to maximum energy losses, but also a maximum loss at the trailing edge. On the other hand, on the extrados side (*SS*), there is creation of vortex and recirculation zones.

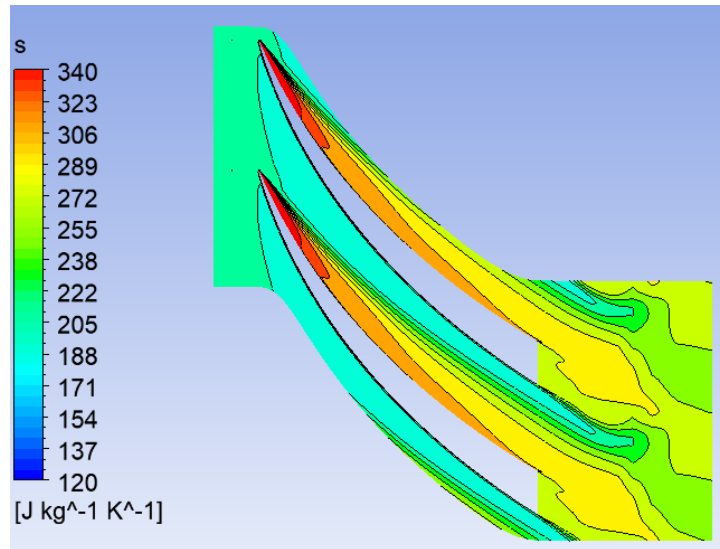


Figure IV.3.B.20. Entropy field in the blade-to-blade plane at 50% relative to the span height.

c) The compressor stage

1. Variation of the total pressure TP in the compressor stage

Figure IV.3.B.21 represents the variation of the total pressure in the meridian plane.

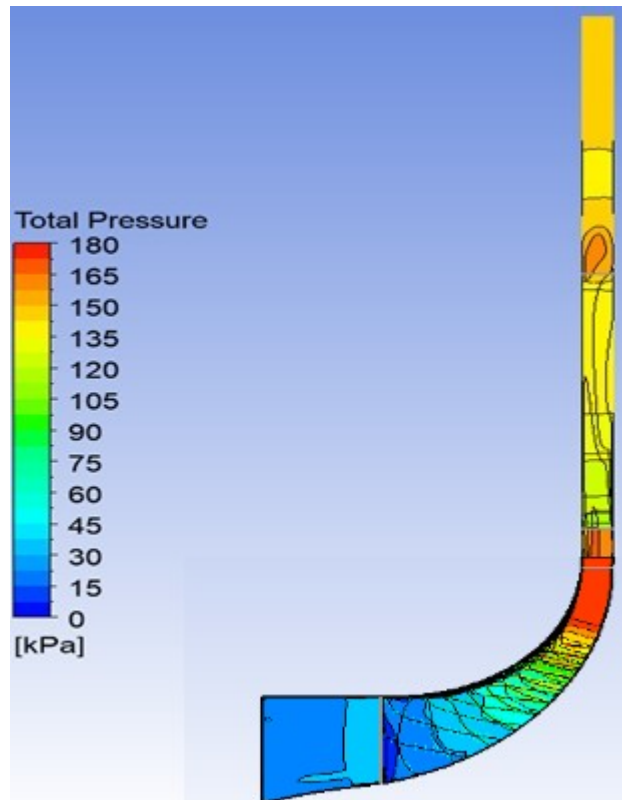


Figure IV.3.B.21. Variation of the total pressure field P_t in the compressor stage.

From the figure, we notice an increase in the total pressure field in the mobile wheel and a decrease in the field in the diffuser.

In the *mobile wheel* of the compressor the fluid energy increases part of which leads to an increase in total pressure.

In the *diffuser* the total pressure field decreases as losses increase, and at the interface, we notice a rapid increase in total pressure up to a maximum value reached due to the effect of interaction and compressibility of the flow.

Figure IV.3.B.22 represents the variation of the total pressure in the centrifugal compressor stage relative to the mean line.

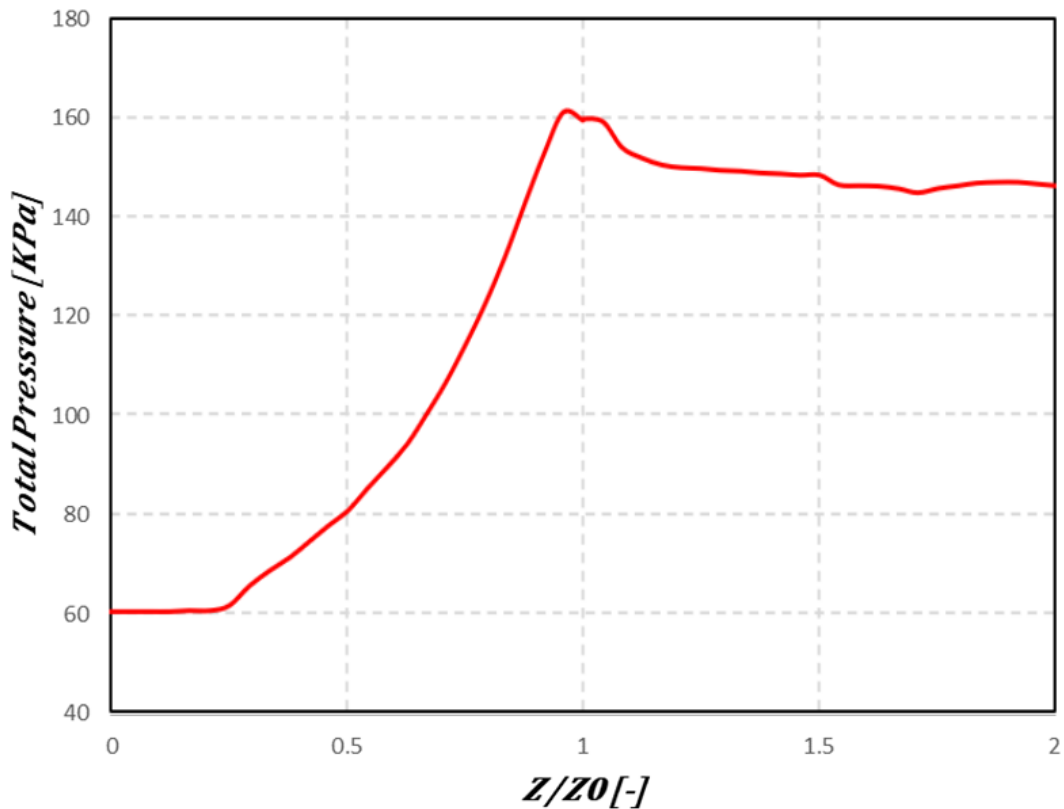


Figure IV.3.B.22. Variation of the total pressure P_t in the compressor stage.

From the figure, we notice an increase in total pressure in the mobile wheel which is due to the fluid energy where part of this energy causes an increase in total pressure, then in the diffuser a decrease in pressure due to the effects of significant losses, in addition at the interface the losses are maximum.

2. Variation of the static pressure SP in the compressor stage

Figure IV.3.B.23 represents the variation of the static pressure field in the centrifugal compressor stage relative to the meridian plane.

We notice, from the figure bellow an increase in static pressure and this, according to the analysis of the pressure field in the mobile wheel and in the diffuser.

From the theoretical analysis, in the mobile wheel the fluid energy causes an increase in total pressure, this increase is shared in a static pressure, on one side and on another, side in fluid kinetic energy.

Therefore, at the outlet of the mobile wheel the kinetic energy is higher, the diffuser will decrease the flow speed of the fluid due to the effects of losses in the fluid passage channel, this slowdown allows in addition the conversion of part of the kinetic energy into static pressure.

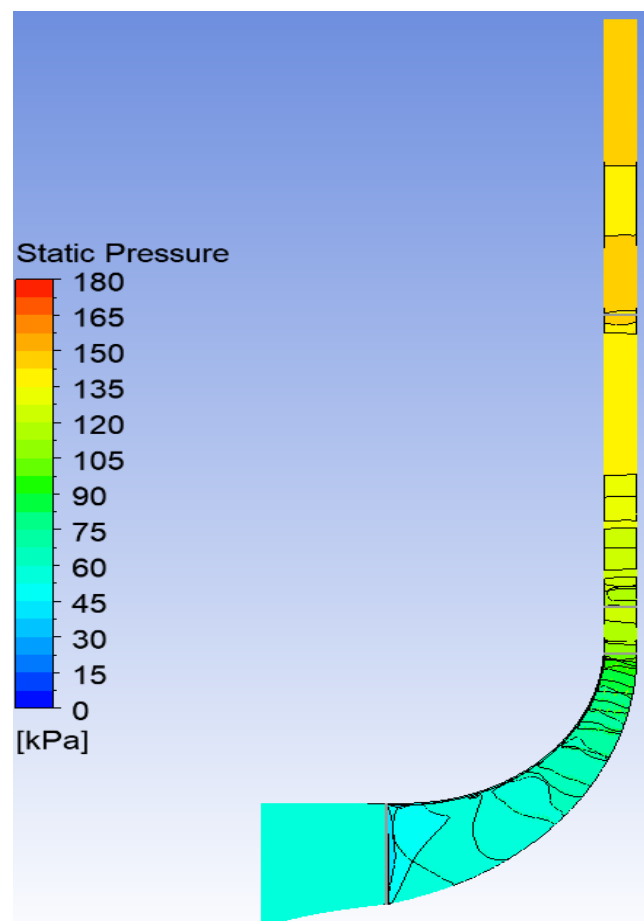


Figure IV.3.B.23. Variation of the static pressure field PS in the compressor stage.

Figure IV.3.B.24 represents the variation of the static pressure in the centrifugal compressor stage relative to the mean line.

We notice from the curve of this figure an increase in static pressure in the centrifugal compressor stage in general. From the previous analysis, in the mobile wheel, the total pressure of the fluid decomposes, in static pressure on one side, and on another side in a kinetic energy. In the diffuser, the kinetic energy is converted into static pressure. So, static pressure increases in the diffuser and a decrease in the kinetic energy of the fluid, due to the passage section and the effects of losses.

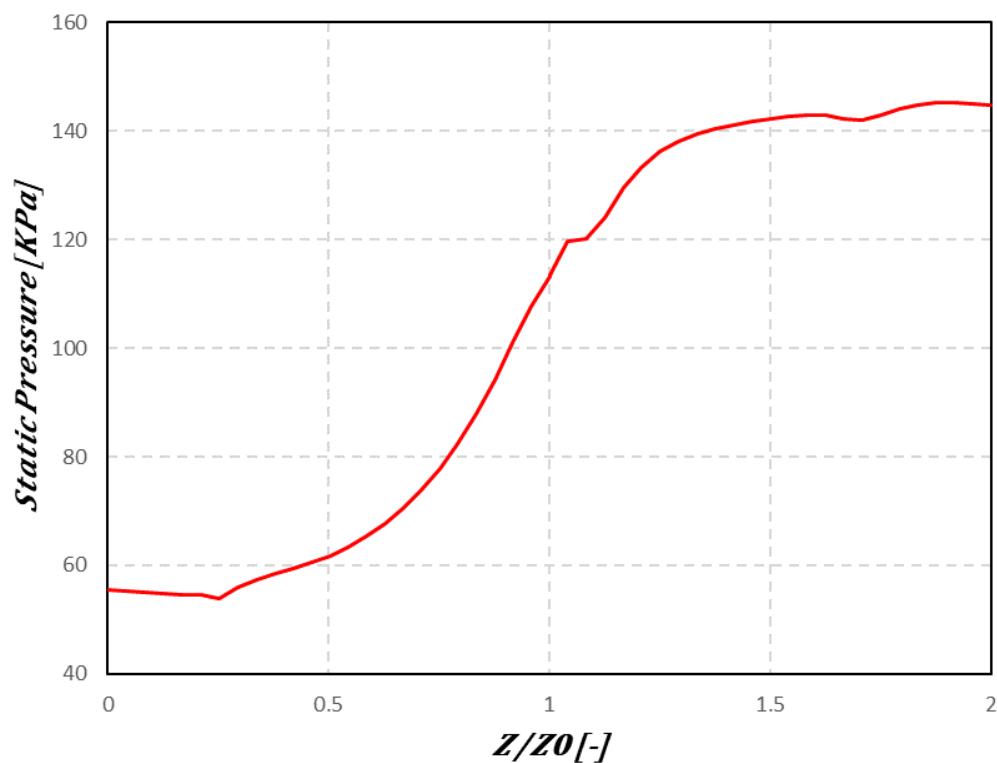


Figure IV.3.B.24. Variation of the static pressure PS in the compressor stage.

3. Variation of the relative Mach number field in the compressor stage

Figure IV.3.B.25 represents the variation of the relative Mach number field in the centrifugal compressor stage relative to the meridian plane.

From this figure, the relative Mach number field decreases in the mobile wheel due to the geometric shape of the blades and the effect of the rotation speed.

In the diffuser, a decrease in the field to minimum values, because the angle of incidence of the flow and the viscosity in the passage section influence the field.

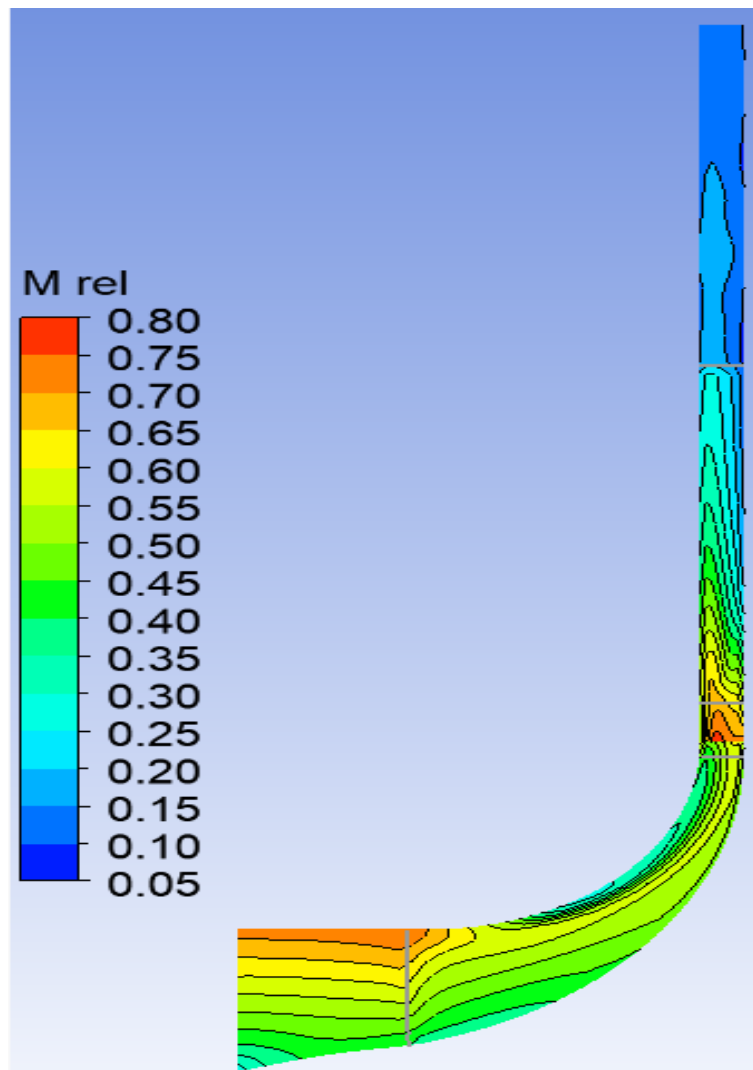


Figure IV.3.B.25. Variation of the relative Mach number field in the compressor stage.

At the interface, a maximum increase in the relative Mach number, due to the effect of the flow interaction and the creation of the jet phenomenon at the outlet of the mobile wheel where the fluid speed is maximum.

From the curve of **Figure IV.3.B.26**, we notice:

- In the interval 0 to 0.5 of the ratio Z/Z_0 , a slight increase in the relative Mach number, due to the geometric shape in the suction channel as well as the convergent passage section.

- In the interval 0.5 to 1 of the ratio Z/Z_0 , the relative Mach number becomes weak due to the effect of the curvature of the blades.
- At the interface, we notice a rapid increase in the relative Mach number up to a maximum value equal to **0.71**, because there is the effect of interaction and compressibility of the flow (jet phenomenon at the outlet of the mobile wheel).
- In the diffuser, the relative Mach number decreases due to the effects of the fluid flow losses.

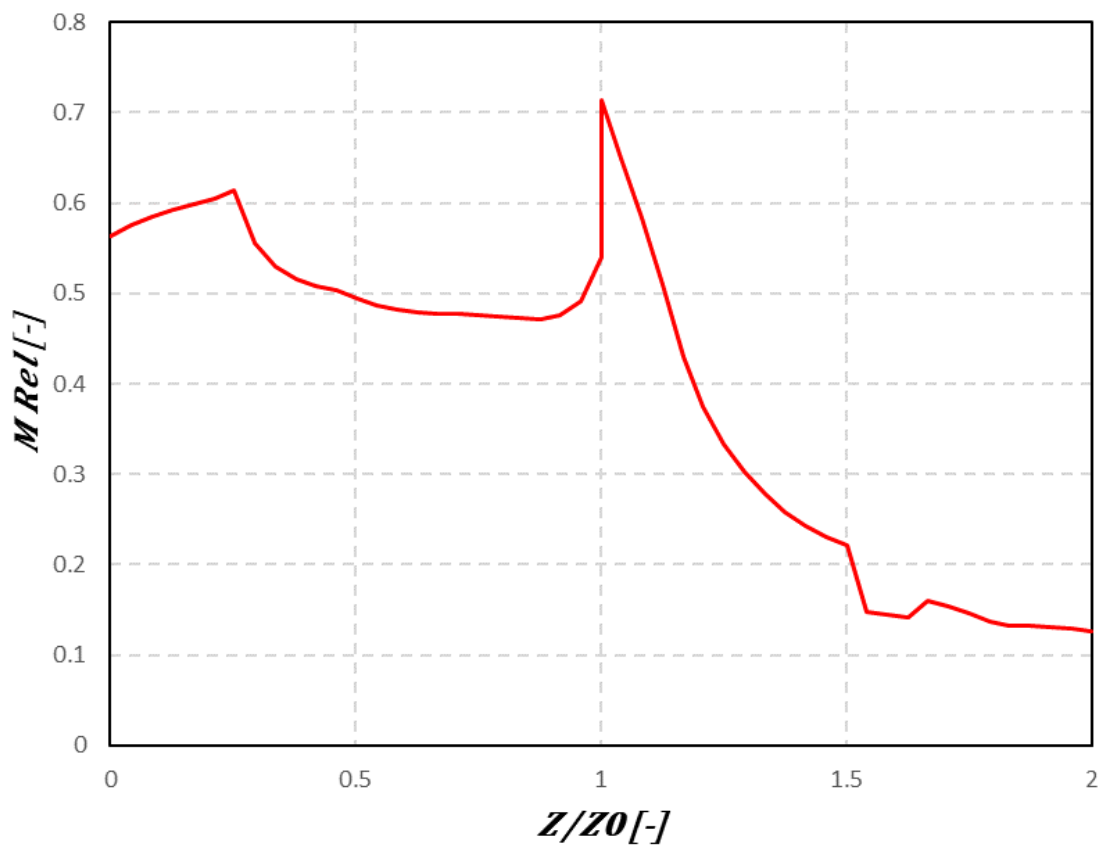


Figure IV.3.B.26. Variation of the relative Mach number in the compressor stage.

Figure IV.3.B.27., represents the variation of the relative Mach number field in the centrifugal compressor stage at the interface and in the blade-to-blade plane relative to the span height at 50%.

Presentation of the variation of relative Mach number in the centrifugal compressor stage at the interface between the mobile wheel and the diffuser.

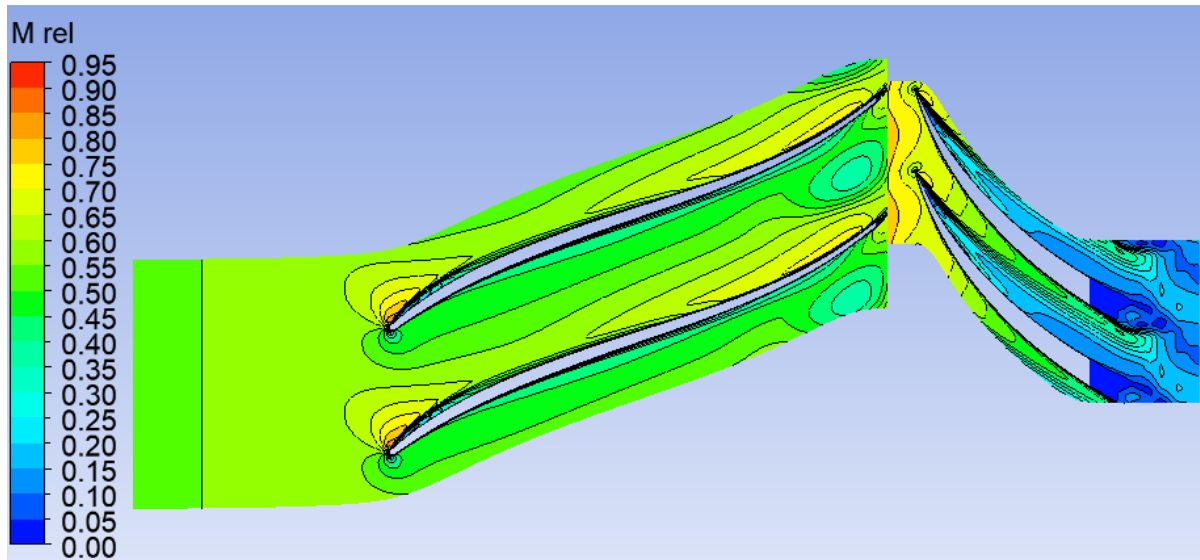


Figure IV.3. B.27. Relative Mach number field in the centrifugal compressor stage at the interface and relative to the span height at 50%.

From the figure, the area where the relative Mach number field is maximum at the interface which reaches the value 0.85 , is due to the effect of interaction and compressibility of the fluid flow.

In the mobile wheel, we notice that the Mach number field decreases due to the effect of blade curvature and the shape of the flow passage section.

In the diffuser, the areas where the relative Mach number field is weak on the intrados side (PS), are due to several phenomena that influence these areas and which will increase up to the outlet of the diffuser, on the other hand on the extrados side (SS) a decrease in the relative Mach number, because there is creation of loss effects.

4. Variation of the turbulence kinetic energy “K”

Figure **IV.3.B.28** represents the variation of the turbulence kinetic energy field in the centrifugal compressor stage relative to the meridian plane.

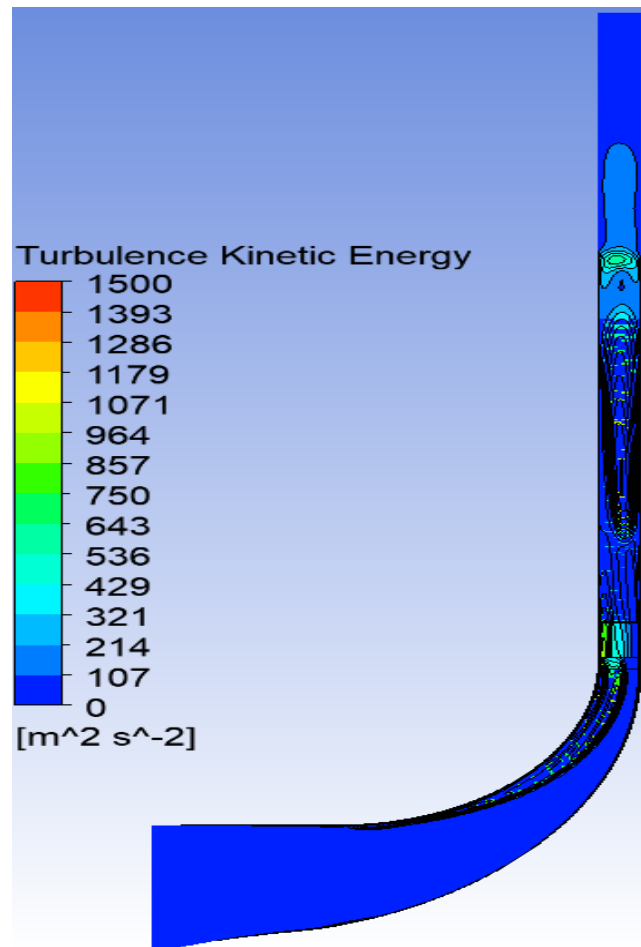


Figure IV.3.B.28. Turbulence energy field in the compressor stage.

From the figure above, we can note that the turbulence kinetic energy increases in the mobile wheel at the head of the leading edge of the blade, this depends on the angle of incidence of the flow, the interaction of the boundary layer between the casing and the end of the blade head, the phenomenon of flow recirculation and the rotation speed, as well as the interaction between the secondary flow and the main flow.

At the interface, the turbulence kinetic energy reaches maximum values, due to the interaction of the flow between the mobile wheel and the diffuser (creation at the outlet of the mobile wheel of wake and jet phenomena) and also, the shock of the fluid flow at the leading edge of the diffuser blades.

In the diffuser, a decrease in the turbulence kinetic energy field due to the effects of less significant losses.

Figure IV.3.B.29 represents the variation of the turbulence kinetic energy in the centrifugal compressor stage relative to the mean line.

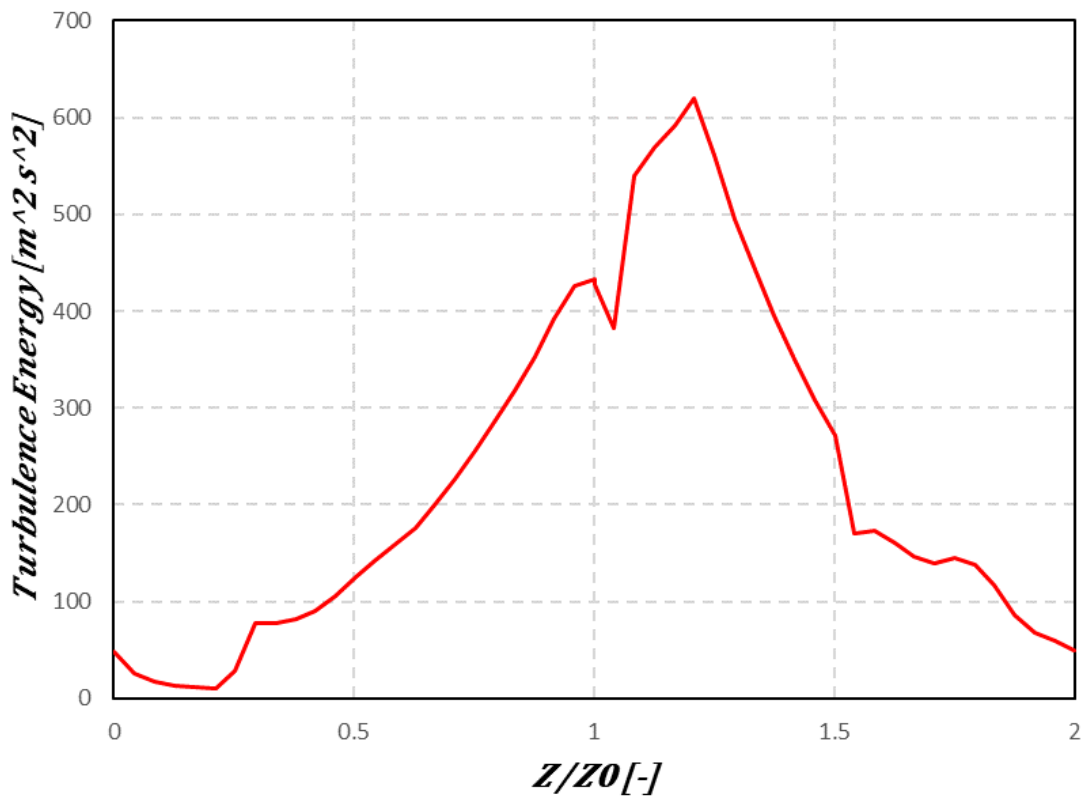


Figure IV.3.B.29. The variation of turbulence energy in the compressor stage.

From the figure, an increase in the turbulence kinetic energy in the mobile wheel until reaching the maximum value at the outlet of the wheel, due to the elevation of the effects of losses.

In the diffuser we have a decrease in the turbulence kinetic energy where the effects of losses are weak.

5. (T,S) Diagram of the centrifugal compressor stage

Figure IV.3.B.30 represents the diagram of temperature as a function of entropy for the stage of the centrifugal compressor for the diffuser.

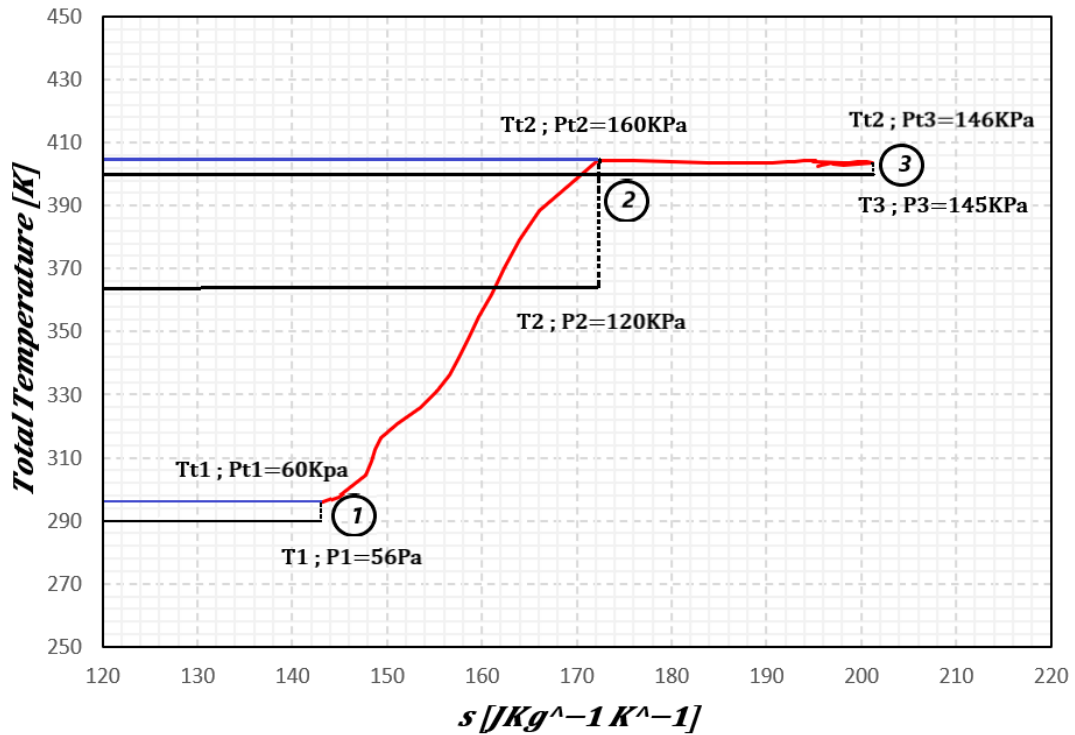


Figure IV.3.B.30. Diagram of temperature as a function of entropy (T.S) of the centrifugal compressor stage.

From the (T,S) diagram of **Figure IV.3.B.30**, we can note the main role of the impeller and the diffuser, an increase in the fluid energy in the wheel of the centrifugal compressor in the form of total pressure and a quantity of heat, such that the increase in total pressure decomposes into static pressure from $P1=56[KPa]$ up to $P2=120[KPa]$; and also, an increase in the kinetic energy of the fluid.

In the diffuser, the mechanical work is zero because the temperature at the entrance is equal to that at the exit ($Tt2=Tt3$) with the decrease in total pressure due to the effects of losses in the fluid passage section, such that the transformation of the fluid energy in the diffuser transforms into an increase in static pressure to the value $P3=145[KPa]$ and a decrease in kinetic energy.

This (T,S) diagram is consistent with the theoretical analysis carried out on the stage of the centrifugal compressor. Therefore, we can validate the results obtained by qualitatively comparing with this diagram and the one given in **Chapter I**. In addition, the same applies to the variations of total and static pressures as well as total and static temperatures.

CONCLUSION

In conclusion, the assessment of turbulence model predictions for centrifugal compressor simulation has provided valuable insights into the complexities and challenges inherent in compressor technology. Through meticulous examination and analysis, this study has deepened our understanding of compressor dynamics and performance prediction methodologies.

Significant differences were observed in the local flow field predictions, particularly at the near-surge operating point (P). The **S-A** model exhibited poor prediction of local flow structures, while the **SST-CC** model demonstrated improved accuracy in capturing curved rotating flows within the impeller. The **k- ω** model performed better in predicting wake and separated flow in the diffuser. Notably, the **SST-CC** model exhibited a reasonably stable, robust, and computationally efficient performance in predicting both global and local flow features.

This study highlights the importance of carefully selecting turbulence models to achieve accurate predictions of centrifugal compressor flow fields. The findings contribute to the development of more reliable CFD simulations, ultimately enhancing the design process of centrifugal compressors and other turbomachinery applications.

Moving forward continued research and innovation in compressor technology are essential for meeting the evolving needs of industries worldwide. By integrating advanced modeling techniques and predictive methodologies, engineers and researchers can further optimize compressor performance and drive efficiency gains across various industrial applications.

In summary, this thesis represents a significant contribution to the field of compressor technology, offering both theoretical insights and practical applications. By bridging the gap between theory and practice, this study advances our understanding of centrifugal compressors and lays the groundwork for continued innovation in this critical area of industrial machinery.

REFERENCES

- [1]. Lee Gibson, Lee Galloway, Sung in Kim, Stephen Spence: **Assessment of turbulence model predictions for a centrifugal compressor simulation.** 2017.
- [2]. Shady Ali, Kevin J. Elliott, Eric Savory, Chao Zhang, Robert J. Martinuzzi, William E. Lin: **Investigation of the Performance of Turbulence Models with Respect to High Flow Curvature in Centrifugal Compressors .** 2016.
- [3]. Sabri Deniz, Armando Del Rio and Ernesto Casartelli: **Experimental and numerical investigation of the speed-no-load instability of a low specific speed pump-turbine with focus on the influence of turbulence models.** 2019.
- [4]. G. Dufour¹, J.-B. Cazalbou, X. Carbonneau, P. Chassaing: **Assessing Rotation/Curvature Corrections to Eddy-Viscosity Models in the Calculations of Centrifugal-Compressor Flows .** 2008.
- [5]. William J. Gooding, Matthew A. Meier, and Nicole L.: **Key THE IMPACT OF VARIOUS MODELLING DECISIONS ON FLOW FIELD PREDICTIONS IN A CENTRIFUGAL COMPRESSOR .** 2020.
- [6]. O Dumitrescu, V Drăgan, I Porumbel and B Gherman: **Numerical assessment of a very high-pressure ratio centrifugal impeller .** 2020.
- [7]. Zi-liang LI, Xin-gen LU, Yun-feng WU , Ge HAN: **Quantitative Investigation of the Turbulence Model Effect on High pressure-ratio Centrifugal Compressor Performance Prediction.**
- [8]. Ziegler K. U., Gallus H. E., and Niehuis R.: **A study on impeller-diffuser interaction— Part I: Influence on the performance.** *Journal of Turbomachinery*, 125 (1): 173–182, 2013.
- [9]. Ziegler K. U., Heinz E. Gallus, Reinhard Niehuis: **A Study on Impeller-Diffuser Interaction-Part II: Detailed Flow Analysis.**
- [10]. Mustapha, BENDJEDDA Sofiane & BESSAYAH.: **simulation numérique de l'écoulement interne dans une roue de compresseur centrifuge.** 2017.

[11]. Heinrich, Martin.: **Genetic Optimization of Turbomachinery Components using the Volute of a Transonic Centrifugal Compressor as a Case Study.** *by Dipl. Freiberg.*

[12]. Klüver, Merle : **A COMPARISON OF PREDICTED PERFORMANCE VALUES FROM A 1D MODEL AND CFD SIMULATIONS TO MEASURED DATA FOR AN INDUSTRIAL HIGH-SPEED CENTRIFUGAL COMPRESSOR.** 2023.

[13]. Kim, Kwang-Yong: **Design optimization of fluid machinery applying computational fluid dynamics and numerical optimization.**

[14]. **Design optimization of fluid machinery applying computational fluid dynamics and numerical optimization.**

[15]. Baldwin, W. S.and Lomax, H.Thin-Layer: **Approximation and Algebraic Model for Separated Turbulent Flows.** (1978). *AIAA Paper 87-257. DOI:10.2514/6.1978-257.*

[16]. Blazek, Jiri: **Computational Fluid Dynamics Principles and Applications .**

[17]. Cleveland, Rama S. R. Gorla, Ohio,U.S.A. Aijaz A.Khan: **Turbomachinery Design and Theory .**

[18]. El-Sayed, Ahmed F.: **Aircraft Propulsion and Gas Turbine Engines .**

[19]. Boyce, Meherwan P.: **Centrifugal compressors : a basic guide.**

[20]. Ling, Jack C.L.: **Compressors for Miniature Unmanned Aerospace Propulsion Systems .**

[21]. BASKHARONE, ERIAN A.: **Principles of Turbomachinery in Air-Breathing Engines .**

[22]. Guwahati.: **Aircraft Propulsion Vinayak N. Kulkarni Department of Mechanical Engineering.** *Indian Institute of Technology.*

[23]. Gymkhana.: **Centrifugal compressors. IITB.**

[24]. Anil W. Date: **Introduction to Computational Fluid Dynamics,** *Cambridge University Press: 2012.*

- [25]. Jameson, A., Schmidt, W. and Turkel, E.: **Numerical Solution of the Euler Equations by Finite Volume Methods**, *AIAA Paper 81-1259* ,1981.
- [26]. Frank M. White, *Viscous Fluid Flow*, McGraw-Hill: **Mechanical Engineering 3rd Edition**, ISBN-10: 0072402318.
- [27]. Батурин О.В: **Numerical Study of the Operating Process in the Stage of a Centrifugal Compressor**, 2013.
- [28]. Sivagnanasundaram S., Spence S., and Early J.: **Map width enhancement technique for a turbocharger compressor**, *Journal of Turbomachinery*. 136 (6): 061002, 2013.
- [29]. Moore J, Moore J.G.: **Effects of curvature and rotation on turbulence in the NASA low-speed centrifugal compressor impeller**. *Virginia polytechnic institute and state university*,1990.
- [30]. Boyce, Meherwan.: **P Gas Turbine engineering handbook, fourth edition**.